Study of Thermal and Magnetic Properties in Strongly Correlated Materials

by

Lu Chen

A dissertation submitted in partial fulfillment
of the requirements for the degree of
Doctor of Philosophy
(Physics)
in the University of Michigan
2020

Doctoral Committee:

Professor Lu Li, Chair
Assistant Professor John Heron
Professor Çağlıyan Kurdak
Associate Professor Kai Sun
Assistant Professor Liuyan Zhao

Lu Chen

chelu@umich.edu

ORCID iD: 0000-0002-0407-9209

Acknowledgments

First and foremost, I would like to thank my adviser, Professor Lu Li, for his guidance and generous support in my research over the past six years. I especially enjoy the discussion with him on the various research topics which almost happen every day. He has a broad interest in many different fields in condensed matter physics, which greatly broadens my view and motivates me. Lu always comes up with interesting ideas that motivate the students a lot in conducting deeper research. Lu is also good at mentoring students, especially new Ph.D. students who just enter this field. Apart from the experimental skills, Lu also helped me a lot in academic writing. The whole experience of working with Lu is quite enjoyable to me since Lu always gives me timely feedback on my research which helps me conduct my research quite efficiently. Apart from the research, Lu also gives me a lot of help in other fields of my academic career. With Lu's recommendation, I was able to win several awards and fellowships during my Ph.D.. I feel extremely lucky to have Lu as my Ph.D. advisor.

I am also quite grateful for the great help of current and former members in Lu's Lab: Ziji Xiang, Kuan-Wen Chen, Colin Tinsman, Tomoya Asaba, Fan Yu, Benjamin Lawson, and Gang Li, who helped me a lot with my research projects. I would also like to thank Prof. Haidong Zhou from the University of Tennesse and Dr. John Singleton from the Pulsed Field Facility in Los Alamos National Lab for their collaboration in my research.

Finally, I would like to thank my parents, my sister, and my husband for their great help and trust in me. Although my parents were not able to get good education due to some historical reasons, they are indeed very kind, generous and full of wisdom. They fully trust and fully support me in everything that I want to do, including pursuing a Ph.D. in physics. Apart from my parents, my sister also mentally, physically, and financially supports me a lot across my past life. My husband, Lu Ma, is also a physics Ph.D.. The interesting thing is he is working on atomic physics and optics which have been scaring me a lot since I was in undergraduate school. So he is and will always be a genius in my point of view. There are two very important "Lu"s in my life, one is my advisor, the other one is my husband. My husband always waits for me in the lab no matter how late I stay in the lab. My husband is also a good chef who feeds me well and gives me the strength to work on my research. I really want to thank him for all the time he has spent in my lab, all the research equipment he has lent to me, and all the research talks he has listened from me. I am so lucky to have such a great family as my support.

TABLE OF CONTENTS

LIST OF FIGURES

ABSTRACT

The search for quantum materials is always an exciting field in condensed matter physics. The strongly correlated materials are one of the most intensively studied systems for decades. Due to the complex interplay between the electronic, magnetic, and structural degrees of freedom, the strongly correlated materials display a broad range of interesting phenomena such as high-temperature superconductivity and the colossal magnetoresistance (CMR) in manganites. An important characteristic of these materials is the existence of several competing states with different symmetries and low energy excitations, such as the complicated phase diagram exhibited by transition metal oxides. A variety of phases with spin, charge, and orbital order leads to many systems such as superconductors, metals, insulators, multiferroics, and other novel phases. With the introduction of the concept of topology, topological quantum materials have attracted tremendous attention in recent years. Among them, superconductors with non-trivial topologies are one of the most studied materials due to the existence of gapless boundary states, such as the zero-energy bound states, in them, which have the potential of realizing fault-tolerant quantum computations.

A new type of measurement technique with high sensitivity is urgently demanded to reveal the complicated electronic and magnetic properties in quantum materials. We develop a highly sensitive torque differential magnetometry using the qPlus mode of a quartz tuning fork. We observe a sharp resonance of the quartz tuning fork at low temperatures down to 20 mK. We calibrate our torque differential magnetometry by measuring the angular dependence of the hysteresis loop in single-crystal $Fe_{0.25}TaS_2$. Furthermore, we demonstrate the

high sensitivity of the torque differential magnetometry by measuring the quantum oscillations of a bismuth single crystal. To use the tuning fork magnetometry in a wet cryogenic system, we also make vacuum cells for the tuning forks which could hold a high vacuum at liquid Helium temperature. We also demonstrate the application of tuning fork magnetometry in a pulsed magnetic field up to 65 T by measuring the hysteresis loop and melting field of underdoped high-temperature superconductors $YBa_2Cu_3O_y$.

We conduct thermal transport study in two strongly correlated materials, vanadium dioxides (VO_2) and $SmBaMn_2O_6$. The nature of the metal-insulator-transition in the transition metal oxides has been a long-studied topic. We investigate the thermal conductivity across the phases transitions in VO_2 and $SmBaMn_2O_6$ single crystals and get one-order-of-magnitude enhancement in the thermal conductivity within the metal-insulator transition. These experiments shed light on the role played by phonon across the first-order structural transition. These experiments also solve the thermal management issues in solid-state materials and could bring potential applications in electronic devices.

To reveal the superconducting gap structure of a topological superconductor candidate, we conduct the heat capacity measurement in the Nb-doped Bi_2Se_3 single crystals. For all samples, the heat capacity shows an exponential decay when T approaches zero, which indicates a nodeless superconducting gap structure. Both the nematic order observed in the torque magnetometry measurement and the nodeless gap structure obtained by the heat capacity measurement indicate an odd parity topological superconductor.

We also present a study of the Nernst effect in an iron-based superconductor with a non-trivial band topology $Fe_{1+y}Te_{1-x}Se_x$. A non-zero Nernst signal is observed in a narrow temperature region around the superconducting transition temperature T_c at a zero field. This anomalous Nernst signal shows symmetric dependence on the external magnetic field and indicates an unconventional vortex contribution in an s-wave superconductor with a strong spin-orbit coupling, which is originated from the local magnetic moments of the interstitial Fe atoms. Our experiments also provide the first evidence of a locally broken

time-reversal symmetry in bulk $Fe_{1+y}Te_{1-x}Se_x$ single crystals.

In summary, my Ph.D. thesis focuses on the development of new measurement techniques such as the torque differential magnetometry and the thermal measurement setup compatible with PPMS, which are capable of resolving novel properties of many solid-state materials. With the help of these newly developed techniques, I study the thermal and magnetic properties in several strongly correlated materials.

CHAPTER 1

Introduction

1.1 Strongly Correlated Electronic Systems: Transition Metal Oxides

For many materials that shape our world, their properties can be well understood by the band theory based on a non-interacting electron assumption. Metals, semiconductors, band insulators, and semimetals of band theory all fall in this category whose properties are comparatively insensitive to the repulsive interactions between electrons. However, there are also lots of materials in which the electron-electron interaction determines their electronic, magnetic, optical, and mechanical properties. These materials fall into the category of strongly correlated materials. In the strongly correlated electronic systems, the collective states can not be explained by the one-particle approximation. The repulsive electron-electron interactions must be taken into account when trying to understand their properties.

The strongly correlated materials have become one of the most intensively studied systems in the condensed matter physics [1, 2, 3]. Due to the complex interplay between their electronic, magnetic and structural degrees of freedom, the strongly correlated materials display a broad range of interesting phenomena such as high-temperature superconductivity [4] and the colossal magnetoresistance (CMR) in manganites, where the electrical resistance changes dramatically in the presence of a magnetic field [5, 6]. An important characteristic of these materials is the existence of several competing states with different symmetries and low energy excitations, such as the complicated phase diagram exhibited by transition metal oxides [7, 8, 9, 10, 11, 12]. A variety of phases with spin, charge, and orbital order leads to many systems such as superconductors, metals, insulators, multiferroics, and other phases. New phases often emerge through a "quantum phase transition" near the "quantum critical point" when a physical parameter, such as the composition, temperature, pressure, or external field, is tuned. This effect could be manifested by an order-of-magnitude change in the electrical resistivity, such as the metal-insulator transi-

tion in cuprates or CMR in manganites. The strong correlation between electrons plays a crucial role across the transition which means a simple tuning on this term could result in a dramatic change in material's property.

Understanding, controlling, and predicting the complexity in the strongly correlated systems is one of the biggest challenges in today's condensed matter physics. On the theory side, it's difficult to conduct the band structure calculation when considering strong electron correlations. The standard $ab\ initio$ methods, which are well suited to study weakly correlated systems like conventional metals and insulators, can not accurately predict the band structure for strongly correlated systems like Mott insulators [13]. The simplified model Hamiltonians approach can better capture the essential physics but can hardly generate any analytical results. A combination of different types of approaches turns out to be a successful way. The modified density function theory [14] (also known as LDA+U, where LDA stands for "local density approximation") and the Dynamical Mean-Field Theory (DMFT) [15, 16] have successfully produced many promising results [17, 18].

Strongly correlated electron materials have attracted tremendous interest not only because of the unusual physics origin behind the complex phenomena but also due to their potential application in modern technology. In this chapter, we will give a brief introduction of several types of well studied strongly correlated materials. The aim is to summarize the interesting topics that have been studied and the background that needs to know before introducing our research.

1.1.1 Manganites and High-temperature Superconductors

The properties of strongly correlated electrons are usually controlled by two parameters: the tunneling electron hopping amplitude t (or the one-electron bandwidth W) and the density of charge carriers (band filling). Electrons tend to hop between nearby sites with an energy scale of t while the on-site Coulomb repulsive energy U hinders this process. The competition between t and U results in different electronic and magnetic states. When $\frac{U}{t}$ is large, electrons are more localized and results in a Mott insulator. As $\frac{U}{t}$ gradually increases, an insulator-metal transition could happen when electrons become less localized. Another tuning parameter is the band filling. The ground state of a Mott insulator is usually antiferromagnetic (AFM), while changing the doping level, i.e. a small deviation from the half-filling state, leads to a paramagnetic conducting state.

These fundamental parameters can be tuned in multiple ways, such as crystal engineering or doping. For perovskite with formula (RE,AE)MO_3, where RE, AE, and M stand for the trivalent rare-earth and divalent alkaline-earth ions, the crystal structure can be modified

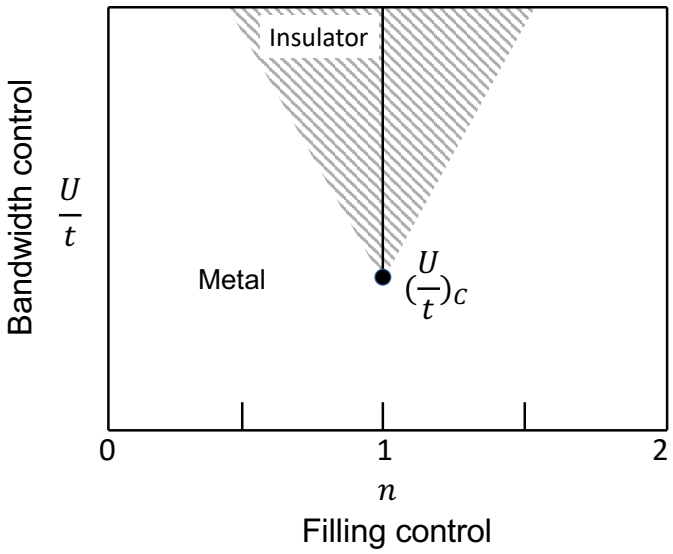

Figure 1.1: Insulator-Metal transitions in strongly correlated electron systems controlled by the bandwidth W (or hopping amplitude t) and the band filling n (or doping level x). $(\frac{U}{t})_C$ is the critical point at which the transition occurs.

by tuning the so-called tolerance factor f, which is defined as

$$f = \frac{r_A + r_O}{\sqrt{2}(r_M + r_O)} \tag{1.1}$$

where r_i, i = A, M, or O, represents the ionic radius of each element. The tolerance factor represents the mismatch between the ironic size of A and M. The perovskite holds a cubic structure when $f \approx 1$. It gradually transforms into a rhombohedral and then to an orthorhombic ($GdFeO_3$-type) structure as r_A (or equivalently f) decreases. The M-O-M bond distortion induced by the crystal structure change also results in the decrease of the one-electron bandwidth W, which causes the metal-insulator transition observed in the $RENiO_3$ family [19]. For example, $LaNiO_3$ is a paramagnetic metal with $f \approx 0.96$ while other RENiO3 with smaller f are AFM insulators at the ground state and undergo a thermally induced insulator-metal transition as temperature increases.

A good example of band-filling-(or doping-) controlled Mott transition is the high-temperature superconductors of copper oxides, such as the hole doping in $La_{2-x}Sr_xCuO_4$ and the electron doping in $Nd_{2-x}Ce_xCuO_4$. The parent compound $LaCuO_4$ is an antiferromagnetic Mott insulator. It can be doped by replacing some of the trivalent La by divalent Sr which results in x holes are added to the Cu-O plane and the doped compound becomes superconductors. In $Nd_{2-x}Ce_xCuO_4$, the reverse process happens in that x electrons are

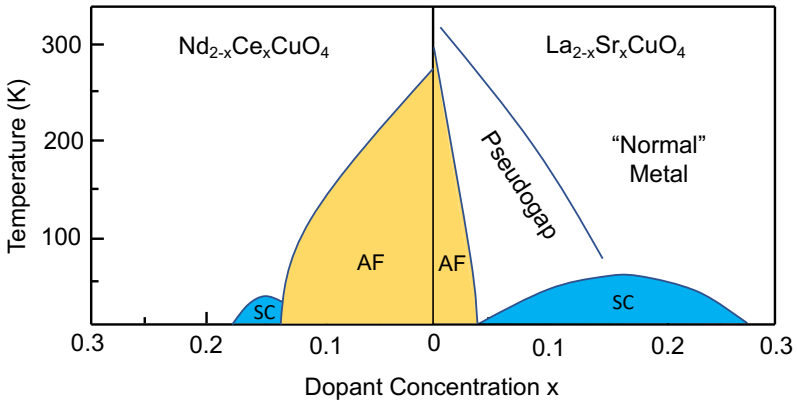

Figure 1.2: Schematic phase diagram of high-temperature superconductors showing hole doping (right side) and electron doping (left side) [21].

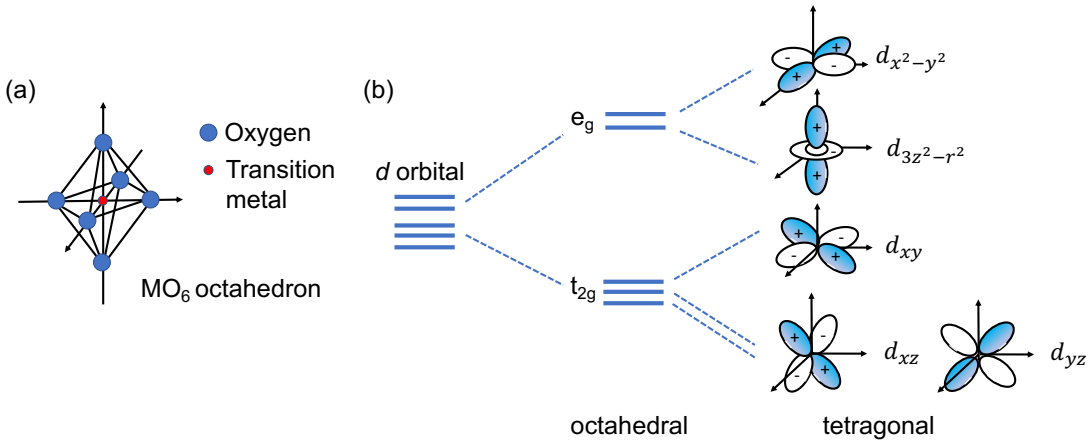

Figure 1.3: (a) MO_6 octahedron in a perovskite structure. (b) d-electron orbitals and level splitting due to the crystal field and Jahn-Teller effect.

added to the Cu-O plane which also brings superconductivity [20]. The phase diagram of $La_{2-x}Sr_xCuO_4$ and $Nd_{2-x}Ce_xCuO_4$ are plotted in Figure 1.2.

The other important phenomena that have been studied a lot in the transition metal perovskites are the abundant ordering of charge, spin, and orbital degrees of freedom. The M iron is surrounded by six O^{2-} irons in a MO_6 octahedron (as shown in Figure 1.3 (a)). The d-orbital degeneracy is partly lifted by the crystal field potential and results in two sub energy levels (e_g orbitals and t_{2g} orbitals). The interplay between the spin and orbital degrees of freedom produces multiple spin-orbital ordering patterns. In the perovskite manganites, the Jahn-Teller effect causes the deformation of the MnO_6 octahedron which is manifested by the elongation or compression of the octahedron along the crystal z-axis (as shown in Figure 1.3 (b)). In $LaMnO_3$, the Jahn-Teller effect causes the compressing of the c axis

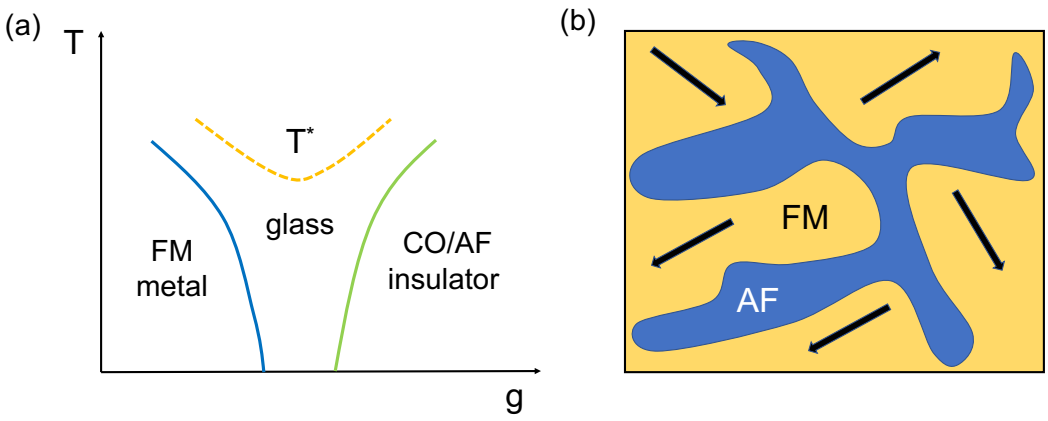

Figure 1.4: (a) Schematic phase diagram of two competing phases (ferromagnetic (FM) metal and charge-ordered antiferromagnetic (CO/AF) insulator)) in the presence of quenched disorder. g is a tuning parameter such as electronic density or bandwidth. (b) The CMR state for manganites where ferromagnetic clusters with randomly oriented magnetic moments separated by regions where charge-ordered antiferromagnetic states are stabilized.

and the expansion in the ab plane. The spins couple ferromagnetically in the ab plane and results in a ferromagnetic ground state [22]. While in $BiMnO_3$, the orbital ordering gives a Mott insulating ferromagnetic ground state due to a lower crystal symmetry [23]. The CMR effect observed in perovskite-type manganites is believed to relate to the phase competition between the ferromagnetic metallic and the charge-orbital ordered states. The CMR effect is observed near the bicritical region where the ferromagnetic metallic and the charge-orbital ordered states compete with each other. The other ingredient which causes the CMR is the quenched disorder near the critical region. The double-perovskite manganite has an even more complicated charge/orbital ordering structure compared to its simpler version (perovskite). The A-site-ordered and disordered-perovskite have the same ground state of a ferromagnetic metal but different Curie temperatures and charge-ordering transition temperatures [24, 25]. In $RE_{0.5}Ba_{0.5}MnO_3$ systems, only the A-site disordered systems exhibit CMR [26].

One reason that results in the unexpected properties of the transition metal oxides is the inhomogeneity at the nanoscale, which makes the early theories based on homogeneous systems unsuccessful in explaining many experimental results. In perovskite manganites, a theory predicts [27] that the ground state is a nanoscale mixture of different phases, particularly in the presence of quenched disorder [28, 29, 30]. This inhomogeneous ground state has been experimentally observed in systems such as Sr-, Ca- and Pr-doped manganese oxides (La, Pr, Ca) MnO_3 by electron microscopy [31, 32] and pulsed neutron diffraction

[33]. In the clean limit without the quenched disorder, ferromagnetic metallic states and antiferromagnetic insulating state are two key competing states in manganites. The quenched disorder can be introduced into the system through lattice-distorting chemical doping, non-statistical fluctuations of dopant density, or strain fields, which results in a coexistence of the two competing states. A mixed glassy state is generated when the temperature is between the Curie and Néel temperature (as shown in Figure 1.4 (a)), where perturbations like magnetic fields, electric fields, pressure, or strain can induce dramatic changes like CMR effect [28, 29]. Figure 1.4 (b) sketches the CMR state for manganites where ferromagnetic clusters with randomly oriented magnetic moments separated by regions where charge-ordered antiferromagnetic states are stabilized. A small magnetic field is enough to re-orient the magnetic moment and induce dramatic change through a percolation process [32].

We conduct the thermal transport and thermoelectric study cross the two-step charge-orbital-order transition in double perovskite manganite $SmBaMn_2O_6$, which will be discussed in Chapter 3.2.

1.1.2 Vanadium Dioxide (VO_2)

Another canonical example of transition metal oxides with strongly correlated electrons is Vanadium Dioxide (VO_2). VO_2 undergoes a first-order phase transition from the low-temperature monoclinic insulating phase to a high-temperature rutile metallic phase at $T_c \approx$ 340 K [34]. A long-standing question is whether the metal-insulator transition is primarily driven by the structural change due to electron-phonon interactions (Peierls transition) or by electron-electron interactions (Mott transition) [35, 36, 37]. On the theory side, traditional density function theory (DFT) [38, 39] and the corrections based on an effective Hubbard U [39, 40] or hybrid functions [41] all fail in explaining the metal-insulator transition. Recently, a theoretical calculation using the correlated fixed-node diffusion quantum Monte Carlo (FN-DMC) method to characterize the electronic structure and magnetic response of VO_2 in two phases [42]. It reveals the structural distortion directly causes the metal-insulator transition and a change in the coupling of vanadium spins when account for the electron correlations, which indicates a Peierls transition. But far-field infrared studies reveal the importance of the electronic correlations in the metal-insulator transition in VO_2 [43, 44]. The scanning near-field infrared studies on VO_2 in the Metal-insulator regime shows a phase-separated picture, nanoscale metallic "puddles" exists in the insulating host. A divergent optical mass observed by the far-field infrared spectroscopy suggests that electron-electron interactions trigger the metal-insulator transition VO_2, which

indicates it's primarily a Mott Transition [45]. Studies about the metal-insulator transition nature in VO_2 is still ongoing. We study the thermal conductivity within the metal-insulator transition in VO_2, which will be discussed in Chapter 3.1.

1.2 Topological Superconductors

The search for topological quantum materials has become an exciting field in condensed matter physics in recent years due to their potential of realizing topologically protected (or fault-tolerant) quantum computation. Topological insulators have attracted tremendous attention due to its peculiar characteristic of an edge or surface state that shows up on an insulating bulk state [46, 70, 48]. Soon afterward, a class of topological superconductors which hold time-reversal-invariance and a fully gapped bulk states plus a gapless surface Andreev bound states is theoretically predicted [49, 50, 51]. A lot of efforts are put into looking for possible candidates for topological superconductors. Topologically nontrivial superconductors are first discussed with 1D and 2D models. Both models consider a spinless, time-reversal-breaking p-wave paring superconducting state and predict the existence of Majorana zero mode in the vortex core of 2D [52] system or at the edge in the 1D case [53]. Majorana fermions are their own antiparticles.The Read-Green model predicts that the bulk Bogoliubov quasiparticles become dispersive itinerant Majorana quasiparticles and the bound states at the vortex cores become Majorana zero mode which can be used to achieve quantum computation [52].

In this chapter, we will first introduce some basic concepts for understanding the topology in quantum materials. Then we will focus on the general definition and properties of topological superconductors. More concrete guidance for realizing topological superconductors in real materials and several topological superconductor candidates will be introduced later in this chapter.

1.2.1 Concept of Topology in Quantum Materials

Topology is a mathematical concept that describes the properties of a geometric object. Two objects are considered to hold the same topology if one can be continuously transformed into the other, such as by stretching, twisting, crumpling, and bending but not by tearing or gluing. For example, a sphere and an ellipse are topologically identical, a donut and a teacup is topologically identical. But a sphere and a donut are not topologically identical since you can not continuously transform a sphere to a donut without punching a hole in it. Physicist uses the mathematical tool of topology to classify materials into different

categories. When a quantum mechanical wavefunction can be connected adiabatically to another wavefunction, these two wavefunctions can be considered to be topologically identical. For example, a condensed matter system whose wavefunction can be adiabatically connected to the atomic limit, the condensed matter system is topologically trivial, otherwise, it is topologically nontrivial. The topological classification can be done by defining an integer number called topological invariant, such as the Chern number [55, 56]. A Z_2 topological invariant is defined when describing a 2D time-reversal-invariant insulator [57, 58]. Later on, a more systematic topological classification for both insulators and superconductors are developed based on the symmetry properties [49, 51].

Here we will give a brief introduction to how topological invariants are defined. In a solid-state system with a Bloch Hamiltonian $\mathcal{H}(\boldsymbol{k})$, the eigenstates of the Bloch wave is given by

$$H(\boldsymbol{k})|u_n(\boldsymbol{k})\rangle = E_n(\boldsymbol{k})|u_n(\boldsymbol{k})\rangle, \tag{1.2}$$

where $\boldsymbol{k}$ is the crystal momentum. The Berry connection is defined as

$$\mathcal{A}^{(n)}(\boldsymbol{k}) = i\langle u_n(\boldsymbol{k})|(\boldsymbol{\partial_k} u_n \boldsymbol{k})\rangle. \tag{1.3}$$

A gauge-invariant quantity can be constructed from $\mathcal{A}^{(n)}(\boldsymbol{k})$ as the field strength of the Berry connection

$$\mathcal{F}^{(n)}_{ij}(\boldsymbol{k}) = \partial_{ki}\mathcal{A}^{(n)}_{kj}(\boldsymbol{k}) - \partial_{kj}\mathcal{A}^{(n)}_{ki}(\boldsymbol{k}). \tag{1.4}$$

The integral of the field strength over the whole Brillouin zone defines a topological invariant, Chern number. Let's take the Chern number in 2D, which is used to describe the quantum spin Hall insulator, as an example. For a 2D system, the Chern number of the nth band is defined as

$$Ch^n_1 = \frac{1}{2\pi}\int_{2dBZ} dk_x dk_y \mathcal{F}^{(n)}_{xy}(\boldsymbol{k}), \tag{1.5}$$

where the integral is over the 2D Brillouin zone. The total Chern number of the occupied bands is

$$Ch = \sum_{E_n<E_F} Ch^{(n)} \tag{1.6}$$

The Hall conductance is directly linked to the total Chern number through

$$\sigma_{xy} = -\frac{e^2}{h}Ch. \tag{1.7}$$

In a system with time-reversal-symmetry, $Ch = -Ch$, which means $Ch = 0$. This indicates a broken time-reversal-symmetry is necessary for realizing a nontrivial quantum Hall state

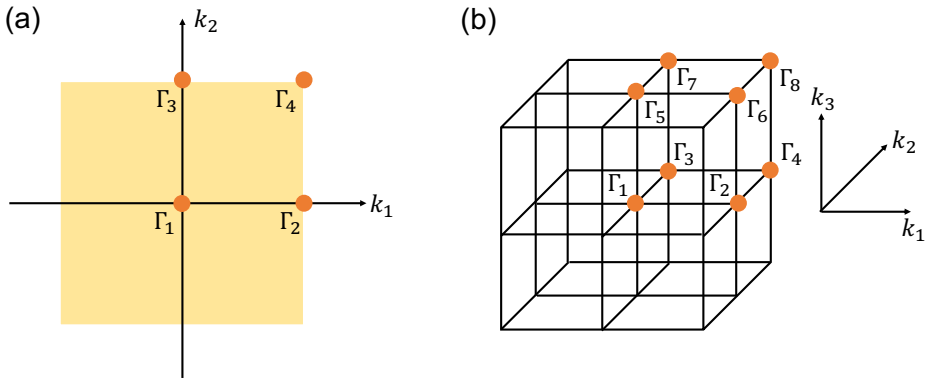

Figure 1.5: Time-reversal-invariant momenta Γ_i $(i = 1, 2, \cdots)$ in (a) 2D and (b) 3D Brillouin zones.

with $Ch \neq 0$. That's why a magnetic field is needed to break the time-reversal-symmetry to achieve a quantum Hall state.

The topological insulators that people are interested in nowadays are materials that hold non-trivial topology while preserving the time-reversal-symmetry. To achieve a time-reversal-invariant topological insulator, we need to include the spin-orbit coupling. A new topological invariant which is called Z_2 index is introduced to describe such kinds of materials. In 2005, C. L. Kane and E. J. Mele propose a theoretical model that converts an ideal 2D semimetallic graphene to a quantum spin Hall insulator when considering the spin-orbit coupling [57]. They also show this phase is associated with a novel Z_2 topological invariant which distinguishes a quantum spin Hall insulator from an ordinary insulator. This Z_2 classification is defined for time-reversal-invariant Hamiltonians [58]. Then B. A. Bernevig, T. L. Hughes, and SC. Zhang propose the quantum spin Hall can be realized in mercury telluride-cadmium telluride semiconductor quantum wells [59], which is experimentally achieved by M. König $et.\ al.$ in 2007 [60].

Using the time-reversal invariance, we can also introduce Z_2 indices in 3D [61]. A 3D time-reversal-invariant system has four independent Z_2 indices that distinguish the ordinary insulator from "weak" and "strong" topological insulators. These phases are characterized by the protected gapless surface (or edge) states, which are insensitive to weak disorder and interactions. If the 3D system also holds an inversion symmetry, the Z_2 indices can be defined in a simpler way as [62]

$$(-1)^{\nu_{3d}} = \prod_{i=1}^{8} \prod_{n=1}^{N} \xi_n(\Gamma_i), \tag{1.8}$$

where ν_{3d} is the 3D topological index (+1 or -1), n is the index for filled bands, and $\xi_n(\Gamma_i)$ is the eigenvalue of parity operator at one of the eight time-reversal-invariant momenta Γ_i in the 3D Brillouin zone (as shown in Figure 1.5 (b)). In the same way, the Z_2 index in 2D is evaluated as

$$(-1)^{\nu_{2d}} = \prod_{i=1}^{4} \prod_{n=1}^{N} \xi_n(\Gamma_i), \tag{1.9}$$

where Γ_i is one of the four time-reversal-invariant surface momenta in a 2D Brillouin zone (as shown in Figure 1.5 (a)). Liang Fu and C. L. Kane also predict a number of specific materials that are strong topological insulators [62], including the semiconducting alloy $Bi_{1-x}Sb_x$, α-Sn, and HgTe under uniaxial strain. They propose that the non-trivial topology in $Bi_{1-x}Sb_x$ can be verified by looking at the surface states by angle-resolved photoemission spectroscopy (ARPES) and counting the number of times the surface states cross the Fermi energy between two time-reversal-invariant momenta. D. Hsieh $et.\ al.$ first report the observation of massive Dirac particles in the bulk as well as gapless surface states in $Bi_{1-x}Sb_x$ using incident-photon-energy-modulated angle-resolved photoemission spectroscopy (IPEM-ARPES) [63]. Then the transport studies detect topological 2D transport channels in $Bi_{1-x}Sb_x$ [64]. Scanning tunneling spectroscopy (STS) also shows a peculiar chiral spin texture which indicates a topological-protected surface state [65]. Then a spin-polarized surface state is directly observed in $Bi_{1-x}Sb_x$ by spin-resolved photoemission spectroscopy (spin-ARPES) which verifies the time-reversal-invariant topological insulator states in $Bi_{1-x}Sb_x$ [66, 67]. A large-gap topological-insulator class with a single Dirac cone has also been observed on the surface of Bi_2Se_3 class of materials by ARPES [68]. A room-temperature topological order and non-trivial spin-texture in stoichiometric Bi_2X_3 (X = Se, Te) have also been revealed by spin- and angle-resolved photoemission spectroscopy (spin-ARPES) [69]. Since then, numerous 3D topological insulators have been discovered and opens a new era of study on topological materials [46, 70, 71].

1.2.2 Topological Superconductors

Similar to an insulator, all the negative energy states of the BdG Hamiltonian are fully occupied in a superconductor. So we can define various topological numbers in a similar way for superconductors depends on their symmetry and dimension properties. Generally speaking, all superconductors with nonzero topological numbers can be considered as (weak) topological superconductors, such as unconventional superconductors with nodal gap structure where the nodes have non-trivial topological numbers. Strictly speaking, a fully-opened gap is required besides a non-zero topological number to define a strong

topological superconductor. Theoretically speaking, for general Hamiltonians, topological superconductors can exist in 1D, 2D, and 3D. Superconductors hold a special type of symmetry, the particle-hole symmetry, which allows us to define topological numbers other than the Chern number. For example, a Z_2 index can be defined in terms of the Berry phase similarly as the topological insulator for 1D superconductors [72]. But this 1D Z_2 index becomes trivial due to the Kramer degeneracy in time-reversal-invariant superconductors. So a new way to define the Z_2 index in 1D is proposed and extended to 2D and 3D [73]. Schnyder $et.\ al.$ construct a table of topological numbers for fully-gapped insulators and superconductors in multiple dimensions, which can be found in Ref. [73].

An important feature of topological superconductors is the existence of gapless boundary states. The bulk states of a topological superconductor are nontrivial. Across the boundary of a topological superconductor and vacuum, which is topologically trivial, a gapless boundary state is required to bridge these two un-matched topologies [74]. Topological superconductors with different topological numbers also have different boundary states, which is called bulk-boundary correspondence [73, 75]. Zero-energy states can also be found on topological defects in topological superconductors. A topological defect holds a different topology compared to the bulk material, so a zero-energy state could appear at the boundary of these two systems in the same way as a gapless boundary state. For example, vortices in topological superconductors can support gapless boundary states, which is called "zero modes" (zero-energy states) [76, 77, 78, 79]. Actually, even before the systematic study of topological superconductors, topologically nontrivial superconductors are discussed in 1D [80] and 2D [52] spinless, time-reversal-breaking p-wave superconductors in 2000. These models give non-Abelian Majorana zero mode in the vortex core in the 2D system and edge states in the 1D system. A similar non-Abelian Majorana zero mode is also proposed in 2D s-wave superconductors [54]. The gapless boundary states in topological superconductors attract tremendous attention due to their potential of realizing fault-tolerant quantum computations.

Interestingly, people have started to search for non-trivial topology in superfluid helium 3 (He-3) even before all the topological quantum systems develop [81]. Under a magnetic field, the He-3 separates into a symmetry protected topological phase and a non-topological phase. The former phase hosts the symmetry protected Majorana fermions and odd-frequency even-parity Cooper pairs [82]. Recently, many efforts have been paid to looking for topological superconductors. Experimentally, there are two ways to realize topological superconductors, the intrinsic ones and the artificially engineered ones. Intrinsic topological superconductors are those in which a topologically-nontrivial gap function naturally show sup. The odd-parity superconductors are one type of intrinsic ones. The-

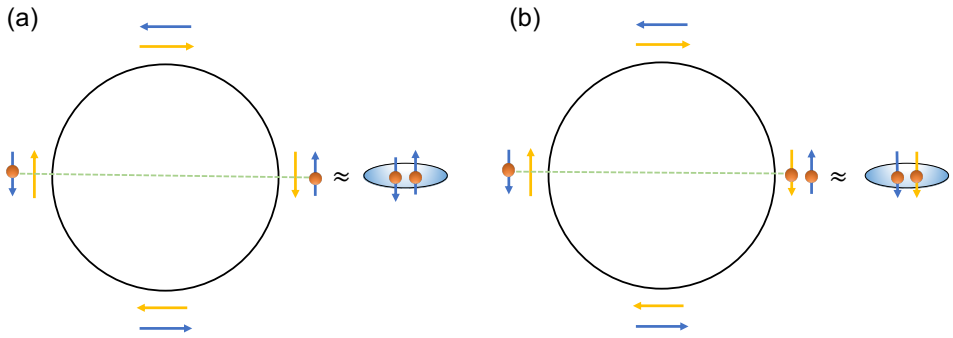

Figure 1.6: A helical spin structure on the Fermi surface induced by strong spin-orbit coupling in superconducting topological insulators. (a) An intra-orbit pairing results in a spin-singlet state. (b) An inter-orbit pairing results in a spin-triplet state.

ory predicts that an odd-parity superconductor is a topological superconductor if the Fermi surface encloses an odd number of time-reversal-invariant momenta in the Brillouin zone [83, 84, 85]. Systems with strong spin-orbit coupling tend to realize the odd-parity pairing states, such as the carrier-doped Bi_2Se_3. As a topological insulator, a strong spin-orbit coupling can induce a helical spin structure on the Fermi surface (as shown in Figure 1.6). If the attraction between electrons in the same orbit is the strongest, Cooper pairs are formed between electrons in the same orbit with antiparallel spins (as shown in Figure 1.6 (a)). If the attraction between electrons in different orbits dominates, Cooper pairs are formed between electrons in different orbits with parallel spins (as shown in Figure 1.6 (b)). Theoretical calculations prefer the spin-triplet pairing states [85, 86]. Once the three-fold rotational symmetry is considered by introducing a warping term into the bulk Hamiltonian, we can even achieve a nematic superconductor in the doped Bi_2Se_3 [87]. The spontaneous symmetry breaking in Cu-doped Bi_2Se_3 has been observed by nuclear magnetic resonance measurements (NMR) [88] and thermodynamic measurements [89]. In Sr-doped Bi_2Se_3, the upper critical field H_{c2} also presents clear two-fold symmetry in magnetotransport measurements [90, 91, 92]. Recently, our group discovered that the amplitude of the superconducting hysteresis loop is enhanced along one direction in Nb-doped Bi_2Se_3 by torque magnetometry measurement, which indicates a spontaneous breaking of the rotational symmetry [93]. We conduct the specific heat measurement in Nb-doped Bi_2Se_3 to study the superconducting gap structure, which will be introduced in Chapter 4.

A superconducting state is also theoretically predicted in carrier-doped Weyl semimetals under different symmetry conditions [94, 95, 96]. Dirac semimetals can also host superconducting states by carrier-doping or applying pressure [97, 98]. The high-pressure resistance study shows the topological Dirac semimetal Cd_3As_2 enters a superconducting

state with a $T_c \approx 2$ K under a pressure of 8.5 GPa [99]. The other two groups also show that the mesoscopic point contacts between pure silver and Cd_3As_2 exhibit unconventional superconductivity with a critical temperature of 6 K [100, 101].

Apart from the odd-parity superconductors, a spin-singlet superconducting state can also be achieved in 2D Dirac fermions. Fu and Kane study the proximity effect between an s-wave superconductor and the surface states of a strong topological insulator. They predict that the resulting 2D state resembles a spinless superconductor and support Majorana bound states at vortices [102]. Following the pioneering work by Fu and Kane, Sato $et.\ al.$ predict that for ordinary fermions with a parabolic energy dispersion, it's possible to realize a topological superconductor that hosts Majorana zero modes when considering the Rashba spin splitting [103]. As for d-wave pairing superconductors, the proximity effect between a d-wave superconductor and surface Dirac fermions can induce a topological superconducting state [104]. Also, Majorana Fermions and topological order can exist in Nodal d-wave superconductors with strong spin-orbit coupling in an external magnetic field [105]. A fully gapped d-wave topological superconductor can be realized from gapless spin-singlet superconductors under a Zeeman field with a broken inversion symmetry and a broken time-reversal symmetry [106].

Equipped with multiple theories, lots of experimental efforts have been put in searching for real topological superconducting materials. Apart from the doped-Bi_2Se_3 system and Cd_3As_2 under high pressure, several other systems have been considered as candidates for topological superconductors. As a strongly correlated material, the superconductor Sr_2RuO_4 has been studied for more than 20 years since its discovery in 1994 [107]. Theory predicts a spin-triple p-wave pairing state [108, 109] which is supported by nuclear magnetic resonance (NMR) experiments [110] and muon spin rotation (μSR) experiments [111]. The spin-triplet odd parity indicates the topological nature of the superconductivity [112, 113, 114] which is evidenced by the edge states observed by in-plane tunneling spectroscopy [115]. Theory also predicts the symmetry-protected Majorana Fermions in Sr_2RuO_4 [116], which hasn't been experimentally confirmed yet. Half-quantum vortices have been observed in Sr_2RuO_4 by cantilever magnetometry measurements which could potentially host a Majorana zero mode in the vortex core [117]. However, recently, the p-wave superconducting state has been questioned a lot by contradictory experimental results. An NMR experiment shows a reduced spin polarization in unstrained samples when entering the superconducting state, which contradicts with the previous NMR result with no change in the Knight shift and questions the p-wave pairing scenario [118]. The specific heat measurement finds the line nodes in the superconducting gap, which calls for a reconsideration of the order parameter [119]. Recent thermal conductivity measure-

ments also found the gap structure of Sr_2RuO_4 consists of vertical line nodes, which is inconsistent with a p-wave order parameter [120]. The chiral edge states that are expected for a time-reversal-symmetry-breaking p-wave superconductor have not been detected yet [121, 122, 123]. All these contradictory results demand a re-evaluation of the pairing symmetry in Sr_2RuO_4.

Other candidates include the noncentrosymmetric superconductors [124, 125], such as $CePt_3Si$ [126], and nodal topological superconductors, such as the quasi 2D superconductor $Cu_x(PbSe)_5(Bi_2Se_3)_6$ [127], heavy-fermion superconductor UPt_3 [76] and half Heusler compound RPtBi [128, 129]. But solid experimental evidence is urgently required to verify their topological superconducting nature. A nearly ferromagnetic spin-triplet superconductivity is discovered in UTe_2 in 2019, which is characterized by a very large and anisotropic upper critical field exceeding 40 T and could potentially host topological excitations that are of interest for quantum computing [130].

Recently, a theory has predicted that the iron-based superconductor $Fe_{1+y}Te_{1-x}Se_x$ could host a topological superconducting state on its surface [131, 132, 133], which is evidenced by photoemission [134] and scanning tunneling spectroscopy measurements [135]. A zero-energy bound state (ZBS) has also been observed at magnetic-field-induced vortices in $Fe_{1+y}Te_{1-x}Se_x$ [135, 136, 137], which indicates a Majorana zero mode exists at the vortex core. Even more surprisingly, the robust ZBS was also found at each interstitial iron impurity by scanning tunneling microscopy in the absence of an external magnetic field [138]. Recently, a theory proposes that magnetic impurity ions can generate topological vortices without external magnetic fields in s-wave superconductors with strong spin-orbit coupling. These quantum anomalous vortices can even support robust Majorana zero-modes when the topological surface states are superconducting [139]. We are curious about how the topological vortices could affect the vortex flow in the vortex liquid state of a type-II superconductor. So we conduct the Nernst effect measurements in $Fe_{1+y}Te_{1-x}Se_x$ single crystals. More details will be discussed in Chapter 5.

CHAPTER 2

Experimental Techniques

In this chapter, we will introduce several experimental techniques that have been used to study the strongly correlated materials and topological superconductors. The development of a new torque differential magnetometry using the quartz tuning forks will be discussed in Chapter 2.1. This highly-sensitive magnetometry provides a powerful probe to resolve the electronic and magnetic anisotropy of novel solid state materials, such as the strongly correlated materials. Heat capacity measurement using the relaxation method will be introduced in Chapter 2.2. Thermal measurements, such as thermal conductivity, thermopower and Nernst effect measurements, will be discussed in Chapter 2.3.

2.1 Torque Differential Magnetometry Using the qPlus-Mode of a Quartz Tuning Fork

A quartz tuning fork is the key component of high-resolution atomic force microscope. Because of its high quality factor, a quartz tuning fork can also be used for high-sensitivity magnetometry. We develop a highly sensitive torque differential magnetometry using the qPlus mode of a quartz tuning fork [140]. The tuning fork is driven by an AC voltage, and its deflection is measured by the resultant AC current. We observe a sharp resonance of the quartz tuning fork at low temperatures down to 20 mK. We calibrate our torque differential magnetometry by measuring the angular dependence of the hysteresis loop in single-crystal $Fe_{0.25}TaS_2$. Furthermore, we demonstrate the high sensitivity of the torque differential magnetometry by measuring the quantum oscillations of a bismuth single crystal. The extracted Fermi-surface cross sections are consistent with those of bismuth crystals. To use the tuning fork magnetometry in a wet cryogenic system, we also make vacuum cells for the tuning forks which could hold a high vacuum at liquid Helium temperature. In the last part, we demonstrate the application of tuning fork magnetometry in a pulsed magnetic

filed up to 65 T by measuring the hysteresis loop and melting field of underdoped high-temperature superconductors $YBa_2Cu_3O_y$ (YBCO). The related publication can be found in Ref. [140].

2.1.1 Introduction on Quartz Tuning Forks

Quartz resonators have been widely used as frequency standards in wrist watches due to its low internal dissipation and insensitivity to accelerations [141]. Among them, quartz tuning forks(QTF) are the most useful because of the surprisingly high quality factor (Q-factor) and low frequency variation at room temperature. Furthermore, the relatively high spring constant k_{eff} provides additional advantages like smaller oscillation amplitude [142] and larger linear operation range [143].

QTFs were introduced into scanning near-field acoustic microscopy as a new method for imaging the topography of nonconducting surfaces by Günther *et al* [144]. Later on, QTFs were used to fulfill tip-sample distance control in near-field optical microscopes [145]. Shear force detection was used in these microscopes and was explicitly investigated by Karrai and Tiemann [146]. Implementation of a tuning fork sensor suitable for high-resolution atomic force microscopy(AFM) imaging was achieved by involving phase lock loop(PLL) control [147]. By attaching a magnetic tip on a QTF, magnetic force microscopy can bring a spatial resolution of several tens of nanometers [148, 149]. Giessibl *et al.* also demonstrated a new configuration of QTF based AFM (called qPlus sensor) which maintains both high scanning speed and atomic resolution [150].

Apart from the application in scanning probe microscopy, QTFs have a potential for the high-sensitivity magnetometry due to high quality factor Q ($\sim 10^4$) and high sensitivity [151]. Cantilever-based torque magnetometry with resolution better than $10^4 \mu_{\text{B}}$ was widely used to study small magnetization signal in magnetic thin layers [152] and individual nanotubes [153]. In these experiments, the read out of the magnetization signal usually involves mechanical oscillator drive and optical detection of cantilever deflection, often resulting in a cumbersome setup that is sensitive to the environment. It's necessary to develop an easy-to-set-up and highly sensitive magnetometry.

In the QTF-based torque magnetometry, magnetization coming from the sample generates a torque which changes the effective spring constant k_{eff} of the QTF. This change leads to a change in the resonance frequency. Thus it can be read out by its electrical response, such as current. Furthermore, cooling down to cryogenic temperature can effectively maximize the signal-to-noise ratio of the QTF [154][155]. This can, therefore, be a platform for a potentially easy-to-set-up sensitive magnetometry. However, QTF based

torque magnetometry has not been widely studied and lacks thorough understanding. A major reason is that the quality factor is very sensitive to the mass of attached specimen and will drop dramatically when the two prongs are not well balanced, making it impractical for resonant detection. Previous QTF-based torque magnetometry was investigated with attaching an iron wire to one prong of a free tuning fork [151]. There are no prior studies on qPlus-mode magnetometry where one prong is mechanically fixed.

In this chapter, we demonstrate that a qPlus-like setup of QTF, dubbed torque differential magnetometry, can achieve several times larger Q than prior non qPlus-like setup even with a relatively massive sample [151]. The QTF device is integrated on the rotator probe of a Janis Variable Temperature Insert(VTI) system which provides a low temperature and vacuum environment. We tested two different measurement circuits and achieved high sensitivity measurements in both low and high magnetic field. In order to calibrate the order of magnitude of magnetization measured with the quartz tuning fork, we measured the hysteresis loop of a well-studied ferromagnetic material $Fe_{0.25}TaS_2$ with different methods of magnetometry. Our analysis demonstrates that torque differential magnetometry can achieve a sensitivity which is comparable to that of the commercial Magnetic Property Measurement System (MPMS) as well as the cantilever-based torque magnetometer. Furthermore, we demonstrate the high sensitivity of our torque differential magnetometry by measuring the de Haas-van Alphen effect in the bismuth single crystal. Quantum oscillations are observed in a magnetic field up to 10 T and the extracted Fermi surfaces are consistent with previous results [156]. The observation of hysteresis loop, as well as the quantum oscillations, indicates that QTF-based magnetometry is a very promising characterization tool in studying the magnetic properties of many novel materials.

2.1.2 Application of Torque Differential Magnetometry in a DC Magnetic Field

2.1.2.1 Experimental Setup

Our experimental setup is shown in Figure 2.1 (a), one prong of the QTF is firmly glued on the side of an "L" shaped substrate with H74F epoxy from Epotek. Figure 2.1 (b) shows the side view of the experimental setup under the microscope. The "L" shaped substrate is machined from brass, which has high density and high thermal conductivity. Attaching a heavy mass to the tuning fork is crucial for obtaining a high quality factor. The sample is attached to the top of the free prong. The magnetic field is applied in the plane which formed by two crystalline axises (Inset of Figure 2.1 (b)). The QTFs (MS1V-T1K) are from Microcrystal with free standing resonance frequency $f_0 = 2^{15}$ Hz = 32768 Hz. The original

QTF is sealed in a metal case which holds a rough vacuum and can be gently removed with pliers. The spring constant of the quartz tuning fork can be calculated by the beam formula [157]

$$k = \frac{Et^3w}{4\triangle L^3}, \tag{2.1}$$

where E is Young's modulus of quartz, t the thickness, w is the width, and $\triangle L$ is the effective length. After plugging in the numbers from reference [142, 157], $\triangle L$ = 2400 μm, t = 214 μm, w = 130 μm and E = 79.1 GPa, the theoretical spring constant is approximately 1822 N/m. However, the calculation with the beam model is only a rough estimation for the spring constant and barely agree with the geometrical configuration of the qPlus sensors. The effective length $\triangle L = L - L_0$ is ambiguously defined since it highly depends on the mounting position L of the sample as well as the determination of the beam origin L_0 [158]. Furthermore, the assembling procedure, such as the non-symmetric alignment of the sample, will affect the spring constant of the QTF [159]. The rigid bonding between the sample and QTF, and between the QTF and substrate are crucial for obtaining a high Q [160]. The whole device is tightly fixed on a 16 pin socket which seats on the rotator probe of a Janis VTI system and stays in vacuum during the whole measurement.

In our experiments, we performed frequency dependent current measurements with the direct mode circuit shown in Figure 2.1 (c). A KEYSIGHT 33520B function generator is used to provide a 10mV AC voltage across the QTF. The voltage frequency is read by a KEYSIGHT 53230A frequency counter. At the same time, the responding current $\tilde{I}(\omega)$ due to piezoelectric effect is measured with a Stanford Research 830 lock-in amplifier whose reference signal comes from the function generator.

The field dependent current measurement is achieved with both a direct mode circuit and a phase lock loop (PLL) mode circuit (Figure 2.1 (d)). In the direct mode, the frequency of the function generator is always fixed at the resonance frequency of the QTF at zero field. When the magnetic field is changing, the magnetization in the sample generates a torque on the free prong of the QTF, which modifies the resonance frequency of the QTF. The lock-in amplifier measures the amplitude and phase of the current through the QTF. The phase shift of the current depends on how much the resonance frequency deviates from the excitation frequency. All data acquisition is fulfilled by Labview programming.

Compared with the direct mode, the PLL mode [147] can directly measure the frequency change of the QTF when applying a field. The shift of the QTF is quite steep at the resonance frequency [151] because of high Q factor. This slope can be used to convert the phase signal to the frequency change. In the PLL mode measurement, the drive frequency

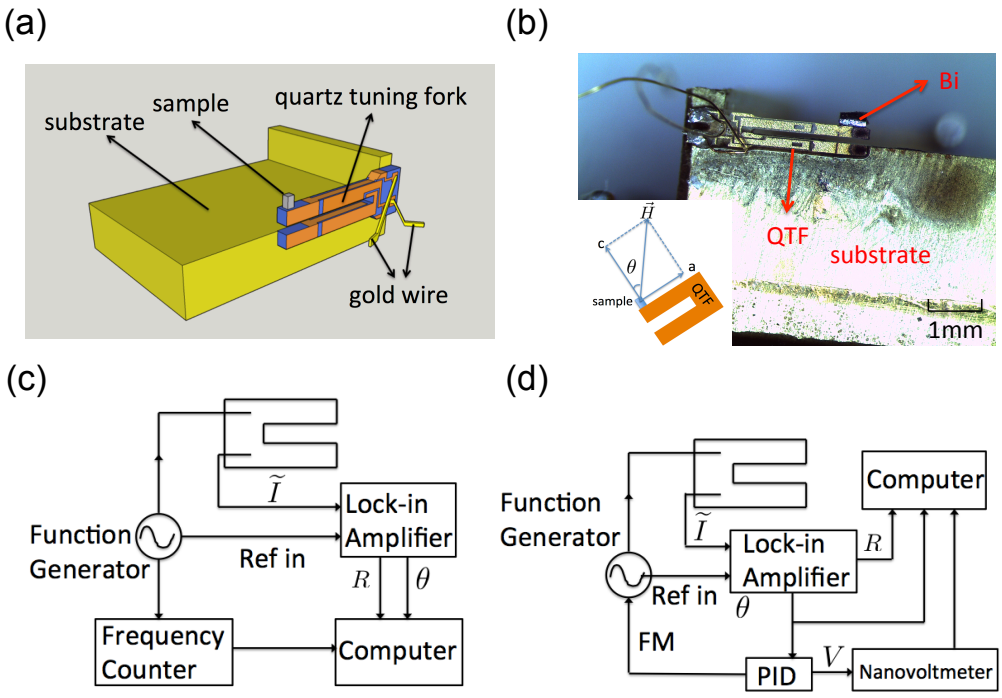

Figure 2.1: (a) Experimental setup. One prong of the QTF is firmly glued on the side of an "L" shaped substrate. The sample is attached on top of the free prong. (b) Side view of the experimental setup under the microscope. Inset shows the sketch of the measurement setup, where the magnetic field is applied in the ac plane of the sample. The sample stage is rotatable up to 90 degrees. θ is the angle between the c axis and H. Schematic of the experimental circuit: (c) direct mode and (d) PLL mode.

of QTF is modulated by a feedback loop to maintain constant phase. The phase lock loop is achieved by sending the phase of the current to the input of a Stanford Research SIM960 analog PID controller, while the output of the PID is used to modulate the frequency of the function generator and is recorded by a Keithley 2182A nanovoltmeter.

2.1.2.2 Theoretical Model: Torque Differential Magnetometry

In our experiment, the magnetization from the sample is represented by the frequency change of the QTF. Here we give a brief mechanical model which is similar to the mechanism of the frequency-modulated cantilever magnetometry [161]. In the qPlus configuration, only one prong of the QTF can oscillate freely while the other prong is tightly fixed on the substrate. The free prong is equivalent to a quartz cantilever which performs harmonic oscillation when applying AC voltage. In the PLL mode, the QTF is driven at its resonance

frequency ω_0 during the measurement. The displacement of the free prong is given by $x(t) = x_0 cos(\omega_0 t)$. In the presence of an external magnetic field H, the magnetization M from the sample applies a torque $\tau = M \times H$ on the QTF. The motion of the QTF can be expressed by

$$m_{\text{eff}} \frac{d^2x}{dt^2} + \gamma \frac{dx}{dt} + k_{\text{eff}} x = F_{\text{drive}} + F_\tau, \tag{2.2}$$

in which m_{eff} is the effective mass of the free prong, γ is the damping factor, k_{eff} is the effective spring constant, F_{drive} is the driving force and F_τ is the force coming from the magnetic torque. F_τ can be further expressed as $F_\tau = \tau / L_{\text{eff}}$, where L_{eff} is the effective length of the QTF. Here we define the angle between H and c axis to be the tilt angle θ. While the free prong keeps on oscillating, the motion adds a small oscillation change to the θ which makes $\theta^{'}(t) = \theta + \Delta\theta(t)$. $\Delta\theta(t)$ also varies with the same frequency ω_0 of the driving force and can be written as $\Delta\theta(t) = \Delta\theta_0 \cos(\omega_0 t)$, in which $\Delta\theta_0$ relates to the oscillation amplitude of the free prong $\Delta\theta_0 = x_0 / L_{\text{eff}}$. In other words, $\Delta\theta(t) = x(t)/L_{\text{eff}}$. The force change can be expanded as

$$F_\tau(\theta + \Delta\theta(t)) - F_\tau(\theta) \approx \frac{\partial F_\tau}{\partial \theta} \Delta\theta(t) = \frac{1}{L_{\text{eff}}} \frac{\partial F_\tau}{\partial \theta} x(t) \tag{2.3}$$

Therefore, the magnetic torque results in a change of effective spring constant

$$\Delta k_{\text{eff}} = k_{\text{eff}}^{'} - k_{\text{eff}} = \frac{1}{L_{\text{eff}}} \frac{\partial F_\tau}{\partial \theta} = \frac{1}{L_{\text{eff}}^2} \frac{\partial \tau}{\partial \theta}. \tag{2.4}$$

For a simple harmonic oscillator,

$$\omega_0 = \sqrt{\frac{k_{eff}}{m}}. \tag{2.5}$$

The shift of the resonance frequency can be written as

$$\Delta\omega_0 = \omega^{'} - \omega_0 = \sqrt{\frac{k_{eff}^{'}}{m}} - \sqrt{\frac{k_{eff}}{m}} = \sqrt{\frac{k_{eff} + \Delta k_{eff}}{m}} - \sqrt{\frac{k_{eff}}{m}} \tag{2.6}$$

$$= \sqrt{\frac{k_{eff}}{m}} [(1 + \frac{\Delta k_{eff}}{k_{eff}})^{\frac{1}{2}} - 1]. \tag{2.7}$$

We assume the change of the effective spring constant $\Delta k_{eff} = k_{eff}^{'} - k_{eff}$ is a small quantity. Using Taylor expansion and ignoring the higher order terms, we can get the

frequency change to be

$$\Delta\omega_0 \approx \sqrt{\frac{k_{eff}}{m}}(1+\frac{1}{2}\frac{\Delta k_{eff}}{k_{eff}}-1) = \sqrt{\frac{k_{eff}}{m}}\frac{1}{2}\frac{\Delta k_{eff}}{k_{eff}} = \omega_0\frac{\Delta k_{\text{eff}}}{2k_{\text{eff}}}. \tag{2.8}$$

So the shift of the resonance frequency becomes

$$\Delta\omega_0 \approx \omega_0\frac{\Delta k_{\text{eff}}}{2k_{\text{eff}}} = \frac{\omega_0}{2L_{\text{eff}}^2 k_{\text{eff}}}\frac{\partial\tau}{\partial_\theta}, \tag{2.9}$$

Therefore, in PLL mode the frequency shift is proportional to the derivative of the magnetic torque with respect to the tilt angle θ, which means the quartz tuning fork is actually a torque differential magnetometer [143].

When the magnetic field is applied in the ac plane of the crystal (Inset of Figure 2.1 (b)), the magnetic torque can be expressed with the components along crystalline c and a axis by

$$\tau = M_a H_c - M_c H_a. \tag{2.10}$$

For a paramagnetic or diamagnetic material [162],

$$\begin{aligned}\tau &= \mu_0\chi_a H_a H_c - \mu_0\chi_c H_c H_a \\ &= \mu_0\Delta\chi H^2\sin\theta\cos\theta,\end{aligned} \tag{2.11}$$

where μ_0 is the vacuum permeability and $\Delta\chi = \chi_a - \chi_c$ is the magnetic susceptibility anisotropy. With the same derivation, the frequency shift for a paramagnet material is

$$\Delta\omega_0 \approx \omega_0\frac{\mu_0\Delta\chi H^2\cos 2\theta}{2L_{\text{eff}}^2 k_{\text{eff}}} = \omega_0\frac{M_{\text{eff}}H\cos 2\theta}{2L_{\text{eff}}^2 k_{\text{eff}}}, \tag{2.12}$$

in which $M_{\text{eff}} = \mu_0\Delta\chi H$ is the effective magnetization.

If the sample is not paramagnetic along all crystal axises, the θ dependence of the frequency shift is a little bit different. Take $Fe_{0.25}TaS_2$ as an example, it is a paramagnet along a axis but a ferromagnet along c axis [163]. When the magnetization along c axis is saturated, the magnetic torque can be written as

$$\tau = \frac{1}{2}\mu_0\chi_a H^2\sin 2\theta - M_s H\sin\theta, \tag{2.13}$$

in which M_s is the saturation magnetization along c axis. In $Fe_{0.25}TaS_2$, the magnetization in ab plane is very low compared with the saturation magnetization along c axis [163]. As

a result, the frequency shift is following

$$\Delta\omega_0 = \omega_0 \frac{\mu_0 \chi_a H^2 \cos 2\theta}{2L_{\text{eff}}^2 k_{\text{eff}}} - \omega_0 \frac{M_s H \cos\theta}{2L_{\text{eff}}^2 k_{\text{eff}}}. \tag{2.14}$$

Further, given the magnetic torque is dominated by the second term in Eq. (9), the dominating term in Eq. (10) would be the second term, which means the frequency shift is proportional to H. Later we are going to demonstrate the angular dependence of the frequency shift at H_c in $Fe_{0.25}TaS_2$ single crystal.

2.1.2.3 Hysteresis Loop in $Fe_{0.25}TaS_2$

In order to calibrate the order of magnitude of the magnetic moment measured by the quartz tuning fork as well as verify the theoretical model of torque differential magnetometry, we measured the hysteresis loop of a well-studied ferromagnetic material $Fe_{0.25}TaS_2$ with different methods of magnetometry. The $Fe_{0.25}TaS_2$ sample used here were grown by chemical vapor deposition method [164]. Both the magnetic moment and resistivity are extremely anisotropic, with the magnetic moments aligned parallel to the c crystallographic direction [163, 164, 165].

Anisotropic magnetic moment was taken by a Quantum Design Physical Property Measurement System(PPMS) using the Vibrating Sample Magnetometer(VSM) option at 1.9 K. The sample measured in PPMS (Sample A) has a dimension of 0.9 mm $\times$ 0.75 mm $\times$ 0.05 mm. As shown in Figure 2.2 (a), a sharp hysteresis loop was observed when $H\|c$. The $H\|c$ magnetic moment saturates at 5.2 T($m_s \sim 10^{-3}$ emu) and is about 1 order of magnitude larger than the $H\|ab$ magnetic moment ($m_{ab} \sim 10^{-4}$ emu).

The angular dependent magnetic torque of Sample B was measured by the cantilever-based torque magnetometer. The experimental setup is similar to the one in reference [162], a 0.3 mm $\times$ 0.16 mm $\times$ 0.05 mm single crystal was put on the tip of a beryllium copper cantilever with a magnetic field applied in the ac plane. The magnetic torque τ coming from the sample is measured by tracking the capacitance change between the cantilever and a gold film underneath [166]. Figure 2.2 (b) shows the torque vs. H at $\theta = -34.8°$, in which θ is the angle between H and c axis. The bow-tie feature corresponds to the sharp jump in the magnetic moment at the coercive field H_c. As demonstrated in the previous session, the magnetic torque in this material is dominated by the second term in Eq. (9). So the torque signal should be proportional to sinθ. The loop height was defined as the torque change at the coercive field $\tau_c = \tau_c^{\text{up}}(H_c) - \tau_c^{\text{down}}(H_c)$. The angular dependent torque measurement was done from $-45°$ to $45°$. The angular dependent data shows that the loop closes exactly at $\theta = 0°$ and the loop size gradually increases as θ deviates from $0°$(Figure 2.2 (e)).

Theoretically, the torque signal should get a maximum at $\theta = \pm 45°$. Unfortunately, we were not able to get the angular dependence above $45°$ due to the limitation of our rotator. The angular dependent $\Delta\tau_c/2H_c$ data can be well fitted with Eq. (9) (red dashed line in Figure 2.2 (e)), which indicates the magnetic moment from the c axis is about 45 times larger than the contribution from the ab plane. In comparison, we also fit the angular dependent data with a sinusoidal function (blue dashed line). It turns out that with a large magnetic anisotropy, $Fe_{0.25}TaS_2$ can be approximated with a 3D Ising model.

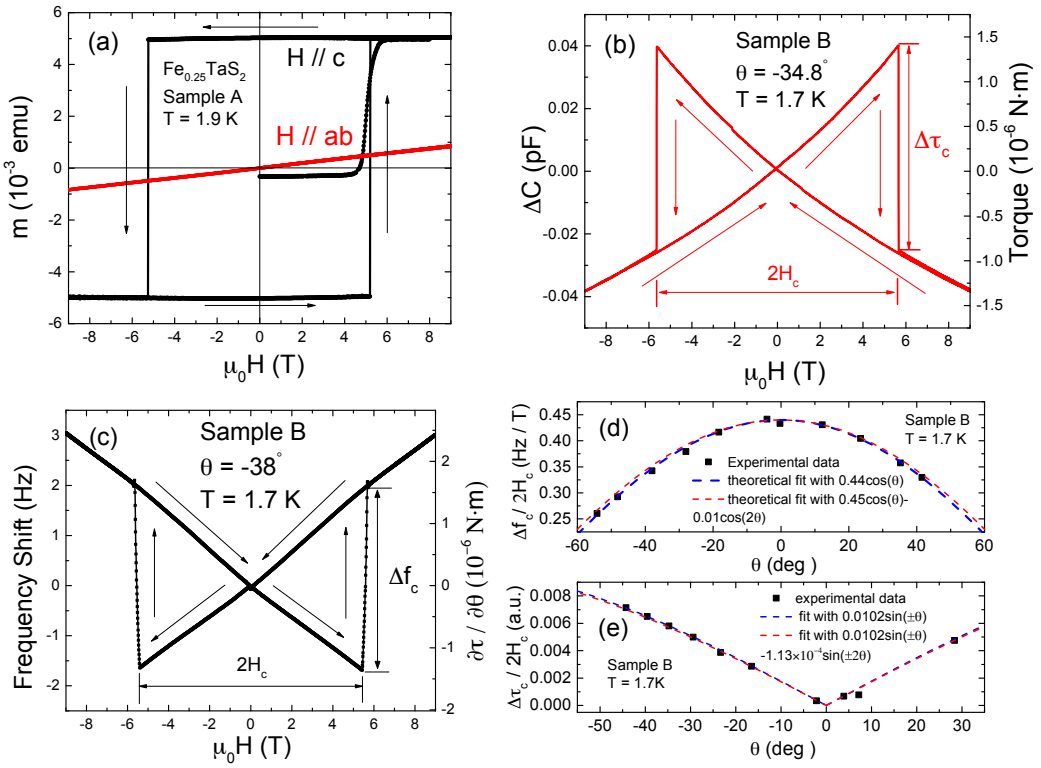

Figure 2.2: Hysteresis loop in $Fe_{0.25}TaS_2$. (a) $m(H)$ curves for $H\|c$ (black) and $H\|ab$ (red) measured by VSM in Sample A at 1.9 K. (b) Torque vs. H measured by torque magnetometer in Sample B at 1.7 K. (c) Frequency shift vs. H measured by quartz tuning fork in Sample B at 1.7 K. θ is the angle between H and c axis. The differential of torque is derived with Eq. (5). Arrows here denote the direction of magnetic field change. (d) $\Delta f_c/2H_c$ vs θ for the quartz tuning fork. (e) $\Delta\tau_c/2H_c$ vs θ for the cantilever. Blue dashed lines are the theoretical fitting with the magnetic moment only along the c axis. Red dashed lines are theoretical fitting with magnetic moment coming from both c axis and ab plane.

Sample B was then attached on the free prong of a qPlus-mode quartz tuning fork with the magnetic field applied in the ac plane. The field dependent frequency shift was measured by the PLL mode and the frequency shift vs H at $\theta = -38°$ was shown in Figure 2.2 (c). A similar hysteresis loop with a bow-tie feature was observed. Here the loop height

is defined as the frequency shift jump at the coercive field $\Delta f_c = f_c^{\text{up}}(H_c) - f_c^{\text{down}}(H_c)$, the loop width is defined as $2H_c$. The angular dependent hysteresis loops show that the loop height gets a maximum at $\theta = 0°$ and continuously increases as θ deviates from $0°$. Figure 2.2 (d) shows the angular dependent $\Delta f_c/2H_c$, which can be well fitted with Eq. (10) (red dashed line). The magnetic anisotropy derived from the fitting is consistent with the result of the cantilever data (Figure 2.2 (e)). If we treat the $Fe_{0.25}TaS_2$ sample as a 3D Ising system, the angular dependence of $\Delta f_c/2H_c$ can be well fitted with the second term of Eq. (10) (blue dashed line). This angular dependent behavior verifies that tuning fork is actually measuring the differentiation of magnetic torque instead of the torque itself. The coefficient in front of the cosθ in the fitting function equals to $\frac{f_0 M_s}{2L_{\text{eff}}^2 k_{\text{eff}}}$. The resonance frequency f_0 of the QTF with $Fe_{0.25}TaS_2$ sample attached is 30432 Hz, the effective length of QTF is $L_{\text{eff}} = 2.4$ mm, the saturation magnetic moment is $m_s = 3.55 \times 10^{-7}$ emu. Then the spring constant can be calculated to be $k = 2131$ N/m after plugging in all these numbers, which is consistent with the calculated spring constant in previous session and the reported values ($10^3 \sim 10^4$ N/m) in previous studies [150, 157, 167, 168].

2.1.2.4 Quantum Oscillations in Bismuth

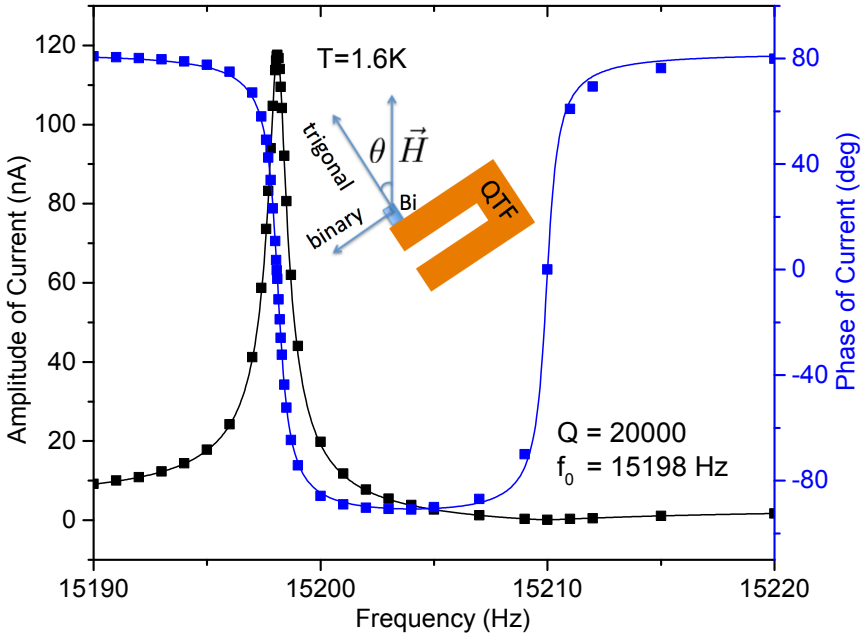

Figure 2.3: Resonance curve of the QTF with Bi sample attached at 1.6 K and in the vacuum. $Q = 20000$, $f_0 = 15198$ Hz. Inset is the configuration of the measurement. The magnetic field is applied in the trigonal-binary plane of the Bi crystal.

We also did the field dependent measurement for single crystal bismuth (Bi) with the qPlus-mode QTF. The orientation of the bismuth crystal is confirmed by X-ray diffraction. A 0.6 mm $\times$ 0.2 mm $\times$ 0.13 mm ($\sim$156 μg) bismuth (Bi) crystal is attached on the top of the free prong. The zero field resonance curve was measured with the direct mode at 1.6 K, as shown in Figure 2.3. The amplitude of the current shows a sharp peak at resonance frequency f_0 while the slope of the phase curve is quite steep. Fitting the magnitude and the phase of the current with Eq. (1) and (2) in reference [167] gives a quality factor around 20000 and $f_0 = 15198$ Hz. The phase of the current has a linear relationship with the frequency within ± 0.3 Hz around f_0, so we can use the phase deviation to infer the shift of the resonance frequency $\triangle f$ if $f_0 + \triangle f$ was in this linear range. However, strong magnetic torque in a high field could result in large frequency shift beyond the linear range. In this situation, the PLL mode has to be involved to track the variation of f_0 in a broad range.

To verify that the direct mode can produce the same result as the PLL mode in this linear range, field dependent measurements up to 10 T are performed with both modes. The crystal orientation is shown in the inset of Figure 2.3, the magnetic field is rotating in the trigonal-binary plane of the Bi crystal, θ denotes the angle between the field and the trigonal axis. Figure 2.4 (a) and (b) show that the frequency shift in the PLL mode and the phase of the current in the direct mode shows the same pattern(later we will compare the periodicity to $1/\mu_0 H$). Figure 2.4 (c) is the effective magnetic moment m_{eff} calculated from the frequency shift with Eq. (8). Comparing Figure 2.4 (a) with Figure 2.4 (b), the direct mode is better at revealing high frequency oscillations with respect to $\mu_0 H$ at low field. The reason is when the magnetic field changes, the magnetization of the sample changes the resonance frequency of the QTF and produces a phase shift on the current. With a sweeping rate of 0.23 T per minute, to obtain a stable PLL, the integration gain can not be too large, which means the time constant of the PLL can not be too small. The PID takes quite a long time to gradually reach a stable output which tunes the frequency of the function generator to the new resonance frequency. This feedback is not fast enough to catch the fast oscillations in the frequency. As a result, the direct mode has advantages in low field measurements since the phase of the current always responds more rapidly than the PID output.

In our experiment, we performed angular dependent measurements up to 10 T at 1.6 K. Figure 2.5 shows the raw data taken with the direct mode at 6 selected angles. When H is increasing, the Landau level energies are also increasing. Every time the Fermi surface passes through a Landau level, the derivative of free energy F over H has an extreme slope. Hence the Landau level crossings can be observed as a series of anomalies in the phase of the current versus H. If H was at an angle θ to the normal direction of a Fermi surface, the

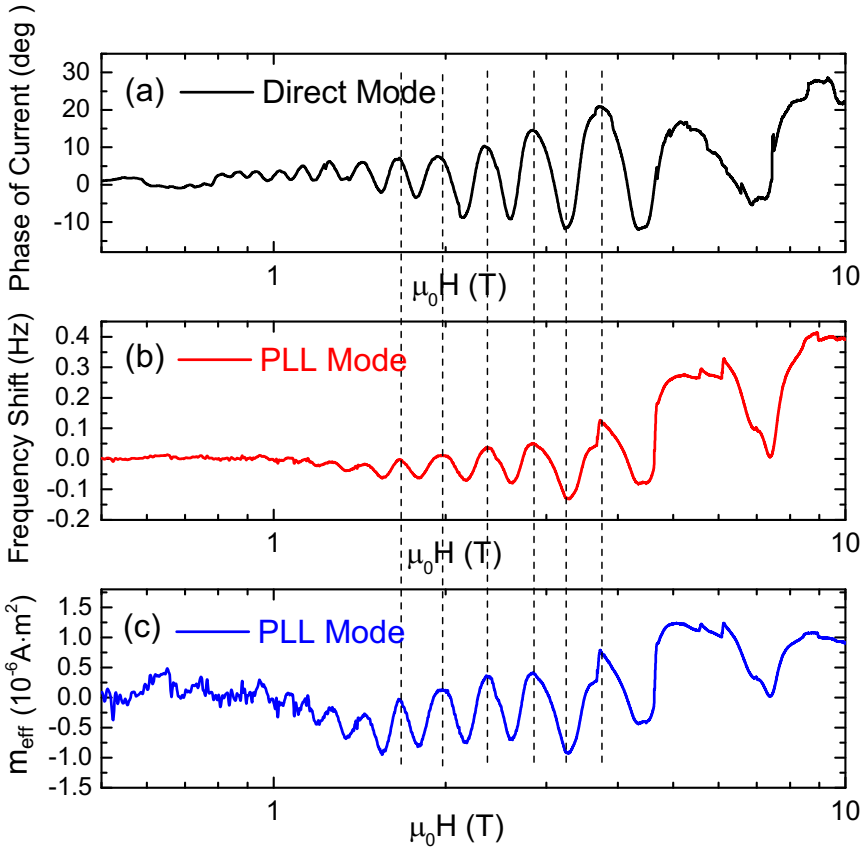

Figure 2.4: Quantum oscillations observed in the Bi crystal with two different measurement modes: (a) The phase of the current vs. H in the direct mode. (b) Frequency shift vs. H in the PLL mode. (c) Converted effective magnetic moment m_{eff} vs. H with Eq. (8) in the PLL mode. Here we used $k = 2131$ N/m from the fitting result of angular dependent $Fe_{0.25}TaS_2$ data for calculating m_{eff}. m_{eff} signal is quite noisy at low field. This is because m_{eff} is calculated through dividing the frequency shift by H, which is comparably a larger number at low field. All curves are taken at $\theta = -43°$, 1.6 K. Dashed lines are given as guides to the eye.

extreme slope happens at fields B_n given by [169]

$$\frac{1}{B_n} = \frac{2\pi e}{\hbar}(n+\gamma)\frac{1}{S(\theta)}, \tag{2.15}$$

where $\hbar$ denotes the reduced Plank constant, e is the electrical charge, n is a positive integer, γ is the Onsager phase, and $S(\theta)$ is the Fermi surface cross section at the magnetic field tilt angle θ. We use $(n, \pm)$ to denote the sub-Landau levels due to Kramers degeneracy. For the electron pocket, the index field B_n is distinguished by a minimum in the phase of the current, as shown in Figure 2.5 (a) - (e). For the hole pocket, B_n is revealed by peaks in the phase of the current, as shown in Figure 2.5 (f).

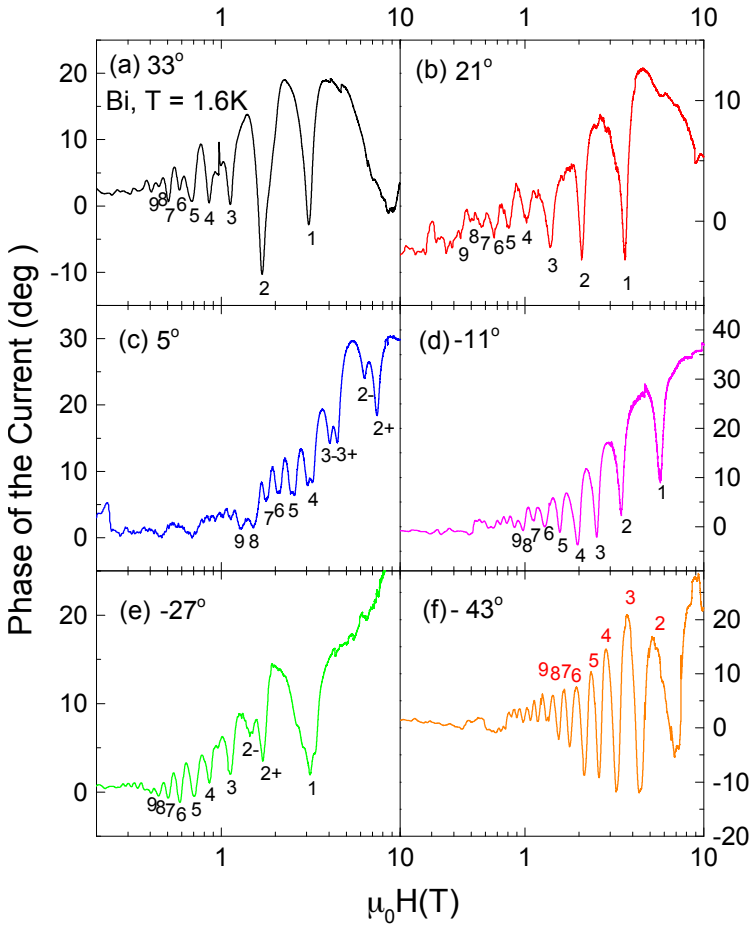

Figure 2.5: The phase of the current vs. H of the Bi crystal at six selected angles taken at 1.6 K (H is in log scale) with the direct mode. Crossings of the Landau sublevels (n, s) appear as extremes B_n in the phase of the current. $(n, +)$ and $(n, -)$ denote the splitting of degenerate Landau levels due to the Zeeman effect.

Landau level indices n vs. $1/B_n$ measured at three selected angles are plotted in Figure 2.6 (a). For the hole pocket, eg. $\theta = -43°$, the data points fall on a straight line which has an intercept of 0 as H approaches infinity. Whereas for the electron pocket, eg. $\theta = -11°, 33°$, the infinite field limit of the index plot intercept is around -0.2. This linear relationship confirms that the above indexing is consistent, the slope corresponds to the dominant quantum oscillation frequency at each angle, from which we can extract the Fermi surface cross-section projected on the plane perpendicular to H.

At each angle, quantum oscillations could come from both electron and hole pockets. Multi-frequencies of the quantum oscillations are revealed by the fast Fourier transform (FFT) of the field dependent phase data. A polynomial background has been subtracted before the FFT process. Figure 2.6 (b) shows the angular dependence of the quantum

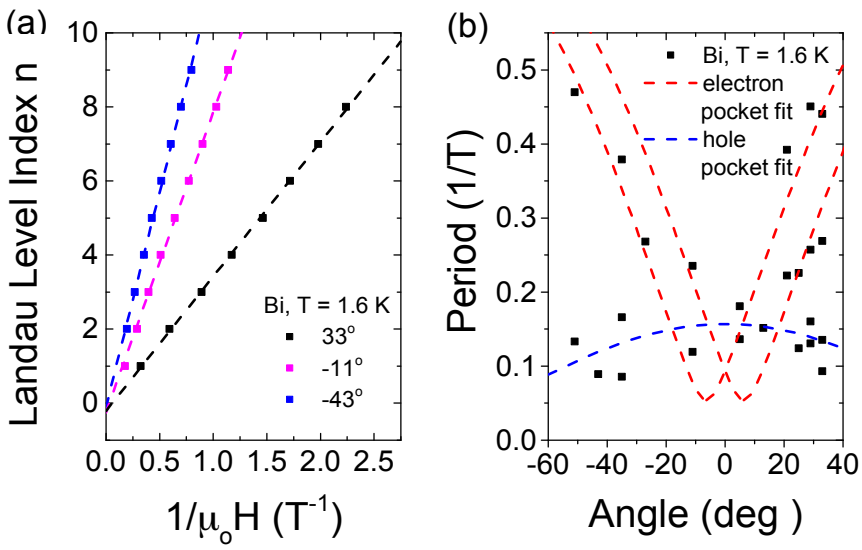

Figure 2.6: (a) Plot of the Landau level index n vs. $1/B_n$ at three selected angles. The Landau levels all fall on straight lines. The slopes give Fermi surface cross-section areas S_e at corresponding angles. (b) Oscillation periods of the observed Fermi surfaces is shown as a function of the angle between H and trigonal axis. Dashed lines are theoretical fittings from $-60°$ to $40°$ with a 3D ellipsoidal Fermi surface model. Red dashed lines represent two electron pockets while a blue dashed line denotes the hole pocket.

oscillation frequencies which can be fit with a 3D ellipsoidal Fermi surface model [169]. Red dashed lines denote quantum oscillation periods coming from two electron pockets which are symmetric with respect to the bisectrix axis. The blue dashed line represents the periods originating from the hole pocket that extends along the trigonal axis. Our results are consistent with previous de Haas-van Alphen measurements in Bi [156]. In the cantilever-based torque magnetometry measurement done by Li. *et* al. [170], the Bi sample has a mass of 0.12 g (770 times larger than our sample) and the quantum oscillation starts to show up at $B \sim 0.5$ T. With a much smaller sample, a quantum oscillation is revealed at a comparable magnetic field in our experiment, which indicates QTFs have advantages in small signal detection.

The electronic properties of Fermi surfaces can be revealed by tracking the temperature dependence and the magnetic field dependence of the quantum oscillation amplitude, which is well defined by the Lifshitz-Kosevich (LK) formula [169]. The oscillation amplitude is determined by the product of thermal damping factor R_T and Dingle damping factor R_D, as follows,

$$R_T = \alpha T m^*/B \, sinh(\alpha T m^*/B), \tag{2.16}$$

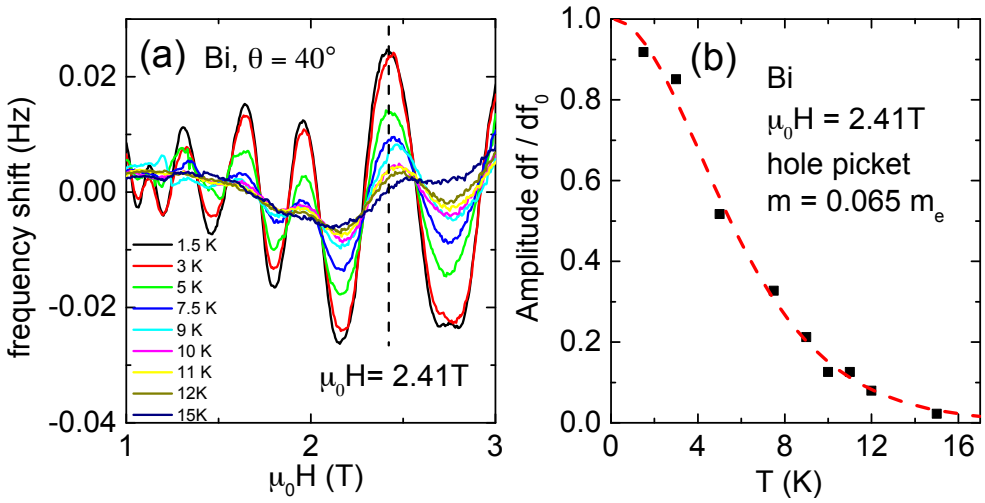

Figure 2.7: Temperature dependence of oscillating frequency shift for Bi. (a) Frequency shift after subtracting a polynomial background is plotted at T between 1.5 K and 15 K. θ is the angle between H and the trigonal axis. (b) Temperature dependence of the oscillating frequency shift at $\mu_0 H$ = 2.41 T, normalized by the 0 K limit. Fitting the oscillating amplitude to the LK formula (red dashed line) yields the effective mass m = 0.065 m_e for the hole pocket.

$$R_D = exp(-\alpha T_D m^*/B), \tag{2.17}$$

where the effective mass $m = m^* m_e$ and the Dingle temperature $T_D = \hbar/2\pi k_B \tau_S$. m_e is the bare electron mass, τ_S is the scattering rate, k_B is the Boltzmann Constant, and $\alpha = 2\pi^2 k_B m_e/e\hbar \sim 14.69$ T/K. Figure 2.7 (a) shows the temperature dependent frequency shift after subtracting a polynomial background between 1.5 K and 15 K. Fitting the temperature dependence of the normalized frequency shift at $\mu_0 H$ = 2.41 T yields m = 0.065 m_e for the hole pocket, which is within 20% error of the reported value in ref. [171].

After successfully detecting the quantum oscillation signals in bismuth single crystals in our VTI system, we move the setup onto a vacuum probe of the 31 T resistive magnet in the National High Magnetic Field Lab (NHMFL). A bismuth single crystal is mounted on the free prong of a qPlus QTF, with the crystal trigonal axis perpendicular to the free prong (as shown in Figure 2.8 (d)). The whole setup is glued on a straight probe by GE varnish. We conduct the field-dependent measurement by both direct mode and PID mode. Figure 2.8 (a) and (b) show the amplitude and phase of the current vs. B at several selected temperatures. The small wiggles below 5 T are quantum oscillation signals from bismuth. A big dip followed by a hug peak around B = 5 T indicates the magnetic field reaches the quantum limits. One interesting observation is two small kinks show up at B_1 = 20.7 T and B_2 = 25.2 T which already beyond the quantum limit. Then we repeat the measure-

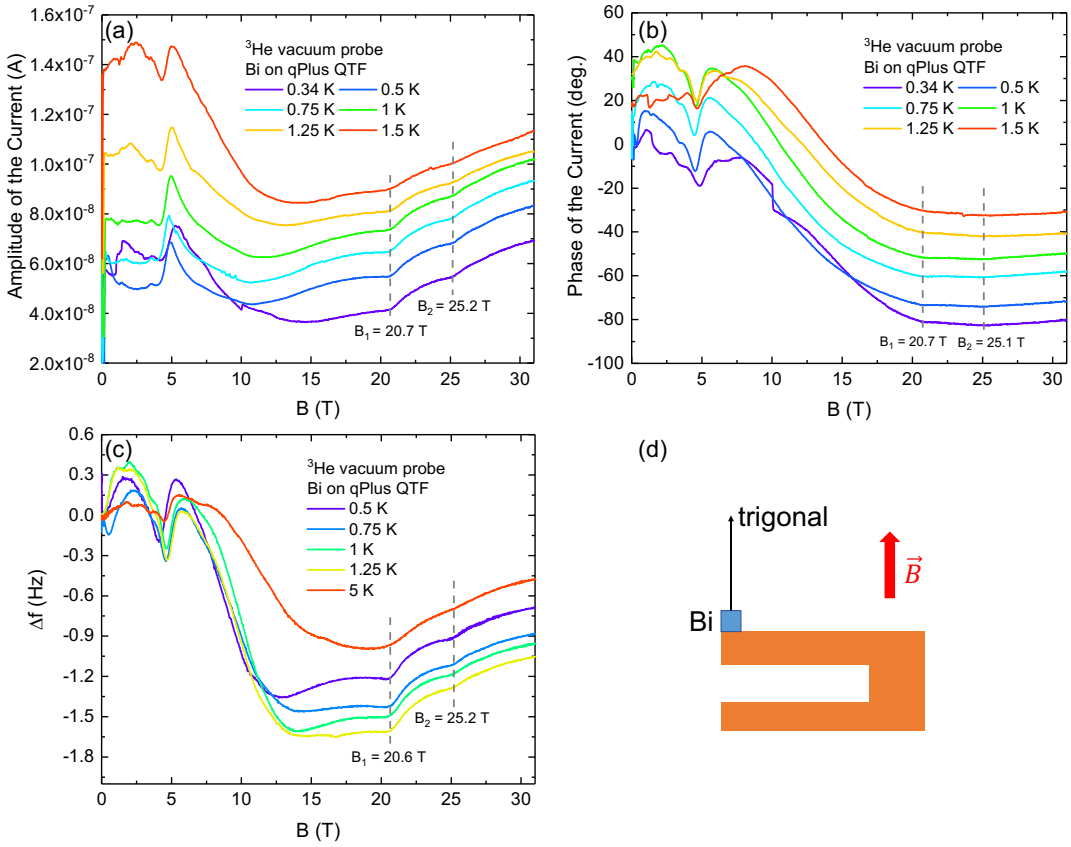

Figure 2.8: Field-dependent quantum oscillation signals in bismuth single crystals up to 31 T measured in a vacuum probe. (a) Amplitude and (b) phase of the current vs. B at several selected temperatures measured by the direct mode. (c) Resonance frequency shift Δf vs. B at several selected temperatures measured by the PID mode. (d) A bismuth single crystal is mounted on the free prong of a qPlus QTF, with the crystal trigonal axis perpendicular to the free prong. The magnetic field is applied along the trigonal axis.

ment with the PID mode and the resonance frequency shift shows consistent results (as shown in Figure 2.8 (c)). Similar results have been observed in bismuth single crystals by the Nernst effect measurements [172]. The Nernst coefficient presents three unexpected maxima which are deep in the ultraquantum limit. These maxima are concomitant with the quasi-plateaus in the Hall coefficient, which suggests that bismuth may host an exotic quantum fluid with a fractional quantum Hall effect and could be a signature of electron fractionalization in a 3D metal [172]. Later, this explanation is ruled out and another possible explanation, which relates the observation to the empty of Dirac valleys in elemental bismuth [173], is raised up after conducting more measurements beyond the quantum limit regime. More details will be discussed in Chapter 2.1.2.6.

In the next step, we test the QTF setup in the ^{3}He-system of the 31 T resistive magnet in NHMFL. A bismuth single crystal is mounted on a qPlus-configuration QTF. The QTF

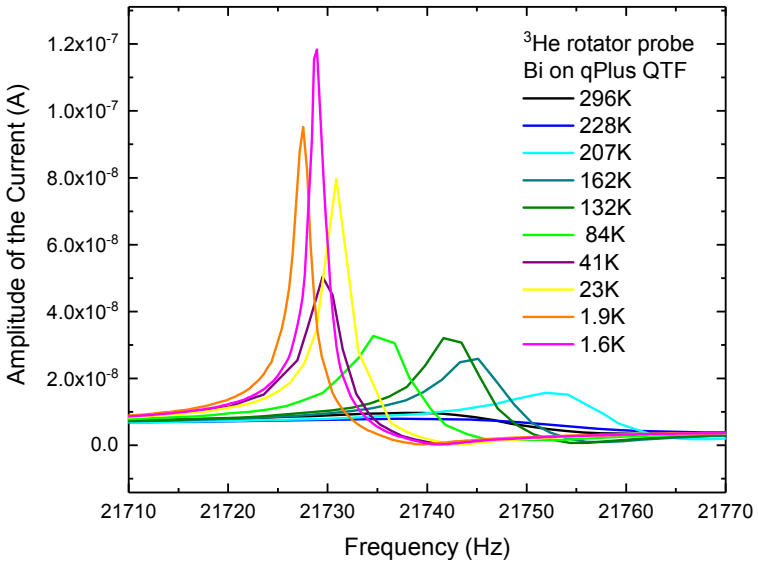

Figure 2.9: Temperature-dependent resonance curve for QTF with a bismuth single crystal. The QTF is mounted on a rotator probe in the ^{3}He system of the 31 T resistive magnet. A small amount of ^{3}He exchange gas is used to cool down the probe.

is glued on a rotator probe. Instead of seating inside a vacuum environment, the QTF is surrounded by a small amount of ^{3}He exchange gas which is used to cool down the whole probe. Figure 2.9 plots the temperature-dependent resonance curve of the QTF from room temperature to 1.6 K. As the temperature decreases, the resonance curve becomes sharper which indicates a larger Q factor. As the temperature changes from 300 K to 41 K, the resonance frequency decreases with the temperature. When the temperature is lower than 41 K, the resonance frequency shows a non-monotonic dependence with the temperature. Actually, the Q factor also shows non-monotonic dependence with the temperature in the low-temperature region ($T < 10$ K). This non-monotonic dependence of the resonance frequency and Q factor vs. temperature have been observed in other types of QTFs, such as QTFs with a resonance frequency of 192 kHz (as shown in Figure 2.14 (b)).

In order to reach the base temperature of 380 mK in a ^{3}He system, we have to condense ^{3}He liquid inside the probe and merge the sample socket into ^{3}He liquid. The condensation process of ^{3}He liquid contains several steps. First of all, we need to introduce a very important component in a ^{3}He system, the sorb. The sorb is made of charcoal and acts like a pump to absorb all ^{3}He inside when it is at low temperature ($T < 5$ K). When the sorb temperature is set at 15 K, it can release a small amount of ^{3}He which acts as exchange gas to cool down the whole probe during loading the probe. After the probe is fully loaded, we can set the sorb temperature to 45 K and it will release all the ^{3}He inside the charcoal. The released ^{3}He gas will be liquified by the 1K pot which locates below

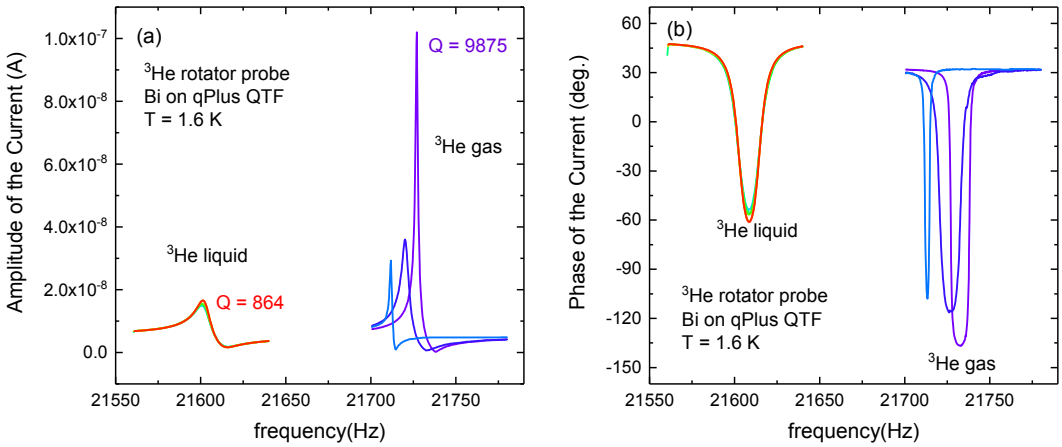

Figure 2.10: Resonance curve of the QTF with a bismuth single crystal in ^{3}He gas and ^{3}He liquid environments. (a) The amplitude of the current vs. frequency. (b) The phase of the current vs. frequency.

the sorb and ^{3}He liquid will drop into the ^{3}He pot which is located at the bottom of the probe. If the sorb stays at 45 K for long enough time (usually between 45 min to 1 hour), all the ^{3}He will be condensed into the ^{3}He pot. At this point, the whole sample socket will be merged inside ^{3}He liquid. During the ^{3}He condensation, the QTF will first stay in a ^{3}He gas environment and is finally surrounded by ^{3}He liquid. Figure 2.10 shows the resonance curve of the QTF when the environment changes. As the QTF stays in a ^{3}He gas environment, $Q \sim 9875$ at $T = 1.6$ K. Compare to the Q factor in the vacuum at the same temperature ($Q \sim 20000$ in Figure 2.3), the Q factor in a ^{3}He gas environment drops to one half. So the QTF is slightly damped by the ^{3}He gas. As the QTF is fully merged into ^{3}He liquid, Q factor drops dramatically to only 864 which is accompanied by a huge decrease of the resonance frequency for about 125 Hz. The dramatic decrease of the Q factor indicates a huge decrease in sensitivity, which means the same QTF setup is not able to detect a small signal that previously can be detected in a vacuum environment. This is the reason why we need to develop a vacuum cell for the QTF setup to use it in a liquid environment. We will introduce the vacuum cell setup in Chapter 2.1.2.6.

2.1.2.5 Discussion

The frequency sensitivity of the direct mode can be estimated in the following way. From the resonance curve of QTF with Bi sample attached (Figure 2.3), the slope of the phase vs. frequency is 132 deg./Hz. The main uncertainty of the direct mode measurement depends on the uncertainty of the phase measured by the lock-in amplifier. In our setup, the error from the phase measured by the lock-in is ± 0.5 deg, which means the frequency sensitivity

is about ± 3.8 mHz. This is about $7 \sim 8$ times higher than the frequency sensitivity achieved by the free tuning fork magnetometer [151].

As for the PLL mode, the major limitation for the sensitivity comes from the output of PID. Take the hysteresis loop measurement as an example, the uncertainty for the PID output is about 3×10^{-3} V, which corresponds to 1.8×10^{-3} Hz. The sensitivity of the saturation magnetic moment is estimated to be $\delta m_{\mathrm{s}} \sim 2.8 \times 10^{-10}$ A·m^2 $\sim 2.8 \times 10^{-7}$ emu at 5 T, which is comparable to the claimed best sensitivity of the latest MPMS (sensitivity $\sim 5 \times 10^{-8}$ emu) by Quantum Design. With the magnitude of our magnetic moment signal about 10^{-4} emu, the signal to noise ratio for our setup is 10^3. The sensitivity of QTF-based differential torque magnetometer is comparable to the sensitivity of cantilever-based torque magnetometer used for the hysteresis loop measurements. In our torque magnetometer experiment, the uncertainty of the beryllium-copper cantilever's capacitance is about 10^{-5} pF, which corresponds to a magnetic moment of 1×10^{-7} emu at 5 T. In the cantilever-based torque magnetometry, a thinner cantilever beam can achieve a higher sensitivity (10^{-10} emu). This is because a thinner beam has a lower spring constant, which makes the relative capacitance change ($\Delta C/C_0$) larger and has higher sensitivity. But it would not sustain the rather large torque signal from the ferromagnet (10^{-4} emu). Finally, we note that the majority of the frequency noise comes from the commercial analog PID feedback controller used in our electronics. In the future study, the performance and sensitivity of torque differential magnetometry can be improved by using a custome designed PLL with tunable bandwidth. The magnitude of M_{s} for $Fe_{0.25}TaS_2$ Sample B is about 10^{-4} emu, so the signal to noise ratio for our setup is 10^3.

The frequency sensitivity in the PLL mode is higher compared to the sensitivity in the direct mode, which is counterintuitive at the first glance. This is because the qPlus-mode QTF with the $Fe_{0.25}TaS_2$ sample attached has a 2.25 times larger Q compared to the QTF with Bi sample attached. As an approximate estimation, the slope of the phase curve for the $Fe_{0.25}TaS_2$ sample will be around ± 297 deg./Hz. This results in a frequency sensitivity about ± 1.68 mHz, which is smaller than the frequency sensitivity in the PLL mode (1.8 mHz). This comparison indicates that a higher Q can help a lot in increasing the sensitivity of the direct mode.

In conclusion, we developed a qPlus-like setup for torque differential magnetometry with the QTF. With the sample attached, the QTF maintains an excellent Q factor of $\sim 10^4$ at 1.6 K. Two different circuits for low and high field measurements maintain high sensitivity in both conditions. The hysteresis loop measurement in the ferromagnetic $Fe_{0.25}TaS_2$ single crystal proves that QTF can achieve a sensitivity of magnetic moment measurement at around 10^{-7} emu, which is comparable to other state-of-the-art magnetometers. The field

dependent measurement on the well-studied metal Bi gives solid evidence for the observation of quantum oscillations. Our measurements on ferromagnet and quantum oscillations demonstrated that our qPlus QTF magnetometry is a reliable method for conducting torque differential magnetometry measurements, especially at cryogenic temperatures and intense magnetic fields. Since the magnetic torque is the derivative of the free energy with respect to the tilt angle, the qPlus QTF magnetometry measures the second derivative of the free energy with respect to the tilt angle, thus providing a powerful probe to resolve the electronic and magnetic anisotropy of novel solid state materials.

2.1.2.6 Vacuum Cell for Quartz Tuning Forks

One vital problem with the application of QTF-based torque differential magnetometry is it must be used in a vacuum environment to achieve a high Q factor. The Q factor will be greatly damped if the QTF was merged in liquid helium. Unfortunately, most of the cryogenic systems in National High Magnetic Field Labs are wet systems, which means samples are directly merged into liquid ^{3}He or ^{4}He to achieve a maximum of the cooling power. To solve this problem, we machined a vacuum cell with brass to hold the QTF setup inside.

The size of the vacuum cell is limited by the sample space on the probe. For the SCM1 dilution refrigerator (magnet bore diameter 52 mm) in NHMFL, the 16-pin rotator probe can hold one 16-pin dip socket on top. The cross-section of the sample space on the 16-pin dip socket is 0.8 inch $\times$ 0.3 inch, which can fit two of our capacitive cantilevers at the same time. The height of the sample space is limited by the radius of the rotator probe, which is around 0.3 inch. We can also use a cylindrical socket rotator on the SCM1 rotator probe. A cylindrical socket rotator is designed to hold a cylindrical sample holder with a diameter of 0.45 inch or 0.5 inch. The length of a cylindrical holder should allow the rotator to turn in a cylinder with an inner diameter of 1 inch. The SCM2 He-3 system (magnet bore diameter 52 mm) can fit two 16-pin dip sockets on the rotator probe. So the available sample space on each 16-pin dip socket is comparable to it in SCM1. For the He-3 system in the 45 T hybrid magnet (magnet bore diameter 32 mm), we usually use a cylindrical socket rotator probe. The sample space of the cylindrical socket has a diameter of 0.451 inch and a length of 0.420 inch.

Figure 2.11 (a) shows the schematic of the vacuum cell, which contains a substrate and a cap. A QTF is mounted on the substrate with the qPlus configuration by H74F thermal epoxy. The cap and substrate are sealed together by Stycast 2850. For the sealing materials, we would like to use the ones that have comparable thermal contraction coefficient to brass since a not matching thermal contraction would result in a crack during cooling down.

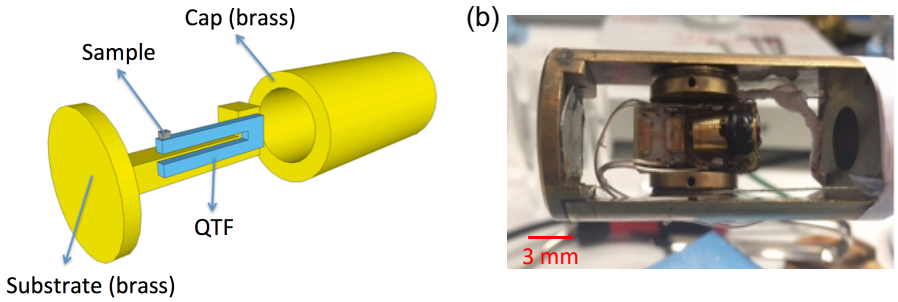

Figure 2.11: (a) Schematic of the structure of a vacuum cell with a QTF mounted. (b) A vacuum cell mounted on top of the 16-pin socket rotator probe of SCM1 in NHMFL.

Compared with Stycast 1260, Stycast 2850 has a thermal contraction coefficient closer to brass. Figure 2.11 (b) is a picture taken at SCM1 in NHMFL, which shows a vacuum cell (right-hand side) and a capacitive cantilever (left-hand side) mounted on top of a 16-pin socket rotator probe. When the vacuum cell is merged into liquid ^{3}He or ^{4}He, all the gas inside will condense into liquid and create a vacuum environment for the QTF.

To test the performance of the vacuum cell setup, a bismuth single crystal is mounted on the QTF. All data are taken with the PLL mode. At 20 mK, after applying a magnetic field up to 18 T, quantum oscillations are observed at multiple angles (as shown in Figure 2.12 (a)). The extracted frequencies are consistent with previous studies [174]. Then we move the same setup onto the cylindrical rotator probe of the 45 T hybrid magnet and apply a magnetic field up to 45 T at 380 mK. As shown in Figure 2.12 (b), the frequency shift of the QTF shows sharp kinks with respect to (w.r.t.) the magnetic field. The field range in the hybrid magnet (from 11.5 T to 45 T) is beyond the quantum limit of the bismuth crystal, which means all the electrons are already confined to the lowest Landau level. So the sharp kinks that show up above 11.5 T could relate to the empty of Dirac valleys in elemental bismuth [173]. The Fermi surface of elemental bismuth contains three electron pockets and one hole pocket. The three electron pockets are rotationally equivalent with an angle of 120 degrees [175], which offers a valley degree to the charge. One or two valleys would become empty when the magnetic field is higher than a critical field B_{empty}, which has been characterized by a large drop in the magnetoresistance at B_{empty} [173]. The carriers transfer from a high-mobility valley to a low-mobility valley at B_{empty}, which causes a

dramatic change of density of states. So we would expect a similar change in magnetic susceptibility at the same critical fields. In Figure 2.12 (c) and (d), we plot the locations of sharp kinks on frequency shift w.r.t. θ and compare them with the experimental results and theoretical fittings from reference [173] and [176]. Parts of our data are consistent with the previous study, but there are still branches that are missing from the previous study. We need to do the same measurements on more bismuth single crystals to verify whether the missing branches are intrinsic or due to sample dependence.

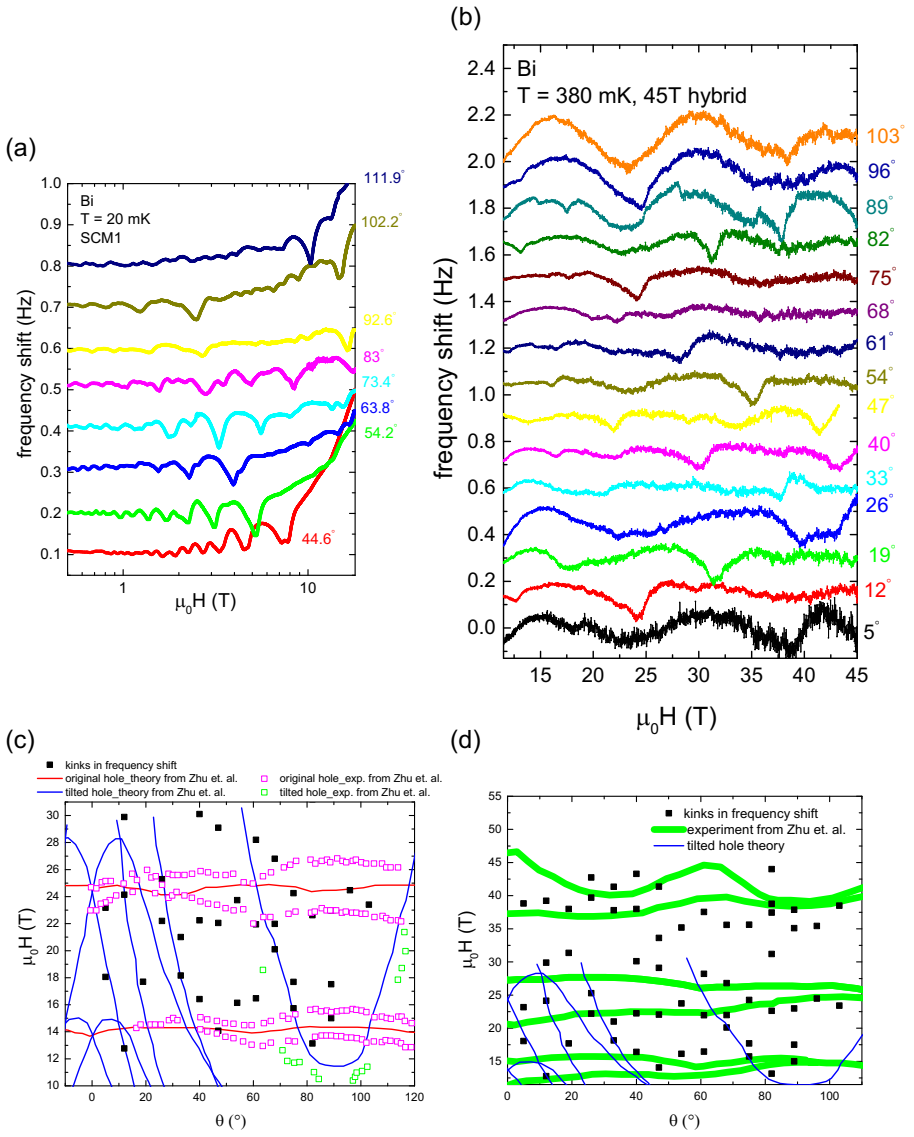

Figure 2.12: (a) Frequency shift vs. H of the Bi crystal taken at eight selected angles at 20 mK. Data are taken at SCM1 in NHMFL. (b) Frequency shift vs. H of the Bi crystal taken at fifteen selected angles at 380 mK. Data are taken at 45 T hybrid magnet in NHMFL. All data are taken with the PLL mode. θ is the angle between the magnetic field and the binary axis. (c) Black squares mark the locations of sharp kinks on frequency shift vs. θ from 11.5 to 32 T in Panel (b). Red and blue solid lines are theoretical fittings of original and tilted hole theory from reference [176]. Magenta and green squares are experimental data of original and tilted hole theory from reference [176]. (d) Black squares mark the locations of sharp kinks on frequency shift vs. θ from 11.5 to 45 T in Panel (b). Blue solid lines are theoretical fittings of tilted hole theory from reference [173]. Green solid lines are experimental data from reference [173].

2.1.3 Application of Torque Differential Magnetometry in a Pulsed Magnetic Field

Apart from the DC magnetic field, QTFs could potentially be used in a pulsed field up to 65 T as well. As an insulator, quartz does not have a problem with eddy currents present in metal cantilevers, which can be a important issue due to the rapid magnetic field change rate in the pulsed field. Furthermore, the resonance frequency of the QTF is much higher than that of the traditional cantilever ($\leq$ 100 Hz), which reduces the coupling between the QTF signal and low frequency mechanical vibration coming from the environment. The magnetic field profile of a 65 T pulsed magnet is plotted in Figure 2.13. It takes 8 ms for it to reach a field of 60 T and another 48 ms to sweep down to zero. A much faster sweeping speed of the pulsed magnet (compared to 0.3 T/min in the superconducting magnet and 3 T/min in the resistive DC magnet) requires the setup has a much faster responding speed. The response time of magnetometry needs to be much smaller than the sweep-up time of the pulsed field (about 8 ms). Therefore, a QTF with higher resonance frequency is desirable in the pulsed field measurement.

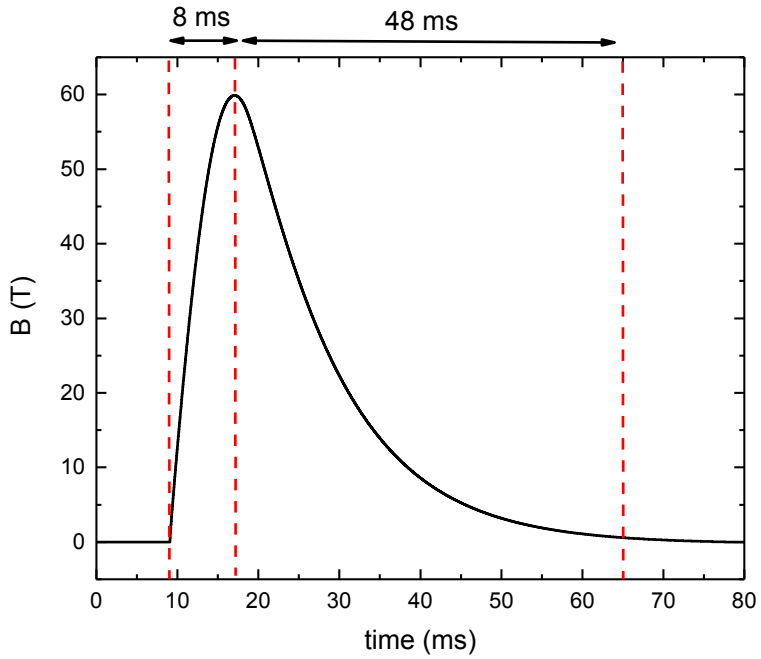

Figure 2.13: The magnetic field vs. time for a 65 T pulsed magnet. It takes around 8 ms for the magnet to reach the highest field and 48 ms to sweep down to zero.

We choose QTF that has a resonance frequency of 192 kHz for the application in the pulsed magnetic field. Figure 2.14 (a) shows the picture of a 192 kHz quartz tuning fork mounted with a qPlus configuration. A $YBa_2Cu_3O_{6.55}$ ($YBCO_{6.55}$) single crystal (sample

size 0.1mm $\times$ 0.1 mm $\times$ 0.2mm) is mounted on top of the free prong. The 65 T multi-shot magnet has a bore size of only 15 mm. So the sample space is more limited than the 18 T DC superconducting magnet, which has a bore size of 52 mm. The huge eddy current generated during the magnetic pulse makes brass a bad choice for the substrate. We use 20 mil thick sapphire as a substrate for QTFs used in the pulsed magnetic field. The substrate is mounted on a straight probe with GE varnish.

The probe is cooled down in ^{4}He exchange gas. The resonance curve is taken by the direct mode. The measurement circuit for the direct mode is shown in Figure 2.14 (b). A 100 mV voltage is applied across the QTF to drive it into resonance. Due to the high resonance frequency ($f \sim 167$ kHz), an SR 844 200 MHz lock-in amplifier was used to measure the response. SR 844 doesn't have a current mode. So an SR 570 low-noise current preamplifier is connected right after the QTF to convert the current signal into a voltage signal. Another SR 560 low-noise voltage preamplifier is connected after the SR 570 to further increase the voltage signal. The output signal of SR 560 is sent into the voltage input of SR 844. The temperature-dependent resonance curve of QTF with $YBCO_{6.55}$ Sample 1 is shown in Figure 2.14 (c). The resonance frequency shifts to lower frequency during cooling down and the change of Q factor is nonmonotonic to temperature.

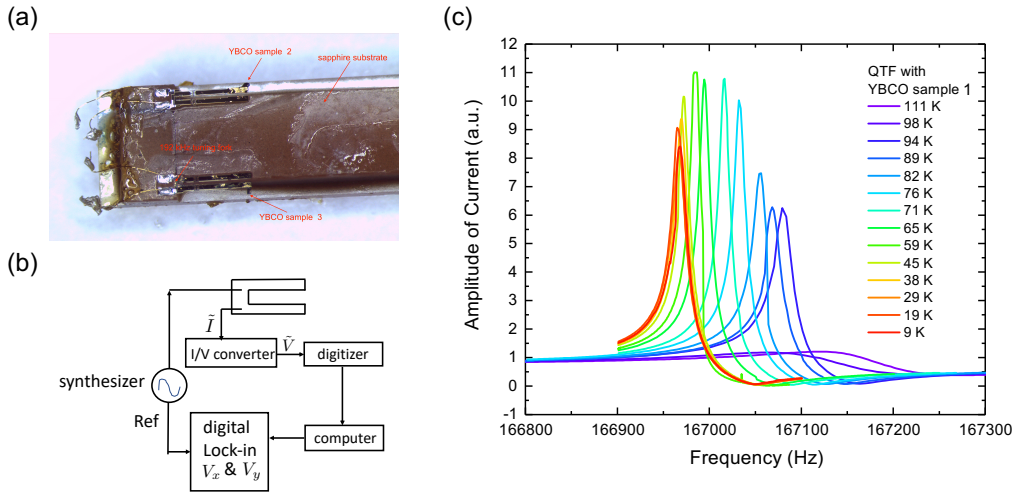

Figure 2.14: (a) Experimental setup for 192 kHz QTFs in a qPlus configuration. Two quartz tuning forks are mounted on a T-shaped sapphire substrate. The resonance frequency of QTF with YBCO Sample 2 mounted is 177.778 kHz and 167.001 kHz with $YBCO_{6.55}$ Sample 1 mounted. (b) Measurement circuit which is similar to the direct mode in Figure 2.1 (c). (c) Temperature-dependent resonance curve for QTF with Sample 1. It has a Q factor of 7950 at T = 9 K in ^{4}He exchange gas.

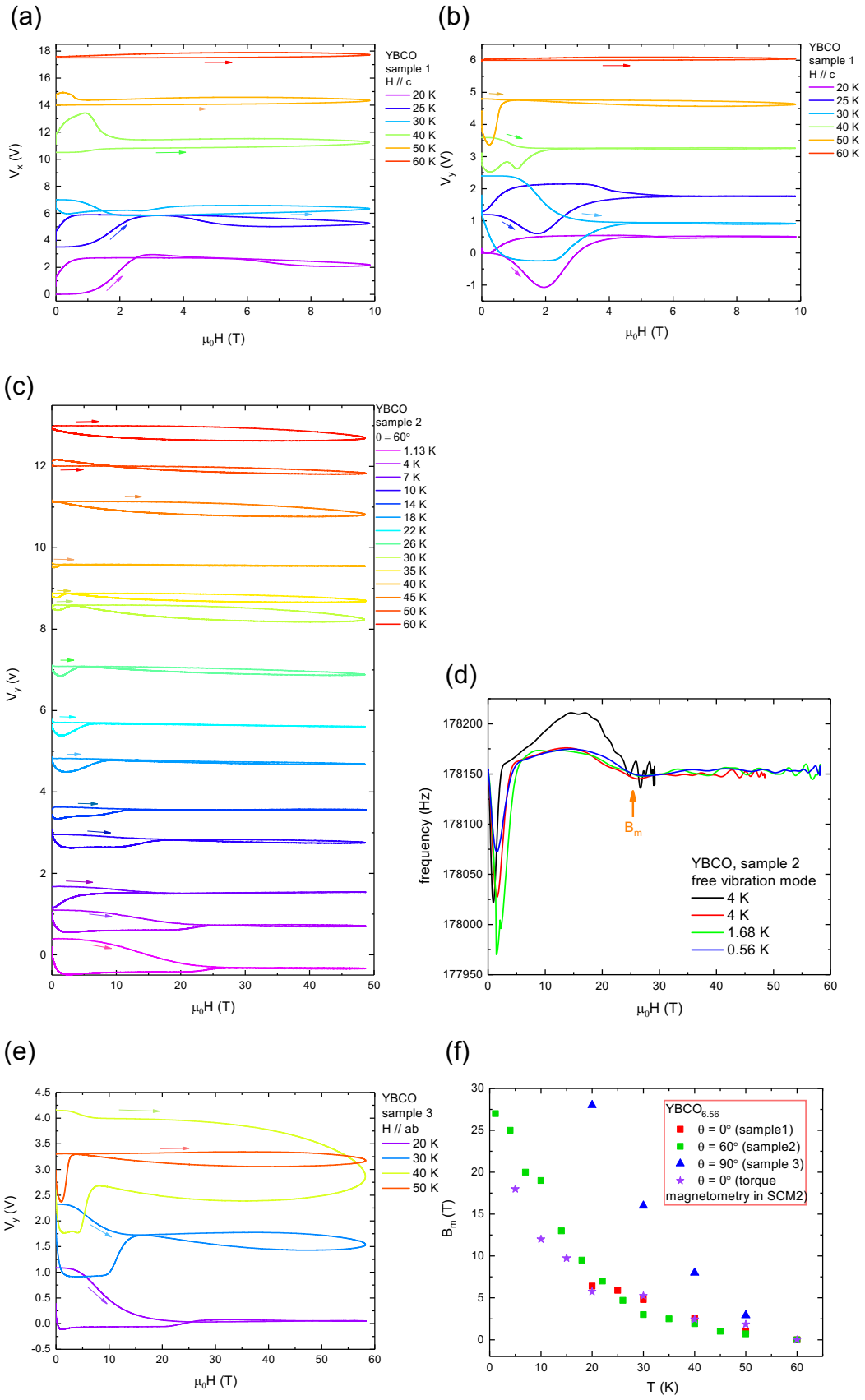
(a)
YBCO
sample 1
H // c
20 K
25 K
30 K
40 K
50 K
60 K
V_x (V)
μ_0H (T)
(b)
YBCO
sample 1
H // c
20 K
25 K
30 K
40 K
50 K
60 K
V_y (V)
μ_0H (T)
(c)
YBCO
sample 2
θ = 60°
1.13 K
4 K
7 K
10 K
14 K
18 K
22 K
26 K
30 K
35 K
40 K
45 K
50 K
60 K
V_y (v)
μ_0H (T)
(d)
frequency (Hz)
B_m
YBCO, sample 2
free vibration mode
4 K
4 K
1.68 K
0.56 K
μ_0H (T)
(e)
YBCO
sample 3
H // ab
20 K
30 K
40 K
50 K
V_y (V)
μ_0H (T)
(f)
$YBCO_{6.56}$
θ = 0° (sample1)
θ = 60° (sample2)
θ = 90° (sample 3)
θ = 0° (torque magnetometry in SCM2)
B_m (T)
T (K)

Figure 2.15: Hysteresis loop and melting field B_m of vortex solid states measured in $YBCO_{6.55}$ Sample 1, 2 and 3. (a) X and (b) Y components of voltage vs. H measured at selected T with the direct mode for $YBCO_{6.55}$ Sample 1. H is applied along the crystal c axis. A clear hysteresis loop can be observed. The loop closing field is defined as the melting field of the vortex solid state. (c) Y components of voltage vs. H measured at selected T with the direct mode for $YBCO_{6.55}$ Sample 2. H is applied with an angle of 60° w.r.t the crystal c axis. (d) The resonance frequency vs. H measured with the free vibration mode in $YBCO_{6.55}$ Sample 2. The orange arrow denotes the melting field B_m. (e) Y components of voltage vs. H measured at selected T with the direct mode for $YBCO_{6.55}$ Sample 3. H is applied in the crystal ab plane. (f) Melting field B_m vs. T in $YBCO_{6.55}$ Sample 1, 2 and 3. The data taken by capacitive torque magnetometry in SCM2 is also plotted as a comparison. In (a), (b), (c) and (e), the arrows represent the field sweeping direction.

We develop two different methods to conduct the field-dependent measurement. The first method is the direct mode (as shown in Figure 2.14 (b)), which is the same setup that is used to measure the resonance curve in Figure 2.14 (c). The QTF is driven at its resonance frequency before the magnetic pulse. During the pulse, the driving voltage is stilled applied with the same frequency. The X and Y component of voltage (equivalent to the current going through the QTF) measured by the digital lock-in are recorded at the same time to show the response coming from the sample magnetization.

The second method is the free vibration mode [177]. The QTF is first driven into its resonance frequency. Right when the pulse starts, the driven voltage is cut off which leaves the QTF to do free vibration. The vibration amplitude will gradually decay with time. During the magnetic pulse, the current going through the QTF is monitored by converted it into a voltage signal and sent it to a fast digitizer. Then this voltage signal is analyzed by a digital lock-in to extract the frequency. So we will have the resonance frequency vs. magnetic field at the end of the measurement. The change of the resonance frequency indicates the magnetization response coming from the sample.

We measure three $YBCO_{6.55}$ samples with different magnetic field orientations to study the hysteresis loop of type II superconductor and melting field of vortex solid state. For $YBCO_{6.55}$ Sample 1, H is applied along the crystal c axis. For $YBCO_{6.55}$ Sample 2, H is applied with an angle of 60° w.r.t the crystal c axis. For $YBCO_{6.55}$ Sample 3, H is applied in the crystal ab plane. First, we use the direct mode to measure the X and Y components of the voltage signal during the magnetic pulse. Figure 2.15 (a), (b), (c) and (e) show that hysteresis loops are observed in both V_x and V_y when T is below 60 K. The loop size decreases when T increases and finally closes at the critical temperature ($T \sim 60$ K). The field location where the hysteresis loop closes is defined as the melting field B_m of the vortex solid state. The magnetization signal in the superconducting state is much larger than the

normal state. The magnetization signal is also much bigger when H is applied inside the ab plane. So for Sample 3, we are only able to get a reasonable signal when T is above 20 K. For Sample 2, we also try the free vibration mode. But the vibration amplitude damps a lot during the upsweep, the vibration of QTF almost stops at the end of the upsweep. So it's hard to get any reasonable data during the down sweep.

Figure 2.15 (d) plot the resonance frequency vs. H measured with the free vibration mode in $YBCO_{6.55}$ Sample 2. A clear hump can be observed between 5 T and 25 T. The resonance frequency almost doesn't change when H is higher than 25 T, which indicates the entering of the vortex liquid state. The field locations are consistent with the melting fields observed with the direct mode (as shown in Figure 2.15 (c)). The melting field B_m vs. T of Sample 1, 2 and 3 are plotted together in Figure 2.15 (f). The data taken by capacitive torque magnetometry in SCM2 is also plotted here as a comparison. The melting field B_m vs. T measured by capacitive torque magnetometry is consistent with the result measured by QTF. They are also consistent with the results obtained by other measurements [178].

2.2 Heat Capacity Measurement

Heat capacity is defined as the amount of heat to be supplied to a given mass of a material to produce a unit change in its temperature. The measurement of the heat capacity of solid-state materials can provide information about the lattice, electronic, and magnetic properties of materials. The heat capacity that has been measured in our experiment is heat capacity at constant pressure

$$C_p = (\frac{dQ}{dT})_p \tag{2.18}$$

We use the heat capacity option in the PPMS system, which adopts the relaxation method to measure heat capacity. The schematic of the sample platform is shown in Figure 2.16. A heater and thermometer are mounted to the bottom side of the sample platform. Four metallic wires are used to provide the electrical connection to the heater and thermometer and also the mechanical support to the sample platform. The sample was mounted on the top side of the sample platform by a thin layer of Apiezon grease. The Apiezon N grease can be used to do low-temperature measurement while the Apiezon H grease performs better at high temperatures. Since the N grease exhibits a slight anomaly in its specific heat near it melting point and only has 5% reproducible heat capacity in the temperature range of 260 K to 325 K. It is recommended to only use the Apiezon N grease at temperatures below 220 K. Below 200 K, the H grease has a tendency to spontaneously pop off which causes loss of grease. For the best results, only use the H grease for temperatures above 200

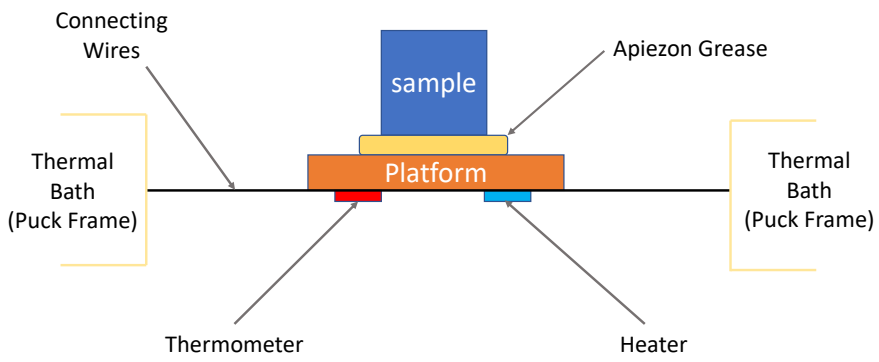

Figure 2.16: Thermal Connections to Sample and Sample Platform in PPMS Heat Capacity Option [179].

K. If you need to work over the entire temperature range, the N grease is a better choice since there will be no loss of grease from it popping off. More details can be found in section 6.2.4 of the PPMS Heat Capacity Option User's Manual. The PPMS can provide a high vacuum environment when measuring the heat capacity. So the thermal conductance between the sample platform and the thermal bath (puck) is totally dominated by the conductance of four metallic wires. The heat loss to the environment through conduction or thermal radiation can be negligible.

During a heat capacity measurement, we have to add heat to and remove heat from the sample while monitoring the change in sample temperature. For the relaxation method, one measurement cycle contains a heating period followed by a cooling period. The heat capacity option software will fit the temperature response of the sample platform to a theoretical model that accounts for both the thermal relaxation of the sample platform to the bath temperature and the relaxation between the sample platform and the sample itself. One big assumption for the fitting technique is the sample heat capacity is almost constant over the temperature range covered by a single measurement cycle. In order to analyze the heat capacity across a first-order phase transition, the advanced slope analysis can be used.

We will use a simplified one-dimensional model to explain the relaxation method (as shown in Figure 2.17 (a)) [180]. We assume the heat diffusion within the sample and between the sample and platform is much faster than the diffusion between the platform and the thermal bath. When a heat pulse is applied to the sample platform with a constant power P, the power that goes into the sample is equal to the power goes out plus the power that used to raise up the sample temperature or

$$P = A\kappa\frac{\partial T}{\partial Z} + C(T)\frac{\partial T}{\partial t} \tag{2.19}$$

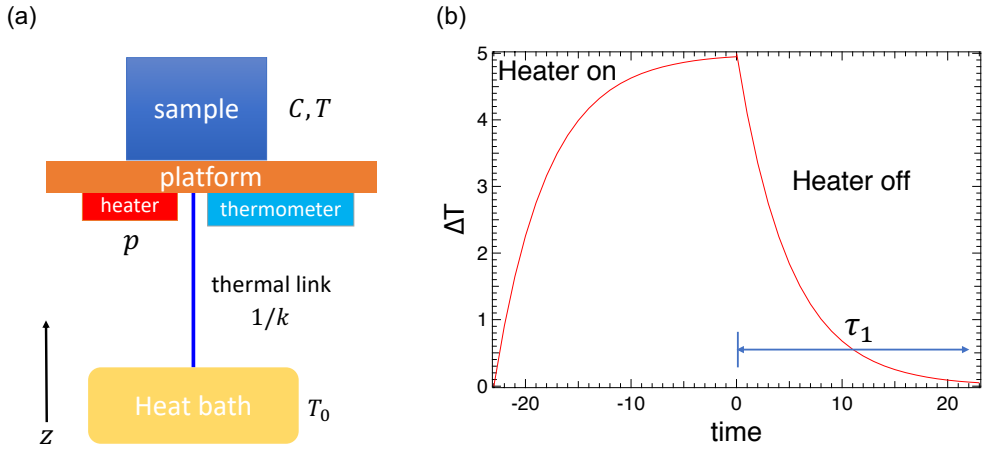

Figure 2.17: (a) Schematic of heat flow. (b) Temperature vs. time during one measurement circuit. τ_1 is the relaxation time of temperature.

Where P is the heater power, A is the cross section of the wire, κ is the thermal conductivity of the wire, z is the heat flow direction. Integrate over the length of the wire,

$$C(T) = (\frac{dT}{dt})^{-1}[P - \int_{T_0}^{T} k(T^{'})dT^{'}] \tag{2.20}$$

where $k(T) = \kappa(T)\frac{A}{l}$ is the thermal conductance of the wire. When the temperature rise in one heat cycle is small, the thermal conductance of the wire is almost a constant, the integral will become

$$\int_{T_0}^{T} k(T^{'})dT^{'} = k(T_{av})\triangle(T) \tag{2.21}$$

$$T_{av} = \frac{1}{2}(T + T_0) \tag{2.22}$$

$$\triangle(T) = T - T_0 \tag{2.23}$$

If the heater is turned off at $t = 0$, we have

$$C = -\frac{k(T_{av})}{d(ln\triangle T)}/dt \tag{2.24}$$

If C is constant over the temperature range between T and T_0,

$$\frac{d(ln\triangle T)}{dT} = -\frac{1}{\tau_1} = -\frac{k}{C} \tag{2.25}$$

So we will have

$$\triangle T(t) = (T_1 - T_0)\exp(-t/\tau_1) \tag{2.26}$$

which means the temperature will decay exponentially after the heater power is switched off (as shown in Figure 2.17 (b)). In the real experiment, we can track the temperature during the whole thermal cycle and fit with equation (2.26) to extract the value of τ_1. Then from equation (2.25), the heat capacity can be calculated as

$$C = k\tau_1 \tag{2.27}$$

The measurement mentioned above measures the heat capacity at each temperature separately. If we want to get a continuous reading of heat capacity across a certain temperature range, such as the superconducting transitions or narrow ordering peaks, we can adopt the sweep method. More details can be found in reference [180].

Measuring the sample's heat capacity usually contains several steps. Before measuring the heat capacity of the sample, we have to calibrate the puck frame first, which means to only measure the heat capacity of the puck frame. After the calibration, applying a thin layer of Apiezon grease on the sample platform and measuring the heat capacity of the grease plus the puck, which is called the addenda. The last step is to mount the sample on top of the grease (the exactly same grease that has been measured in the last step) and measure the whole heat capacity again. The sample's heat capacity would be the whole heat capacity subtract the addenda's heat capacity. Remember, whenever we have to switch to another sample, the addenda have to be measured again in order to minimize the error. An example of heat capacity measurement in a superconducting sample will be introduced in Chapter 4.

2.3 Thermal measurements

2.3.1 Thermal Conductivity Measurement

A material's thermal conductivity measures its ability to conduct heat. Materials with high thermal conductivity are widely used as heat sinks, such as copper, and materials with low thermal conductivity are used as thermal insulation, such as fiberglass and Styrofoam. According to Fourier's Law for heat conduction, thermal conductivity κ is define as

$$\mathbf{q} = -\kappa\nabla T \tag{2.28}$$

where $\mathbf{q}$ is the heat flux and ∇T is the temperature gradient. For 3D anisotropic materials, the thermal conductivity κ is usually a tensor and can be written as

$$\kappa = \begin{pmatrix} \kappa_{11} & \kappa_{12} & \kappa_{13} \\ \kappa_{21} & \kappa_{22} & \kappa_{23} \\ \kappa_{31} & \kappa_{32} & \kappa_{33} \end{pmatrix} \tag{2.29}$$

where the subscripts 1, 2, and 3 refer to a-, b-, and c-axis of the crystal, respectively. The thermal conductivity tensor can be further simplified with certain crystal symmetry. For example, if the crystal holds a four-fold symmetry inside the ab-plane, the thermal conductivity tensor can be simplified as [181]

$$\kappa = \begin{pmatrix} \kappa_{11} & 0 & \kappa_{13} \\ 0 & \kappa_{22} & \kappa_{23} \\ \kappa_{31} & \kappa_{32} & \kappa_{33} \end{pmatrix} \tag{2.30}$$

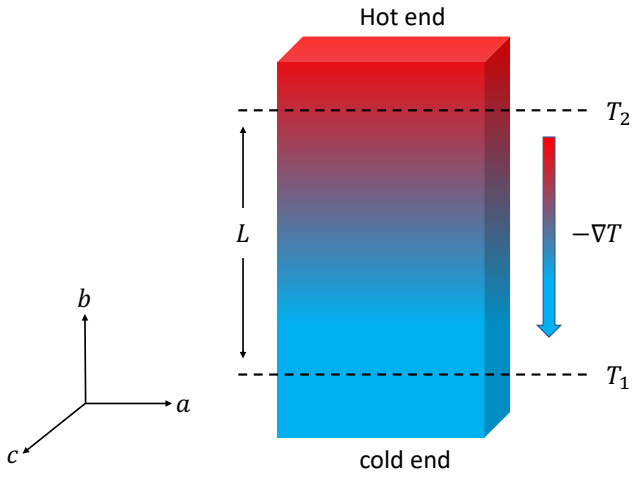

Figure 2.18: Schematic of thermal gradient built along the crystal b axis. Red color denotes the hot end while blue denotes the cold end. T_2 (T_1) is the temperature close to the hot (cold) end. L is the distance between the location where T_1 and T_2 are measured.

In a real experiment, in order to simplify the measurement, we usually make the heat to conduct only along a certain crystal axis. As shown in Figure 2.18, the heat is transferred along the crystal b axis inside the ab plane. The thermal conductivity we measured will be κ_{22}. The temperature gradient can be calculated by $\nabla T = \frac{T_2 - T_1}{L}$. The heat flux q, which gives the heat rate per unit area, can be written as $q = \frac{P}{S}$, where P is the heat that has been

transferred per unit time and S is the sample cross section. With this configuration, κ_{22} can be calculated as

$$\kappa_{22} = \frac{-PL}{S(T_2 - T_1)} \tag{2.31}$$

In SI unit, thermal conductivity is measured in W/(m·K). With a good vacuum and thermal shielding, the heat loss from the sample can be neglected. The heat rate P is equal to the power of the heater which seats at the hot end of the sample. The temperature difference between T_1 and T_2 can be measured by thermocouples or thermometers. Detailed experimental setup and data acquisition method will be introduced in Chapter 3.

2.3.2 Thermopower Measurement

The thermoelectric effect is the direct conversion of temperature differences to electric voltage and vice versa. When a thermal gradient buildup can introduce an electric potential, it is called the Seebeck effect. When an electric current is passed through a circuit of a thermocouple, heat is evolved at one junction and absorbed at the other junction. This is known as the Peltier Effect. Materials that hold significant thermoelectric effects are called thermoelectric materials, which can be used to generate electricity, measure temperature or change the temperature of objects. The Seebeck coefficient (also known as thermopower, thermoelectric power, and thermoelectric sensitivity) of a material is a measure of the magnitude of an induced thermoelectric voltage in response to a temperature difference across that material, as induced by the Seebeck effect. In SI unit, the Seebeck coefficient is measured in V/K.

Most generally, the Seebeck coefficient can be defined through a vector differential equation. In a real experiment, in order to simplify the measurement, we still make the heat to conduct only along a certain crystal axis. As shown in Figure 2.19, when a thermal gradient ∇T is generated along the b axis of the sample, the charged particles will move from the hot end to the cold end which induces an electrical current **J** and an electrical potential ∇V along the crystal b axis. The electrical current **J** can be expressed as

$$\mathbf{J} = -\sigma \nabla V - \sigma S \nabla T \tag{2.32}$$

where **J** is the current density, σ is the electrical conductivity, ∇V is the voltage gradient and S is the Seebeck coefficient. At a steady state, the current density would be zero, which means S can be written as

$$S = \frac{\nabla V}{\nabla T} = \frac{V}{(T_2 - T_1)} \cdot \frac{L_T}{L_V} \tag{2.33}$$

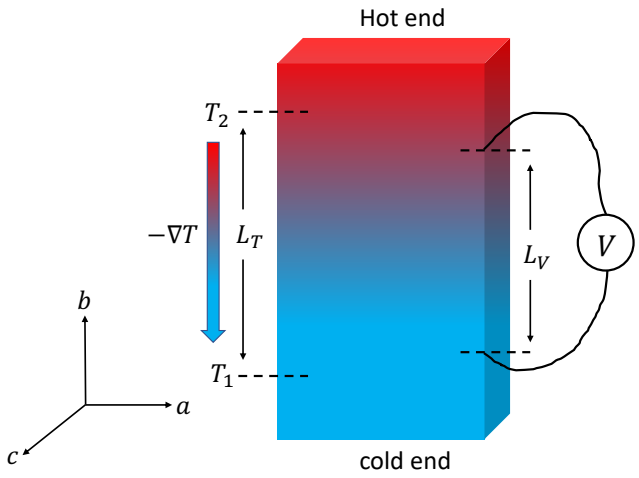

Figure 2.19: Schematic of thermopower measurement. A thermal gradient ∇T induces a voltage difference ∇V across the sample. Red color denotes the hot end while blue denotes the cold end. T_2 (T_1) is the temperature close to the hot (cold) end. L_T is the distance between the location where T_1 and T_2 are measured. L_V is the distance between the location where V is measured.

in which L_T is the distance between the location where T_1 and T_2 are measured. L_V is the distance between the location where V is measured. Detailed experimental setup and data acquisition methods will also be introduced in Chapter 3.

2.3.3 Nernst Effect Measurement

The Nernst effect (also called the Nernst– Ettingshausen effect) is the transverse electric field produced by a longitudinal thermal gradient in the presence of a magnetic field. The thermoelectric effect has been widely studied due to its potential technological application. However, the Nernst effect is much less explored than its longitudinal counterpart. The Nernst effect has been studied in normal metals, magnetic materials, strongly correlated electron systems and type-II superconductors [182, 183]. Nernst effect is very small in normal metals due to the Sondheimer cancellation [184]. After the discovery of a sizable Nernst effect in a high-temperature superconductor, the Nernst effect attracts more attention at the beginning of this century [185]. Since then, there has been a lot of debate about the origin of the Nernst signal in the cuprates [186, 187].

In this section, we will explain the Nernst effect of a normal metal in an electrical transport format. As shown in Figure 2.20, with a thermal gradient $-\nabla T$ generated along

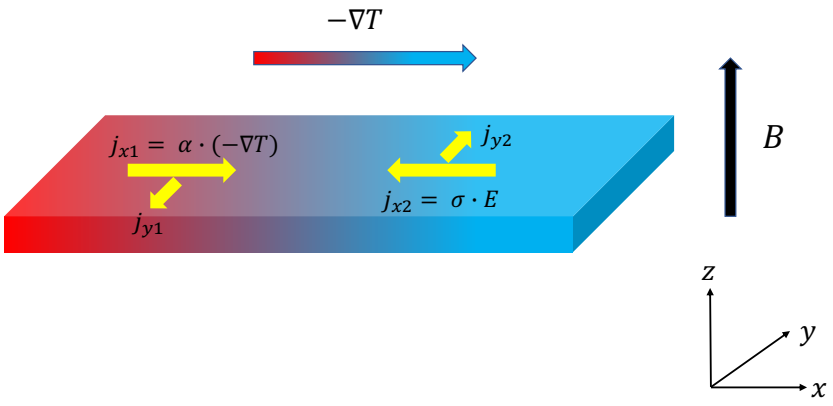

Figure 2.20: Schematic of Nernst effect in a normal metal. The longitudinal electrical current j_x is induced by a thermal gradient $-\nabla T$. The transverse current j_y is produced when a magnetic field B is applied along the z direction. The unbalance between the transverse current j_{x1} and j_{x2} produces the Nernst signal.

the x direction and a magnetic field applied along the z direction, the total electrical current density in the metal is

$$\mathbf{j} = \sigma \cdot \mathbf{E} + \alpha \cdot (-\nabla \mathbf{T}) \tag{2.34}$$

where σ is the 2D electrical conductivity tensor and α is the 2D Peltier conductivity tensor. So in a matrix form,

$$\begin{pmatrix} j_x \\ j_y \end{pmatrix} = \begin{pmatrix} \sigma_{xx} & \sigma_{xy} \\ \sigma_{yx} & \sigma_{yy} \end{pmatrix} \begin{pmatrix} E_x \\ E_y \end{pmatrix} + \begin{pmatrix} \alpha_{xx} & \alpha_{xy} \\ \alpha_{yx} & \alpha_{yy} \end{pmatrix} \begin{pmatrix} -\nabla_x T \\ -\nabla_y T \end{pmatrix} \tag{2.35}$$

Now we can write down the in-plane current density in a two-component form.

$$j_x = \sigma_{xx} E_x + \sigma_{xy} E_y + \alpha_{xx}(-\nabla_x T) + \alpha_{xy}(-\nabla_y T) \tag{2.36}$$

$$j_y = \sigma_{yx} E_x + \sigma_{yy} E_y + \alpha_{yx}(-\nabla_x T) + \alpha_{yy}(-\nabla_y T) \tag{2.37}$$

Since the temperature gradient along the y direction can be negligible, we can ignore the terms with $-\nabla_y T$. If we use the symmetry condition $\sigma_{xy} = \sigma_{yx}$, $\alpha_{xy} = \alpha_{yx}$, $\sigma_{xx} = \sigma_{yy} = \sigma$ and $\alpha_{xx} = \alpha_{yy} = \alpha$, equation 2.36 and 2.37 can be simplified to

$$j_x = \sigma E_x + \sigma_{xy} E_y + \alpha(-\nabla_x T) \tag{2.38}$$

$$j_y = \sigma_{xy} E_x + \sigma E_y + \alpha_{xy}(-\nabla_x T) \tag{2.39}$$

At the steady state, the net current flow should be zero, which means $j_x = 0$ and $j_y = 0$. We can solve 2.38 and 2.39 together to get [186, 188]

$$e_y = \frac{E_y}{\nabla_x T} = \frac{\sigma\alpha_{xy} - \sigma_{xy}\alpha}{\sigma^2 - \sigma_{xy}^2} \tag{2.40}$$

in which e_y is observed Nernst signal. The Nernst coefficient is defined as $\nu = \frac{e_y}{B}$, where B is the magnetic field. For most of the samples discussed, the Hall angle θ is small, which means $\tan\theta = \frac{\sigma_{xy}}{\sigma} \ll 1$. So we have

$$e_y \sim \frac{\alpha_{xy}}{\sigma} - \frac{\alpha \tan\theta}{\sigma} \tag{2.41}$$

Using the definition of the thermopower $S = \frac{E_x}{\nabla_x T}$, we cam solve 2.38 and 2.39 together to get

$$\frac{E_x}{\nabla_x T} = \frac{\sigma\alpha - \sigma_{xy}\alpha_{xy}}{\sigma^2 - \sigma_{xy}^2} = \frac{\alpha}{\sigma} - \frac{\alpha_{xy}\tan\theta}{\sigma} \tag{2.42}$$

With the small Hall angle assumption,

$$S = \frac{E_x}{\nabla_x T} \approx \frac{\alpha}{\sigma} \tag{2.43}$$

Equation 2.41 can be expressed as

$$e_y = \frac{\alpha}{\sigma}(\frac{\alpha_{xy}}{\alpha} - \tan\theta) = S(\frac{\alpha_{xy}}{\alpha} - \tan\theta) = S(\tan\theta^P - \tan\theta) \tag{2.44}$$

where θ is the electrical Hall angle. θ^P is the Peltier Hall angle with $\tan\theta^P = \frac{\alpha_{xy}}{\alpha}$. Under the small Peltier Hall angle approximation, $\tan\theta^P \approx \theta^P = \frac{\alpha_{xy}}{\alpha}$. We the small Hall angle approximation, we have

$$e_y = S\frac{\alpha_{xy}}{\alpha} - S\tan\theta = \rho\alpha_{xy} - S\tan\theta \tag{2.45}$$

From 2.40, the Nernst signal is $e_y = \frac{E_y}{\nabla_x T}$. In the real experiment, E_y can be calculated by measuring the Voltage drop V along the x direction and divided by the distance between two voltage leads along x. The thermal gradient $\nabla_x T$ can be measured in the same way as in the thermal conductivity measurement. Detailed experimental setup and data acquisition methods will also be introduced in Chapter 5.

2.3.4 DC Power Tests for Thermal Conductivity and Thermoelectric Measurements

When conducting thermal transport or thermoelectric measurements, selecting the correct heater power range is crucial. If the heater power is too small, it won't build enough thermal gradient across the sample which can not generate large enough signals for detection. If the heater power is too large, it will heat the whole sample which is extremely unfavorable if the measurement is done at low temperatures. One way to make sure that the heater power is within the reasonable range is to conduct a DC power test at both room temperature and the lowest experiment temperature before starting the measurement. We can apply a series of DC currents to the sample heater and monitor the thermal couple reading at the same time. If the temperature difference between the two thermocouple junctions on the sample linearly depends on the square of the heater current, it means the temperature difference is proportional to the heater power.

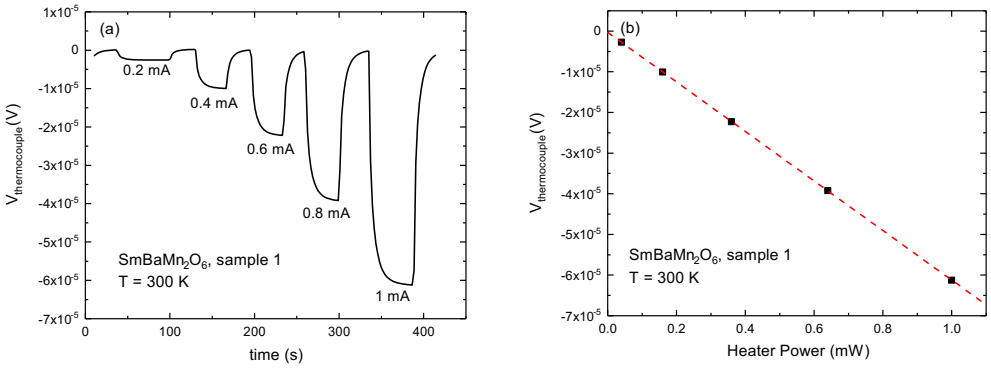

Figure 2.21: Linear response test of the thermocouple with various heating powers in $SmBaMn_2O_6$ Sample 1 at room temperature. (a) The thermocouple voltage is plotted as the DC heating power is set from 0 to several other constant values. (b) The average stable thermocouple voltage is plotted against the DC static heater power. The result shows that the thermocouple reading responses linearly to the heater power. The heater resistance is 1 kΩ.

For the thermal transport measurement, we take the DC power test in $SmBaMn_2O_6$ Sample 1 at 300 K as an example. Figure 2.21 plots the linear response of the thermocouple when applying various heating powers across $SmBaMn_2O_6$ Sample 1. The DC heater power can be applied as an on-off series. Using the type-E thermocouple calibration relation, at 300 K, $\frac{dV}{dT} = 61.1\mu V/K$. We can get the temperature difference between the two thermocouples is around 1 K when applying a 1 mW heater power.

For the thermoelectric measurement, we take the DC power test in $Fe_{1+y}Te_{1-x}Se_x$

Sample 1 at 300 K as an example. Figure 2.22 plots the linear response of the thermocouple and Seebeck voltage when applying various heating powers across $Fe_{1+y}Te_{1-x}Se_x$ Sample 1. To verify that our sample has an even temperature gradient and linear response to the heater power, we change the heater power at room temperature and measure the temperature difference across the two thermocouples. The data are plotted in Figure 2.22 (a), in which we choose 3 different heater current 0.2 mA, 0.4 mA and 0.6 mA. Figure 2.22 (b) shows the temperature difference between the two thermocouples linearly depends on the heater power. Figure 2.22 (c) shows the voltage between two Seebeck contacts linearly depends on the heater power. Therefore, the temperature gradient and thermal power response are proportional to the heater power.

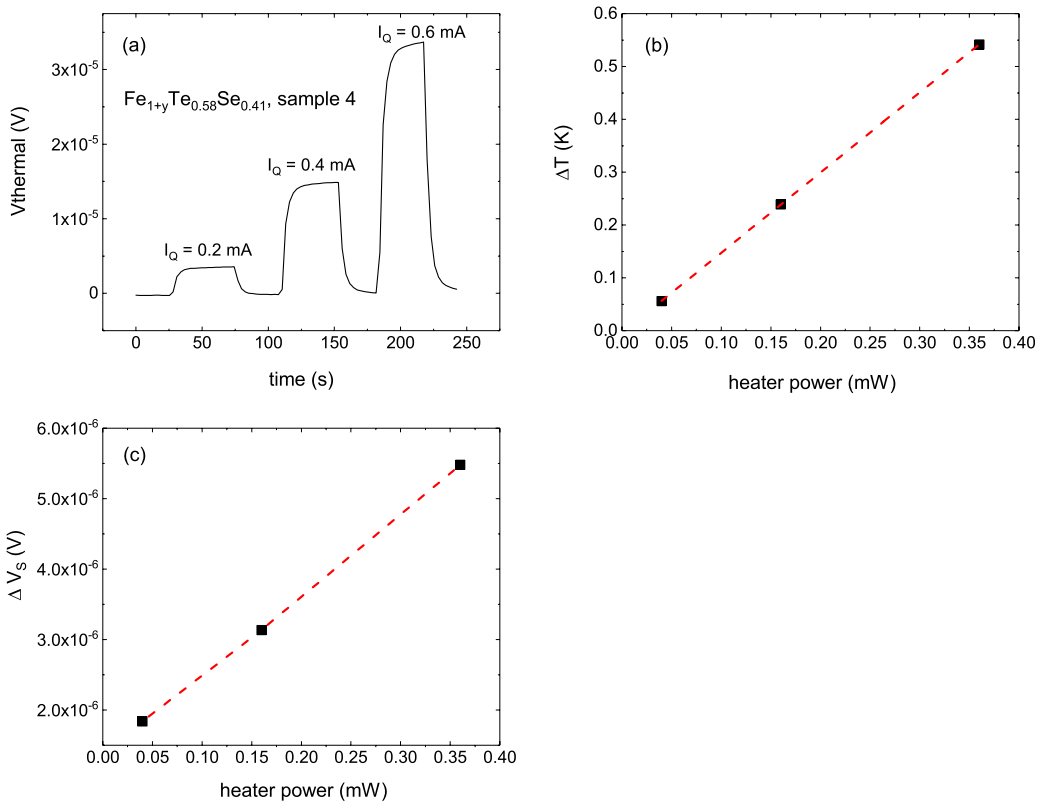

Figure 2.22: Linear response test of the thermocouple and Seebeck voltage with various heating powers in $Fe_{1+y}Te_{1-x}Se_x$ Sample 1 at 300 K. (a) Voltage difference across the thermocouple with different heater current at 300 K. (b) The converted temperature difference between two thermocouples vs. the heater power at 300 K. (b) The voltage between two Seebeck contacts vs. the heater power at 300 K. The heater resistance is 1 kΩ.

2.3.5 Equipment

2.3.5.1 High-temperature Vacuum Probe

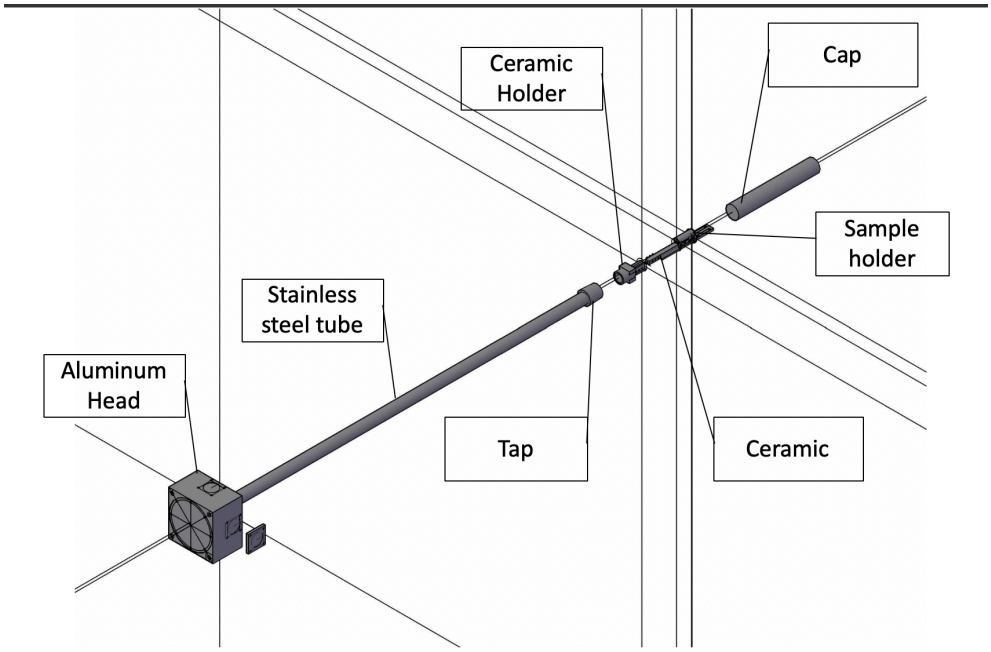

Figure 2.23: Schematic of the home-made high-temperature probe.

In order to conduct electrical and thermal measurements above room temperature, we design and build a high-temperature vacuum probe. The high-temperature vacuum probe was first designed and made by visiting student Peng Cai from Tsing Hua University. The sample holder and feed through were later modified by postdoc Gang Li and me. Figure 2.23 shows the schematic of the high-temperature probe. This probe has four coax wires and 9 pairs of twisted pairs, which could be used to run thermal transport measurements as well as tuning fork measurements. Figure 2.24 shows the front and back view of the probe head. The vacuum is held by a taper seal. A small amount of vacuum grease can be applied between the brass cap and tap to help seal the vacuum. The ceramic or nylon insulators are used as thermal insulation between the sample holder and stainless steel tube. The probe temperature can go to $150°$C with the nylon insulator, while it can go even higher with the ceramic insulator. But one thing that needs to be kept in mind is the maximum temperature the probe can reach also depends on the melting point of the insulating layers of the wires inside the cap. So an extra care is needed when running this probe at a T $> 200°$C. The 18 pin sample holder and the heater cavity are machined by one piece of oxygen-free copper.

A 50 Ω resistive heater is put inside of the heater cavity and mounted together by torr seal. This heater could be used to control the probe temperature. A type E thermocouple is screwed on the far end of the sample holder, which could be used to measure the probe temperature. From the back view (Figure 2.24 (b)), we can see a plastic terminator block is mounted on top of the ceramic or nylon insulator. The twisted pairs coming from the top of the probe are first clamped (or terminated) by each screw on the terminator. Then one end of the extension of the twisted pairs are clamped on the screws. The other end of the extensions are soldered to the dip-sip sockets, which finally insert into the holes on the sample holder. The advantage of the terminator block is it can separate the twisted pairs into two parts. In the real experiment, the extensions are more likely to be damaged. With this setup, we only need to replace the extension instead of replacing the whole wire inside the probe.

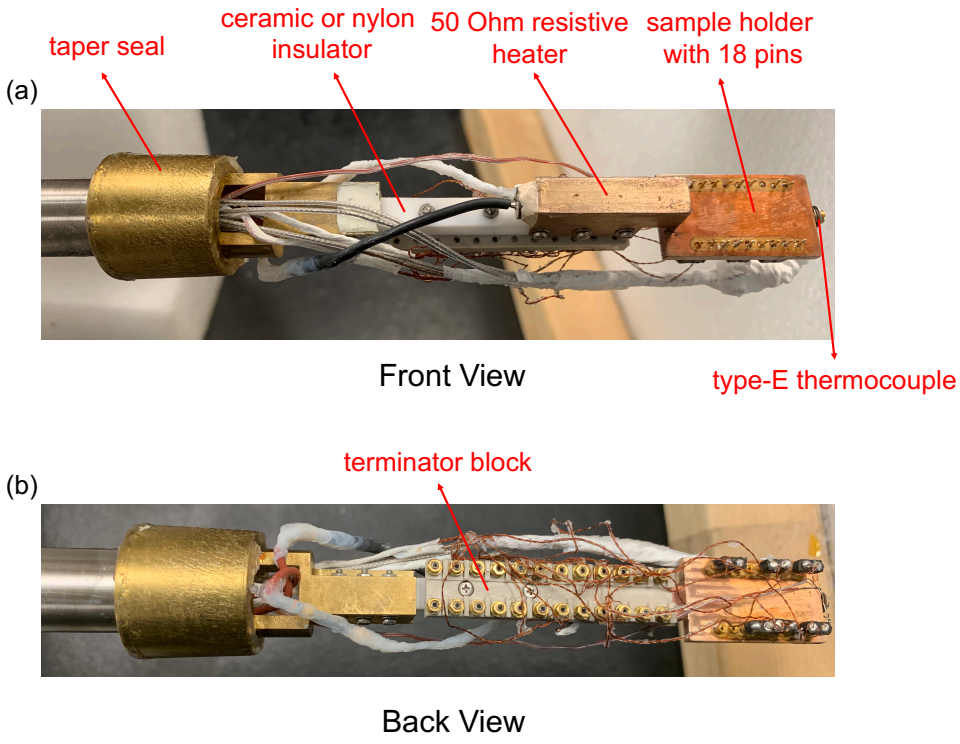

Figure 2.24: (a) Front and (b) back view of the high-temperature probe head.

Figure 2.25 (a) shows the probe head. On the top, four coax wires are soldered to the four SMA connectors. A Detoronics DJ (MIL-DTL-38999 series II type) vacuum-sealed circular connector is mounted on one side of the probe head, which is used to connect all the twisted pairs. A feedtrough made by torr seal is located on the other side, which has one pair of type-E thermocouple wires and four pure copper rods that coming out (as shown in

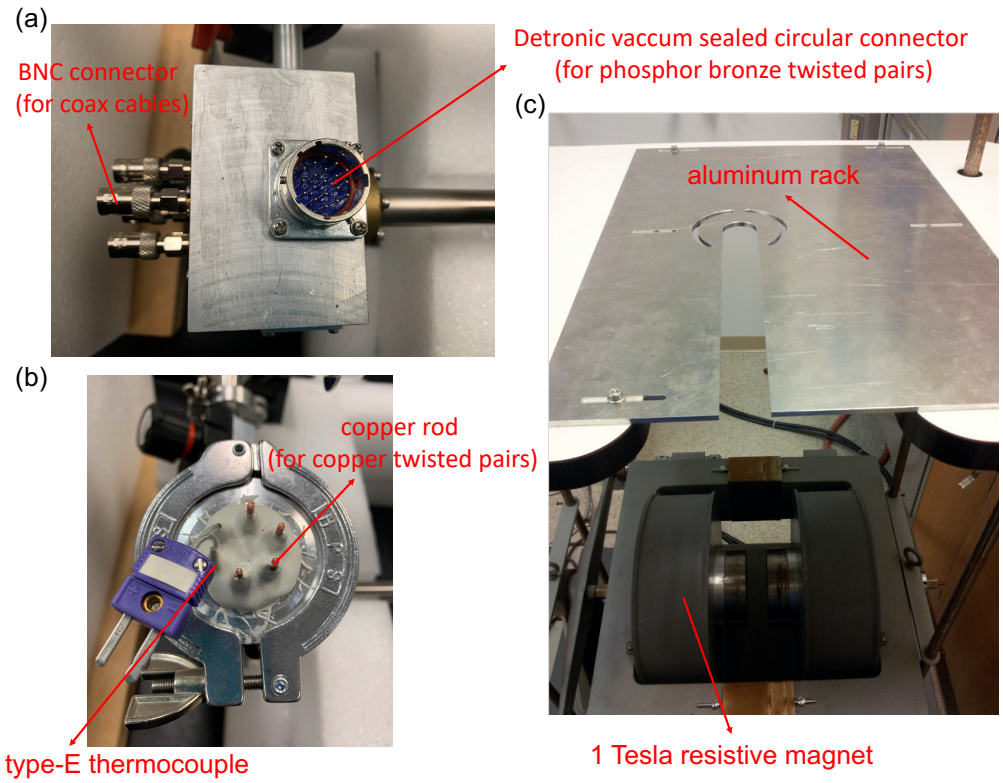

Figure 2.25: (a) Four BNC connectors and one Detronic vacuum-sealed circular connector located on the head of the probe. (b) Feed trough made by torr seal located on the head of the probe. There are one pair of type-E thermocouple wires and four pure copper rods coming out of the feed through. (c) 1 T resistive magnet with an aluminum rack on top. The vacuum probe can be mounted on the aluminum rack which makes the sample holder seat in the center of the magnetic field.

Figure 2.25 (b)). Two of the pure copper rods are connected to the 50 Ω resistive heater. The other two copper rods are connected to pure copper twisted pairs. The last side of the probe head is left with a KF 16 flange, which is used to connect to the pumping station and pump the probe down to vacuum. The probe can reach a vacuum level of 1×10^{-4} mbar with a well-sealed cap. Figure 2.25 (c) shows our 1T resistive magnet. The high-temperature probe can be mounted on top of the aluminum rack which makes the sample holder locates right at the center of the magnetic field.

2.3.5.2 Home-build Thermal Transport Puck For PPMS

The thermal transport option that was designed by Quantum Design can only be used to measure a big bar-shaped sample which has a length of 5 to 10 mm. It also requires that the sample can not be too fragile since thick copper wires have to be wrapped around the

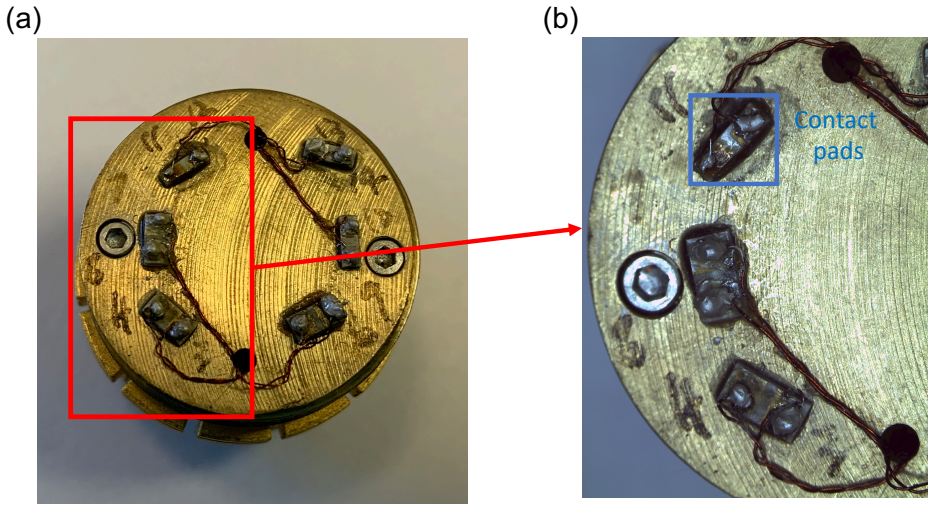

Figure 2.26: Home-build Thermal Transport Puck For PPMS. Panel (b) is a zoom-in of Panel (a) in which the blue square surrounds the contact pads made by BeO heat sink chips.

sample, which causes a huge tension on the sample. In order to measure smaller and more fragile samples, we develop a home-build thermal transport puck for our PPMS system.

Our thermal transport puck contains three parts, a universal puck from Quantum Design, a heat sink and a cap machined with brass by the machine shop (as shown in Figure 2.26). The heat sink is mounted on top of the universal puck by two screws. 6 BeO heat sink chips are glued on top of the heat sink with H74f thermal epoxy from Epo-tek. This puck has 6 twisted pairs in total, which contains 12 wires made by phosphor bronze. One end of the twisted pairs is soldered in the hole of the universal puck, while the other end is soldered on top of the BeO heat sink chip (purchased from Lake Shore Cryotronics). Samples can be mounted on top of the heat sink. The cap is used as shielding for the thermal radiation. The advantage of our home-build thermal transport puck is it can be used to measure small sample which has a length of 1 to 2 mm. Since our home-build thermal transport puck can be integrated into the PPMS system, it can measure a temperature range of 2 to 400 K under a magnetic field of 0 to 14 T.

CHAPTER 3

Study of Thermal Conductivity in Phase-change Materials

In this chapter, we will discuss the thermal transport study conducted in two strongly correlated materials, VO_2 and $SmBaMn_2O_6$. We investigate the thermal conductivity across the phases transitions in VO_2 and $SmBaMn_2O_6$ single crystals and get one-order-of-magnitude enhancement in the thermal conductivity within the metal-insulator transition. These experiments shed light on the role played by phonon across the first-order structural transition. These experiments could also bring potential applications in electronic devices and solve the thermal management issues in solid-state materials. The related publications can be found in Ref. [189, 190].

3.1 Enhancement of Thermal Conductivity Across the Metal-insulator Transition in Vanadium Dioxide

Metal-to-insulator transition (MIT) in vanadium dioxide (VO_2) was investigated by electrical and thermal transport measurements. We report an order-of-magnitude enhancement of thermal conductivity across the MIT region in the VO_2 single crystal. Magnetic field dependent measurements reveal the thermal conductivity peak doesn't show an obvious dependence on the magnetic field, which indicates that the enhancement of thermal conductivity could come from neutral heat carriers such as phonons. Our experiment provides a direction of achieving thermal management in phase-change materials.

3.1.1 Metal Insulator Transition in Vanadium Dioxide

As a strongly correlated system, VO_2 undergoes a first order metal-to-insulator phase transition at around $T_s = 340$ K due to a crystal structure and electronic structure change

[34]. The low-temperature insulating phase has a monoclinic structure (M, $P2_1/c$) with a band gap $E_g \approx 0.6$ eV, while the high-temperature metallic phase is characterized by a rutile crystalline structure (R, $P4_2/mnm$) [35]. The MIT is accompanied by a significant change in the electrical conductivity and the thermopower [34, 191]. The transition temperature can be tuned over a wide range by aliovalent ion doping [192], external strain [193], and external electrical field [194]. As a typical example of phase-change material, VO_2 provides a potential platform for achieving electronic and optical devices [195, 196].

The nature of the MIT is still unclear due to the complex interplay among several degrees of freedom (charge, lattice, orbital and spin). At a temperature around the MIT, the metallic tetragonal and insulating rutile phases coexist in this material and induce complicated domain structures, which significantly affect the transition characteristics, such as the broadening of the MIT [197]. A photoinduced metal-like phase of monoclinic VO_2 was reported by combining ultrafast electron diffraction and infrared transmissivity experiments, which indicates that there exists a metastable state within the transition that retains the lattice distortion of the insulating phase but acquired metal-like mid-infrared optical properties [198]. Recently, a thermal conductivity measurement has revealed a violation of the Wiedemann-Franz law by observing an order-of-magnitude decrease of the Lorentz number at the high-temperature metallic phase in the vicinity of the MIT [191]. This unusually low electronic thermal conductivity and the breakdown of the Wiedemann-Franz law indicates that the charge and heat carriers diffuse differently in this strongly correlated electron fluid.

In order to further understand the nature of the MIT, we conduct the electrical and thermal transport measurements in VO_2 single crystals. A significant decrease of the Seebeck coefficient accompanied by a $10^4 \sim 10^5$ orders of magnitude increase of the electrical conductivity was observed across the transition. However, the thermal conductivity is enhanced by 1 order of magnitude at the transition temperature T_s. This thermal conductivity peak doesn't show apparent dependence on the magnetic field up to 13.9 T, which indicates that the heat carriers are neutral and don't interact with the external magnetic field. The strong enhancement of thermal conductivity likely results from the softening of certain phonon modes at the phase transition [199, 200].

3.1.2 Thermal Conductivity Measurement Setup for VO_2

The single crystal VO_2 samples being used in our experiments are grown by the chemical vapor transport method [201, 202]. Typical single crystals are needle-like with the crystal c axis along the axial direction, which have lengths between 1 to 2 mm (shown in Figure

3.1 (a)). The electrical and thermal transport measurements are conducted in our home-developed high-temperature vacuum probe (more details about the probe design is in the Appendix). The temperature of the probe is controlled by a Lakeshore model 336 cryogenic temperature controller. The magnetic field dependent thermal measurement is conducted in a Physical Properties Measurement System (PPMS) DynaCool from Quantum Design. To conduct thermal measurements in the PPMS system, we design and build a thermal transport puck that's compatible with the PPMS system (more details about the thermal transport puck is in the Appendix).

Figure 3.1 (b) shows the schematic of our experimental setup. A needle-shaped VO_2 single crystal is mounted vertically on a sapphire substrate. A resistive heater is mounted on top of the sample, which can provide a thermal gradient along the c axis of the sample. Four electrical contacts are placed consecutively on the front side of the sample with H20E silver epoxy from Epo-tek, which can be used to conduct the four-lead resistance measurement as well as the thermal power measurement. Two type E thermocouples are mounted on the back side of the sample to measure the temperature gradient across the sample. In order to prevent the thermocouple from electrically shorted to the sample, the thermocouple junction is thermally linked to the sample by a small amount of thermal joint compound. Two ends of the thermocouples with the same material are shorted together. The voltage across the two un-shorted ends indicates the temperature difference between these two thermocouple junctions. The whole setup is glued on the heat sink of the high-temperature probe by H grease.

The four-lead resistance is measured by applying a low-frequency AC current through the sample with a Keithley 6221 DC and AC current source. The voltage across the sample is measured by a Stanford Research 830 DSP lock-in amplifier. The thermal power and thermal conductivity are measured by a pulsed power technique [203]. A periodic AC current (f = 0.01 Hz) is applied to the heater which seated on top of the sample by the current source. A small temperature gradient is generated between the heater and the heat sink. The temperature of the sample is adjusted by a global heater on the probe, which varies with a speed of 0.1 K/min in the experiment. The thermal power is measured through two of the electrical contacts by a Keithley 2182A nanovoltmeter. The voltage across the two thermocouples is measured by another Keithley 2182A nanovoltmeter. Before the thermal conductivity measurement, we have to conduct a DC power test first to make sure the temperature gradient responses linearly to the heater power (more details can be found in the Appendix). In our measurement, we carried out a dense temperature-dependent measurement only across the MIT region to reduce the material cracking due to the thermal cycles.

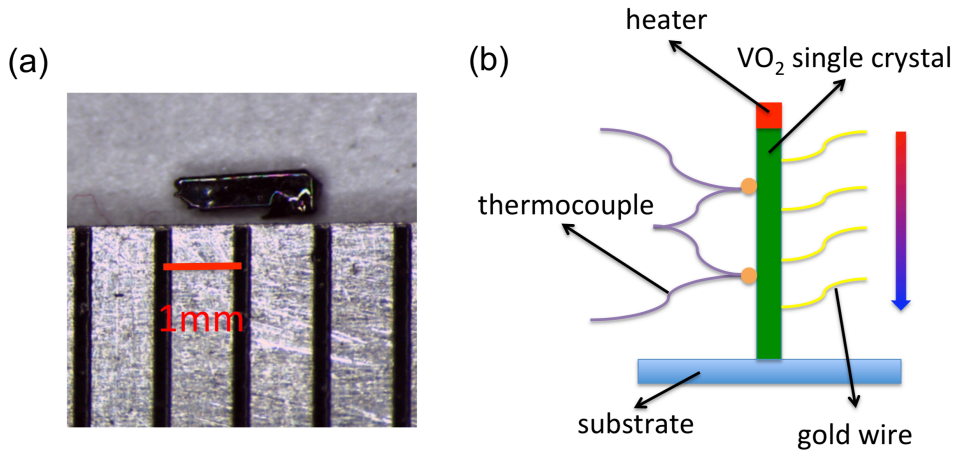

Figure 3.1: (a) Typical VO_2 single crystals besides a mm scale. (b) Schematics of the experimental setup. A bar-shape VO_2 single crystal stands vertically on a sapphire substrate with a resistive heater mounted on top of the sample. Four gold wires are used to conduct the four-lead resistance measurement as well as the thermopower measurement. Two shorted thermocouples are used to measure the temperature gradient along the sample. The arrow on the right-hand side indicates the direction of the heat flow.

3.1.3 Enhancement of Thermal Conductivity Across the Metal Insulator Transition in VO_2

Figure 3.2 (a) shows the temperature dependent electrical conductivity measured from 300 K to 370K. The sample undergoes a metal to insulator transition around 340 K with the conductivity increases about a factor of $10^4 \sim 10^5$ and a thermal hysteresis loop appears at T_s between warming up and cooling down, similar to previous results in VO_2 single crystals and thin films [34, 204, 205]. The difference between the transition temperature during warm up and cool down is around 4 K. The Seebeck coefficient is large and electron-like (shown as the negative sign) in the low temperature insulating state. The magnitude of S vs. temperature T is shown in Figure 3.2 (b). The Seebeck coefficient S starts to decrease from $850\mu V/K$ for the insulating state to $26\mu V/K$ for the metallic state at around $T_s = 338$ K. The constant value of S in the metallic state is consistent with the previous experimental results in bulk VO_2 single crystals [34], microbeams [206] and thin films

[207, 208].

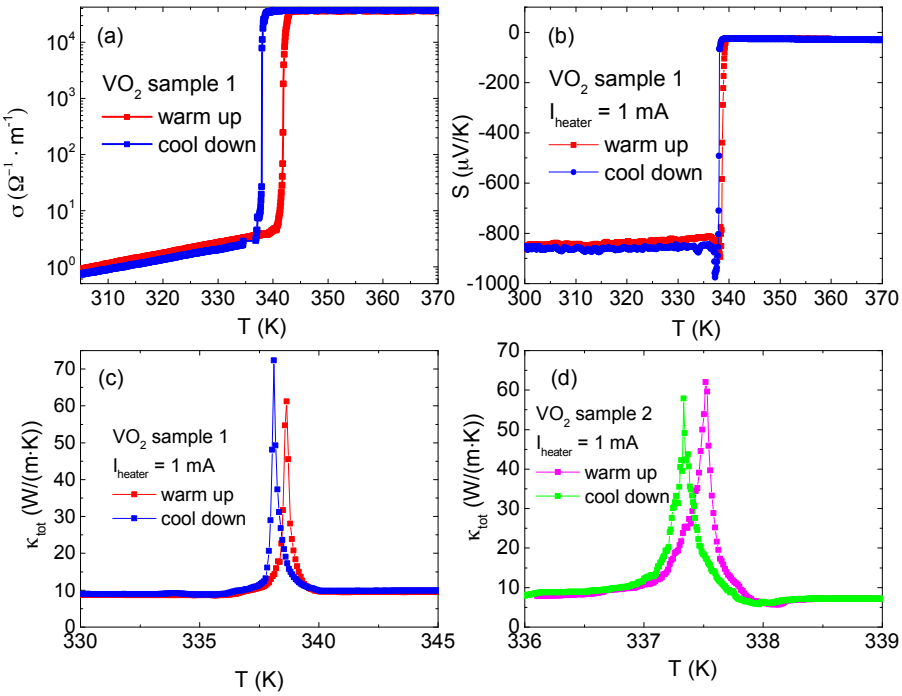

Figure 3.2: (a) Four-probe electrical conductivity σ vs. T in VO_2 Sample 1. (b) Seebeck coefficient S vs. T for VO_2 Sample 1. The sample temperature was swept at a rate of 0.1 K/min. The difference of the transition temperature T_s between (a) and (b) results from the heating across the sample in the Seebeck measurement. (c) Measured total thermal conductivity κ_{tot} vs T for VO_2 Sample 1 at the same T sweeping rate as Panel (b). The thermal conductivity peaks with an about $8 \sim 9$ times increase across the metal-insulator transition. (d) Measured total thermal conductivity κ_{tot} vs. T for VO_2 Sample 2 with a slower sweeping speed of temperature ($\sim$ 0.01 K/min). The enhancement of thermal conductivity signal is reproduced in Sample 2. In (a) $\sim$ (d), red (magenta) curves denote warming up while blue (green) curves denote cooling down.

In bulk VO_2, it was reported that the total thermal conductivity κ_{tot} almost stays constant [34, 191] or decreases [209] very slightly with temperature increases across the MIT. The temperature dependent thermal conductivity measured in VO_2 Sample 1 is shown in Figure 3.2 (c). The thermal conductivity in the semiconductor states and the metallic states only differs by $\sim$ 0.9 W/(m$\cdot$ K), which is about 4.5 times larger than the previously measured value in the VO_2 nanobeam ($\sim$ 0.2 W/(m$\cdot$ K))[191]. This difference is mainly because Ref. [191] used single-crystal VO_2 nanobeams while we used VO_2 bulk single crystal. A larger thermal conductivity suggests a longer mean free path and less disorder in our bulk single crystal samples. We focus on the thermal conductivity in detail across the MIT and found that the thermal conductivity peaks with an increase of about $8 \sim 9$ times within the MIT. This anomalous peak in thermal conductivity only exists within a very narrow

temperature range inside the transition region ($\sim$ 2 K with I_{heater} = 1.41 mA), it requires a very slow sweeping rate of global T to reveal such a narrow peak. Figure 3.2 (c) is taken with a temperature sweeping speed of 0.1 K/min. This anomalous peak is repeated in VO_2 Sample 2 with a slower sweeping speed ($\sim$ 0.01 K/min) (shown in Figure 3.2 (d)). This sharp peak was likely missed in Ref. [191] because they only used a steady-state method which did not track dense enough data points within the MIT.

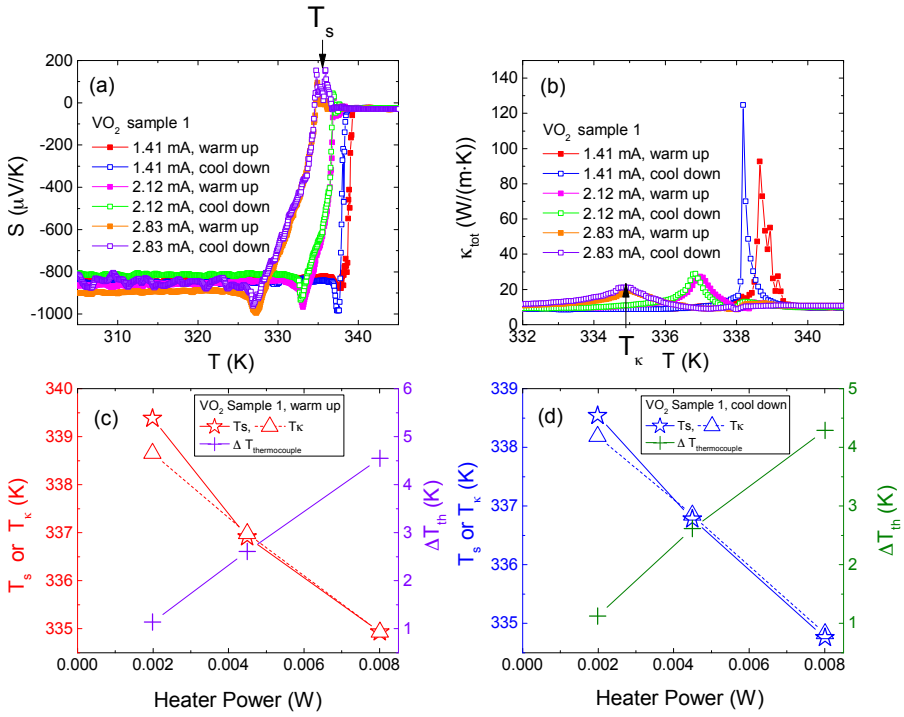

Figure 3.3: (a) Temperature-dependent Seebeck coefficient S measured in VO_2 Sample 1 with different heater current. The AC current going through the heater I_{heater} ranges from 1.41 mA to 2.83 mA (peak value). The transition temperature T_s for thermal power is defined as the temperature when the entire of the sample enters the metallic state. T_s shifts towards lower temperature with higher heater power. (b) Total thermal conductivity κ_{tot} vs. T in VO_2 Sample 1 with different heater current. The peak position of thermal conductivity T_κ also decreases with the heater power. (c) Left axis: T_s and T_κ vs. heater power during warm up. Right axis: the temperature difference between the two thermocouples ΔT_{th} vs. heater power during warm up. (d) Left axis: T_s and T_κ vs. heater power during cool down. Right axis: the temperature difference between the two thermocouples ΔT_{th} vs. heater power during cool down. Solid and dashed lines are guides to the eyes.

To study the self-heating effect from the sample heater, we measured the thermal power and thermal conductivity with different heater current (as shown in Figure 3.3). The transition temperature T_s for thermal power is defined as the temperature when the entire of the sample enters the metallic states. Figure 3.3 (a) shows T_s shifts towards lower temper-

ature with higher heater power. A similar effect is also observed in thermal conductivity. The thermal conductivity peak position T_κ moves towards lower temperature and broadens with higher heater power. Because of the sample heater, the real temperature of the sample could be higher than the temperature reading from the thermometer on the probe. So we plot the temperature difference between the two thermocouples ΔT_{th} vs. the heater power on the right axes of Figure 3.3 (c) (warm-up) and (d) (cool-down). During warm-up, when the heater power increases from 2 mW to 8 mW, ΔT_{th} increases by 3.5 K. The transition temperature T_s and T_κ are plotted on the left axes of Figure 3.3 (c) (warm-up) and (d) (cool-down). T_s decreases about 4.5 K and T_κ decreases by 3.7 K when the heater power changes from 2 mW to 8 mW. So the shift of T_s and T_κ is mainly due to the self-heating coming from the sample heater. The reason why the thermal conductivity peaks become broader with higher heater power is that the enhancement of thermal conductivity only happens in a very narrow temperature range, the AC current in the sample heater changes the sample temperature during one period, which artificially broadens the peak. This heating effect also explains the difference of T_s values observed in the electrical resistivity and that of the Seebeck effect shown in Fig. 2.4(a) and Fig. 2.4(b).

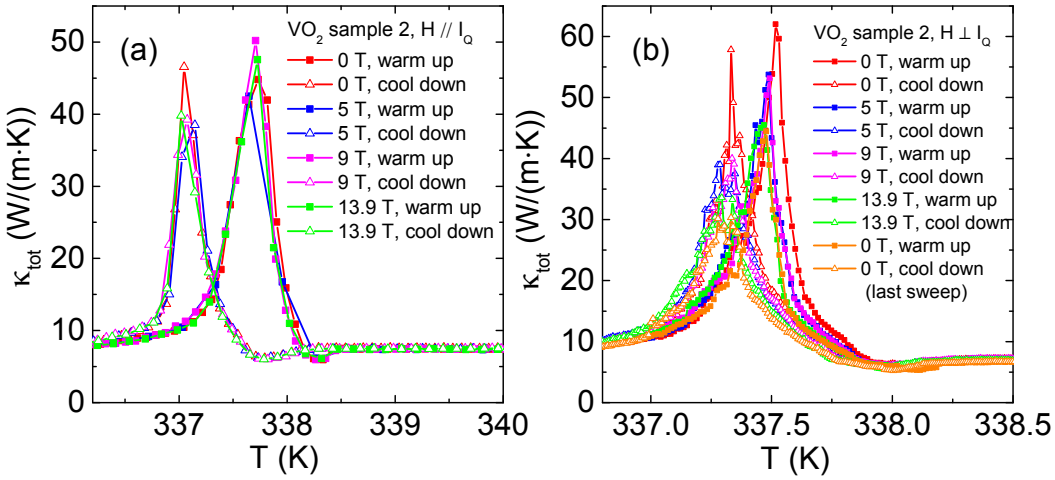

Figure 3.4: Magnetic field dependence of the total thermal conductivity κ_{tot} vs. T in VO_2 Sample 2 with H (a) parallel to the heat flow I_Q and (b) perpendicular to the heat flow I_Q.

To further understand the origin of the thermal conductivity peak, we measured the magnetic field dependence of the thermal conductivity up to 13.9 T with both longitudinal and transverse configuration. When H is parallel to the heat current I_Q, the peak position and width don't show obvious change with respect to the magnetic field (Figure 3.4 (a)). With H perpendicular to I_Q, the thermal conductivity peak becomes slightly lower and shifts towards lower temperature (as shown in Figure 3.4 (b)). In order to verify whether this change is due to magnetic field or sample degradation [210], we did the field depen-

dent measurement with a sequence of magnetic field equal to 0 T, 5 T, 9 T, 13.9 T and 0 T. We found that the peak height always becomes lower and the position keeps on shifting towards lower temperature. Thermal cycles could bring a considerable amount of thermal shock to the sample, which induces dislocation strain fields in it and decreases the thermal conductivity [210]. So the lowering of the thermal conductivity peak in different thermal cycles should come from the sample degradation. The contribution to the thermal conductivity peak could come from neutral heat carriers since it doesn't respond to the magnetic field. One way that could help to reduce the crack from the thermal cycle is only to carry out dense temperature-dependent measurement across the MIT region. For example, we first do a T dependent sweep from 300K to 370K. After that, we only do T sweep between 335K and 340K to further reveal what happens inside the MIT. Avoiding sweep across a broad temperature range (like from 300K to 370K) could help to slow down the cracks in the sample.

3.1.4 Theoretical Explanation: Soft Phonon

One significant feature of the enhancement of the thermal conductivity is that it only happens during the MIT, around where VO_2 undergoes a structural transition from low-temperature rutile phase to high-temperature tetragonal phase. The kinetic model relates the thermal conductivity κ with the heat capacity C as

$$\kappa \sim \frac{1}{3} C v l \tag{3.1}$$

with v the average velocity, and l the mean free path. The sharp peak of κ at the MIT can not be completely explained by the divergence of C at the first-order phase transition because the heat capacity peak in VO_2 is much weaker than our 8-9 times enhancement peak in the thermal conductivity [34, 211]. Similar enhancement of thermal conductivity at high temperature was also observed around the α-β phase transition in Cu_2Se and $Cu_{1.98}Ag_{0.2}Se$ between 350 K and 400 K [212], while the origin of this peak was not quite discussed yet. But a significant reduction of the thermal conductivity is observed in PbTe [213] and $Pb_{1-x}Ge_xTe$ [214] alloys, and this change was argued to arise from the softening of optical mode can increase anharmonic acoustic-optical coupling and decrease phonon lifetimes. On the theory side, Eq. 3.1 assumes a homogeneous and isotropic conduction media. The structural phase transition in VO_2 indicates an inhomogeneous media. The mean free path l is at best the same and could become much smaller during the transition.

The acoustic phonons already carry out heat current in the insulating and metallic states. It is hard to figure out the mechanism that can reduce the scattering rate of acoustic

phonons by a factor of 8∼9 only at the MIT transition. Therefore, we hypothesize that the strong enhancement of κ in VO_2 can be explained by a large group velocity increase at the transition, which is likely a consequence of the softening optical phonon modes that were observed by neutron scattering [200] in VO_2. Generally, when the crystal structure undergoes a transition that is associated with softening of the optical phonons, the population n and velocity v of these phonon modes increase greatly. The phonon thermal conductivity is $\kappa_{ph} \propto \frac{1}{k_B T^2} \sum n(n+1)(\hbar\omega)^2 v l$, with $\hbar\omega$ the phonon energy [215]. As a result, the increase of additional softened phonons, as well as the phonon velocity would likely to contribute to the enhancement of the thermal conductivity. For example, silica involves from the low-pressure stishovite phase to the high-pressure $CaCl_2$-type phase under hydrostatic compression [216, 217, 218]. Recently, Aramberri $et.\ al.$ carried down first-principle calculations and reported that in silica the longitudinal component of thermal conductivity κ increases about 2 orders of magnitude at the critical pressure P_c and T = 10 K [215]. At the structural transition point, because of the instability of the lattice, the softening of some acoustic modes are overcompensated by a large increase of their population, which strongly enhances the low-temperature thermal conductivity of silica. However, for VO_2, the phase transition happens at a much higher temperature, and other factors could dominate the contribution of thermal conductivity. Aramberri $et.\ al.$ [215] also points out that when three-phonon scattering dominates the scattering process, the mode softening can close the phonon-phonon scattering channels and increase the thermal conductivity. The increase of phonon population due to softening could bring a substantial enhancement in the heat capacity. Given such a high increase of heat capacity around MIT and non-zero group velocity, the softened phonons could carry a huge amount of heat which results in the peak in the thermal conductivity. One example is the thermal conductivity peak near the Peierls transition in two charge-density-wave systems $K_{0.3}MoO_3$ and $(TaSe_4)_2I$ [219]. The author claimed that the anomalous peak is due to the increase of phonon mode population rather than changes in electron- or phonon-scattering process. A first-principle calculation would help to fully understand the mechanism behind the enhancement of the thermal conductivity in VO_2.

All the electronic devices or circuitry could generate excess heat while operating, so the thermal management is essential to their reliability [220]. Our discovery provides a general idea of the realization of high thermal conductivity materials. Working at the structural transition point of phase change materials could potentially create a thermal path to efficiently conduct the heat outside the material and make the device work at an optimal temperature. The low-frequency phonons usually dominate the heat transport, so the soft modes in materials like VO_2 suggest potential applications in temperature-tunable thermal

switches [221].

3.1.5 Conclusion

We did the electrical and thermal transport measurements in VO_2 single crystals. The electrical conductivity is enhanced at the transition by a factor of $10^4 \sim 10^5$, accompanied by a sharp drop of the thermal power S. By conducting the thermal transport measurement with an extremely slow sweeping speed of temperature, a narrow thermal conductivity peak is revealed within the MIT of VO_2 single crystals. The thermal conductivity was measured in a magnetic field up to 13.9 T parallel or perpendicular to the heat current, which didn't show obvious dependence on H. This indicates that the strong enhancement of the thermal conductivity could possibly due to the softening of certain phonon modes at the phase transition [215, 213, 214] and induce a strong enhancement of the thermal conductivity.

3.2 Anomalous Thermal Conductivity Across the Structural Transition in $SmBaMn_2O_6$ Single Crystals

To understand whether the enhancement of thermal conductivity could take place at different types of phase transitions, we conduct thermal measurements in $SmBaMn_2O_6$ single crystals which has both structural and magnetic phase transitions. In $SmBaMn_2O_6$, successive phase transitions in charge, spin and lattice degrees of freedoms take place at $T_{co1} \sim 362$ K, $T_{co2} \sim 190$ K and $T_N \sim 175$ K. An enhancement of thermal conductivity is only observed at the structural transition around T_{co1} while it is absent at the structural transition around T_{co2}. One possible explanation is the spin-phonon coupling in this material strongly modifies the phonon spectra and prevent the evolution of soft-phonon modes around the antiferromagnetic transition T_N, which lies right below T_{co2}. Our study provides a way to look for enhanced thermal conductivity in materials where multiple phase transitions coexist.

3.2.1 Two-step Charge-orbital-order (COO) Transition in $SmBaMn_2O_6$

In solid-state materials, structural transitions are always accompanied by changes in other physical properties, such as electrical conductivity, magnetic susceptibility or thermal conductivity. Enhancement of thermal conductivity across the metal-insulator transition has been reported recently in VO_2 [189]. VO_2 undergoes a first order metal-to-insulator phase transition at around $T_s \sim 340$ K due to a crystal structure and electronic structure change.

The thermal conductivity is enhanced by 1 order of magnitude at the transition temperature T_s, which is possibly due to the softening of certain phonon modes at the structural phase transition [215]. It is necessary to further address whether the enhancement of thermal conductivity could also take place at other types of phase transitions and how the ordering states in other degrees of freedom, such as magnetic ordering, could possibly affect it.

Perovskite-type manganites, which have been extensively studied due to its abundant properties originate from the interplay among the charge, spin, orbital and lattice degrees of freedom, could be one platform to further study this topic [222]. The colossal magnetoresistance (CMR) effect, i.e. the dramatic change of electrical resistivity under a magnetic field, has attracted researchers' attention due to its potential applications in the memory device heads and sensors [5, 6]. The ferroelectricity driven by the charge-ordering state and the tilting of MnO_6 octahedra in layered manganites is also widely studied because of its expected application in electronic devices such as ferroelectric RAM and capacitors [223, 224]. In this chapter, we focus on the A-site ordered double-perovskite $SmBaMn_2O_6$. The A-site ordered $SmBaMn_2O_6$ compounds undergo a two-step charge-orbital-order (COO) transition at T_{co1} and T_{co2} as temperature decreases. This material has a first-order structural phase transition at $T_{co1} = 380$ K from low-temperature tetragonal phase to high-temperature orthorhombic phase [26]. X-ray scattering and electron diffraction reveal a long-range COO phase below T_{co1} [225, 226]. The stacking manner of ab planes change from $AABB$- to $ABAB$-type around $T_{co2} = 190$ K is evidenced by X-ray scattering and Raman scattering [227]. At T_{co2}, the space group changes from nonpolar $Pnam$ to polar $P2_1am$, which suggests a ferroelectric transition due to the rearrangement of charge and orbitals at T_{co2} [224]. Yamada $et.\ al.$ reports that the antiferromagnetic (AFM) transition happens at $T_N = 175$ K, which is just below T_{co2} [228].

We conduct electrical transport, magnetic susceptibility, and thermal transport measurements in $SmBaMn_2O_6$ single crystals. Both electrical resistance and magnetic susceptibility show abrupt change accompanied by a narrow hysteresis loop at $T_{co1} \sim 362$ K. Another anomaly takes place between 150 K and 210 K (around T_{co2}) which is manifested by a much broader hysteresis loop. The total thermal conductivity is enhanced by 3$\sim$4 times within the metal-insulator-transition (MIT) at T_{co1}, while no obvious enhancement is observed around T_{co2}. The explanation on the absence of thermal conductivity peak at the structural transition at T_{co2} is further discussed in this chapter.

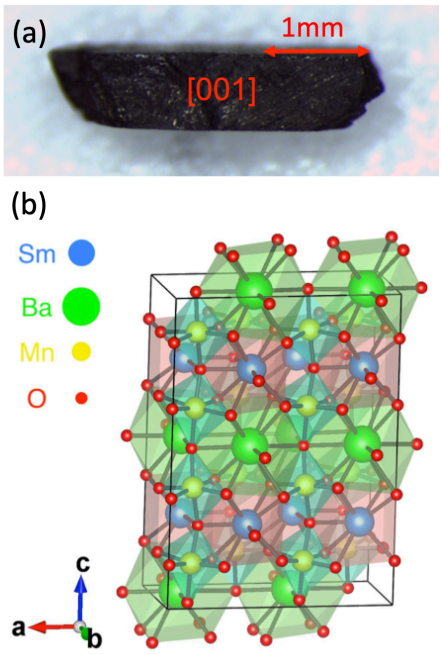

Figure 3.5: (a) A polished single crystal of $SmBaMn_2O_6$ (Sample 1) with the front surface to be [001]. (b) Crystal structure of $SmBaMn_2O_6$ at 300 K [224].

3.2.2 Thermal Conductivity Measurement Setup for $SmBaMn_2O_6$

The $SmBaMn_2O_6$ single crystals being used in our experiments are grown by floating zone method [228]. The single crystal is polished into a bar shape for electrical and thermal transport measurement. Sample 1 has a dimension of $0.6 \times 0.65 \times 3$ mm (as shown in Figure 3.5 (a), Sample 2 has a dimension of $0.45 \times 0.6 \times 2.5$ mm. Sample 3 is cut from the same batch of Sample 2, which has a mass of 4.15 mg and is used for magnetization measurement. The crystal structure of $SmBaMn_2O_6$ at 300 K is shown in Figure 3.5 (b), where SmO and BaO layers stack alternatively along the crystal c axis. All the measurements are conducted in a Physical Properties Measurement System (PPMS) DynaCool from Quantum Design.

The experimental setup for the electrical and thermal transport measurement is similar to the setup in reference [189]. A bar-shape $SmBaMn_2O_6$ single crystal is mounted vertically on a sapphire substrate. A resistive heater is attached on top of the sample by the H74F thermal epoxy to provide a thermal gradient inside the [001] plane of the sample. In order to provide better electrical contact with the sample, we evaporate gold contacts on the front surface of the sample and then attach four gold wires on the contacts with silver

epoxy. These four gold wires are used for four-probe resistance measurement as well as thermal power measurement. Two type-E thermocouples are thermally linked to the back side of the sample with the thermal joint compound. The whole setup is mounted on top of a self-designed thermal transport puck, which is compatible with the PPMS DynaCool system.

Four-probe resistance measurement is conducted by the Electrical Transport Option (ETO) of PPMS. The thermal power and thermal conductivity are measured by a pulsed power technique [203, 189]. A periodic AC current($f = 0.01$ Hz) is applied through the resistive heater by a Keithley 6221 DC and AC current source to generate a thermal gradient across the sample. The thermal power is measured through two of the electrical contacts by a Keithley 2182A nanovoltmeter. The voltage across the two thermocouples is read by another Keithley 2182A nanovoltmeter, which could be used to calculate the temperature gradient across the sample. During the thermal transport measurement, the sample temperature is swept with a speed of 0.1 K/min. Magnetization is measured using the Vibrating Sample Magnetometer (VSM) of PPMS. For the temperature dependent measurement, we first cool the sample down to 100 K without applying any magnetic field. Then we apply a magnetic field of 3 T at 100 K and measure the magnetization during warm up and cool down.

3.2.3 Anomalous Thermal Conductivity Across the Two-step Charge-orbital-order (COO) Transition

Figure 3.6 (a) shows the four-probe resistance measured in $SmBaMn_2O_6$ Sample 1 and Sample 2. A slowly vary AC current is applied inside the [001] plane of the sample. Sample 1 undergoes an MIT at $T_{co1} \sim 362$ K with a resistance increase about 20 times during cool down. The resistance of Sample 2 only increases about 10 times at $T_{co1} \sim 354$ K. Both samples show a steep change on resistance with a thermal hysteresis loop at T_{co1} which is clear evidence of a first-order phase transition [228]. The difference between the transition temperature T_{co1} during warm up and cool down is around 6 K. The difference in the transition temperature between Sample 1 and 2 could be caused by the valence distribution of Mn ions. The charge-ordering is from the mixed valence of the two Mn ions, one is + 3 and the other one is + 4. The charge ordering temperature is very sensitive to the valence distribution, which means a slight deviation from this +3/+4 valence combination could change or even eliminate the charge ordering transition [229, 230]. The deviation of the valence from +3/+4 is reflected by the inhomogeneous oxygen deficiency in the different parts of the as-grown crystals during the melting process. Since the sample was grown under Ar,

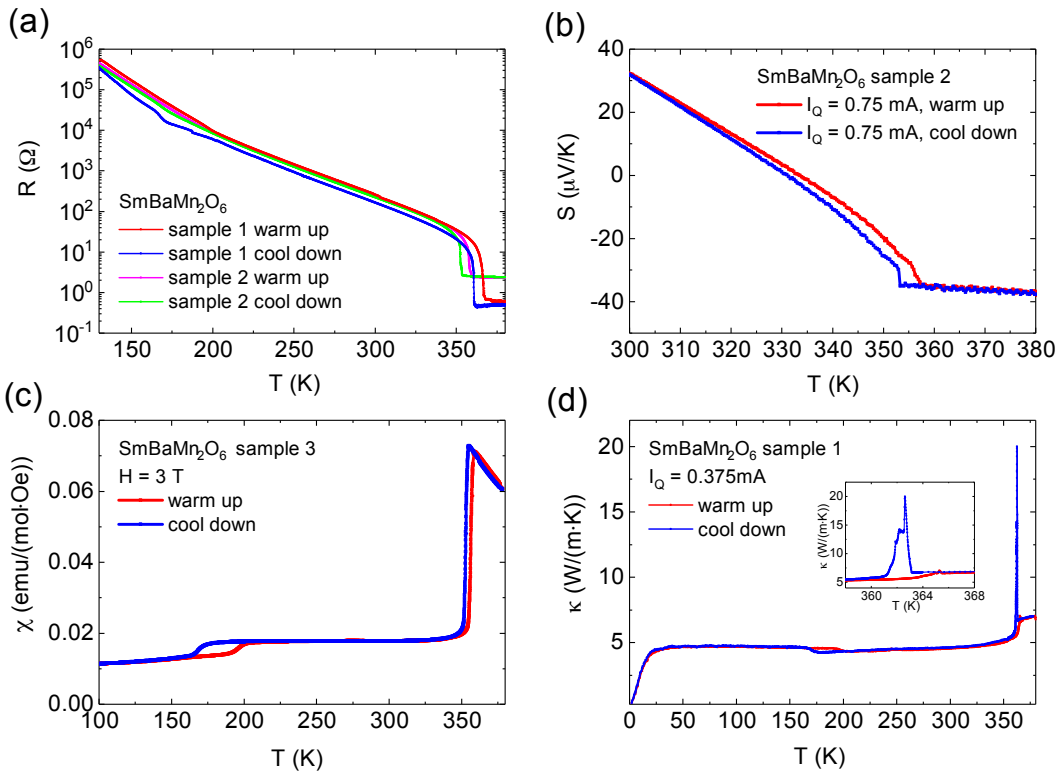

Figure 3.6: (a) Four-probe resistance R vs. T in $SmBaMn_2O_6$ Sample 1 and 2. The current is applied in the [001] plane. (b) Seebeck coefficient S vs. T in $SmBaMn_2O_6$ Sample 2. The sample temperature was swept at a rate of 0.1 K/min. (c) Temperature dependence of magnetic susceptibility in $SmBaMn_2O_6$ Sample 3 taken with H = 3 T. (d) Measured total thermal conductivity κ_{tot} vs. T in $SmBaMn_2O_6$ Sample 1 with a slower sweeping speed of temperature ($\sim$ 0.02 K/m.in) around T_{co1}. The inset figure is a zoom in of κ_{tot} around T_{co1}, which shows the thermal conductivity increases for about 4 times across T_{co1} during cooling down. In (a) $\sim$ (d), red (magenta) curves denote warming up while blue (green) curves denote cooling down.

so the oxygen should be deficient which means more +3, as $SmBaMn_2O_{6-x}$. Different x values in our sample could cause a difference in the transition temperature. Upon further cooling, another anomaly is observed between 150 K and 210 K (around $T_{co2} \simeq 190$ K) in resistance, which is consistent with the observation in reference [228]. The temperature dependent Seebeck coefficient changes sign at 330 K and reach an almost constant value of -34 μV/K at T_{co1} when entering the metallic state (as shown in Figure 3.6 (b)). The temperature dependent magnetic susceptibility shows a steep change accompanied by a narrow hysteresis loop at T_{co1} (as shown in Figure 3.6 (c)), while a much broader hysteresis loop is observed between 160 K and 210 K (around T_{co2}). Nakajima *et. al.* have reported that the magnetization curve has a broad peak at around 250 K in the pulverized sample, which is assigned to the AFM transition [26, 231]. However, this peak is strongly suppressed in our

measurement as well as Yamada $et.\ al.$'s experiments, which indicates a strong dependence of sample properties on the system size.

The temperature dependent total thermal conductivity between 2 K and 380 K of Sample 1 is shown in Figure 3.6 (d). The thermal conductivity increases about 50% from a low-temperature insulating state to a high-temperature metallic state at T_{co1}. The inset of Figure 3.6 (d) shows the thermal conductivity is enhanced by 3$\sim$4 times within the MIT during cool down, while the enhancement during warm-up is much weaker. Between 150 K and 210 K, another anomaly which is accompanied by a hysteresis loop is observed on the thermal conductivity. Figure 3.7 (a) shows the zoom-in of the total thermal conductivity between 2 K and 300 K. Recently, the enhancement of thermal conductivity within the MIT of oxides has been reported in the VO_2 single crystals, which is claimed to be related to the soft phonons at the structural transition [189]. Although the phase transitions at T_{co1} and T_{co2} are both accompanied by structural transitions in $SmBaMn_2O_6$, no obvious enhancement of thermal conductivity is observed around T_{co2}. Instead, the thermal conductivity shows a dip around T_{co2} before entering the AFM state.

We vary the temperature sweeping speed as well as the heater current to further study the thermal conductivity peak within the MIT. Figure 3.7 (b) (3.7(c)) shows the total thermal conductivity measured in Sample 1 with a temperature sweeping speed of 0.1 K/min (0.02 K/min). The thermal conductivity peak is more prominent with a slower sweeping speed of temperature because a faster sweeping speed of temperature will smear out the enhancement effect that only happens in a very narrow temperature range. The total thermal conductivity shows a non-monotonic dependence on the heater current, which contrasts to the monotonic behavior observed in the VO_2 single crystals [189]. Furthermore, the thermal conductivity shows comparable enhancement during both warm up and cool down in VO_2, while it only shows obvious enhancement during cool down in $SmBaMn_2O_6$. Figure 3.7 (d) shows the total thermal conductivity measured in Sample 2 with a temperature sweeping speed of 0.1 K/min. The thermal conductivity peak in Sample 2 is lower than that in Sample 1.

3.2.4 Discussion

First of all, we ask if thermal conductivity peaks observed at the structural transition $T_{co1} \sim 362$ K arises from the latent heat. Latent heat is released at the first-order structural transition. This heat leads to a sudden rise in the overall temperature, which changes the overall trend in the thermocouple voltage raw data. After analyzing our raw data more seriously, we figured out that the raw data actually shows the effect of the latent heat at the

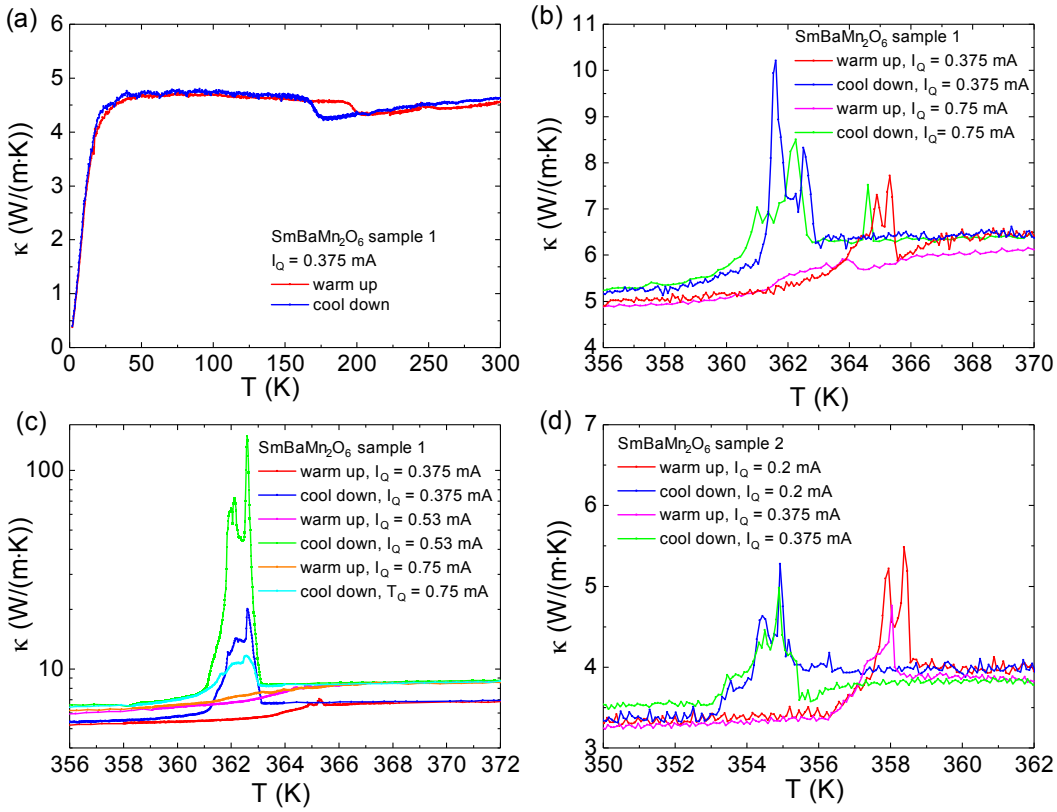

Figure 3.7: (a) Measured total thermal conductivity κ_{tot} vs. T in $SmBaMn_2O_6$ Sample 1 below 300 K. (b) Total thermal conductivity κ_{tot} vs. T in $SmBaMn_2O_6$ Sample 1 with different heater currents. The temperature sweeping speed is 0.1 K/min around T_{co1}. (c) Total thermal conductivity κ_{tot} vs. T in $SmBaMn_2O_6$ Sample 1 with different heater currents. The temperature sweeping speed is 0.02 K/min around T_{co1}. (d) Total thermal conductivity κ_{tot} vs. T in $SmBaMn_2O_6$ Sample 2 with different heater currents. The temperature sweeping speed is 0.1 K/min around T_{co1}.

structural transition. Figure 3.8 plots the thermocouple reading of the sample across the phase transition around T_{co1} with different temperature sweeping speed. As shown below in Figure 3.8 (a), the upper envelope of the thermocouple reading becomes higher at the transition point. The upper envelope corresponds to "heater off", which shows a change of about 2×10^{-6} V at the transition. This corresponds to a temperature change of about 30 mK on the sample. We see that the latent heat released at the structural transition brings the sample temperature up by 30 mK. In Figure 3.8 (b), with a slower sweeping speed of temperature, the upper envelope shows a smaller change of 1.5×10^{-6} V across the transition, which corresponds to a temperature change of 22 mK. We see that with a slower sweeping speed of temperature, the sudden temperature change on the sample is smaller since the total latent heat released at the transition process should be constant. We like to

further emphasize that we measure the change of the temperature gradient between "heater on" and "heater off". The relative change of thermocouple reading leads to the thermal conductivity. As a result, this setup excludes the effect of the latent heat since both the "heater on" and "heater off" data setup should respond to the same latent heat release.

The sweeping rate dependence of the raw data is more convincing. As we sweep the sample overall temperature (at 0.1 K/min, as shown in Figure 3.8 (a)), we observe a quick shrink of the temperature gradient across the sample at the phase transition, even though the heater power is the same. We interpret this quick shrink of the temperature gradient as the rapid enhancement of the sample thermal conductivity. Interestingly, as we sweep the overall temperature with a much slower rate (at 0.02 K/min, as shown in Figure 3.8 (b)), this effect of the shrinking temperature gradient gets much stronger. In other words, at a slower rate, we are able to catch the sharp change of the thermal conductivity. We would like to point out that the sweep rate dependence is opposite to the expectation based on the latent heat release. Across the first-order phase transition, the same sample releases the same amount of latent heat. At a slower sweep rate, the latent heat has a much longer time to release. As a result, the temperature variation caused by the latent heat release should be much weaker, in contrast to our observation of the stronger effect (as shown in Figure 3.8 (c)).

More importantly, we may estimate the latent heat releasing power across T_{co1} by assuming that the latent heat released at the transition is on the same order of magnitude as VO_2 [34]. Due to the sample heater, there will be a temperature gradient built up across the sample, which makes the temperature of the sample shows some inhomogeneity. Our experimental results (Figure 3.7 (c)) show a clear dependence on the heater power. To access the role of latent heat, we estimate the latent heat releasing power and our heater power across the transition at T_{co1}. We focus on the thermal conductivity peak measured with I_Q = 0.53 mA (RMS) during cool down in Figure 3.7 (c) for the estimation, because the peak shows the most significant enhancement. Since we are using the peak of the sine wave as the "heater on" status, the peak current should be I_{Qp} = 0.75 mA. For our 1 kΩ sample heater, the "heater on" power is 0.56 mW. Furthermore, based on that Sample 1's cross-section 0.6 mm $\times$ 0.65 mm and the distance between two thermocouple joints 1.25 mm, as well as the sample density 7.01 g/cm3, the sample volume between the two thermocouples corresponds to N = 6.92 $\times 10^{-6}$ mol. Assume the structural transition releases the same amount of latent heat as VO_2 (Q_L = 1020 cal/mol [34]), we find out a total latent heat of 29.5 mJ through the transition. Now, given the sweeping rate of 0.02 K/min and a transition width of about 2 K, the transition time takes 6000 s. The latent heat releasing power of this sample is 4.92 μW. Therefore, the sample heater power is more than 100 times bigger than

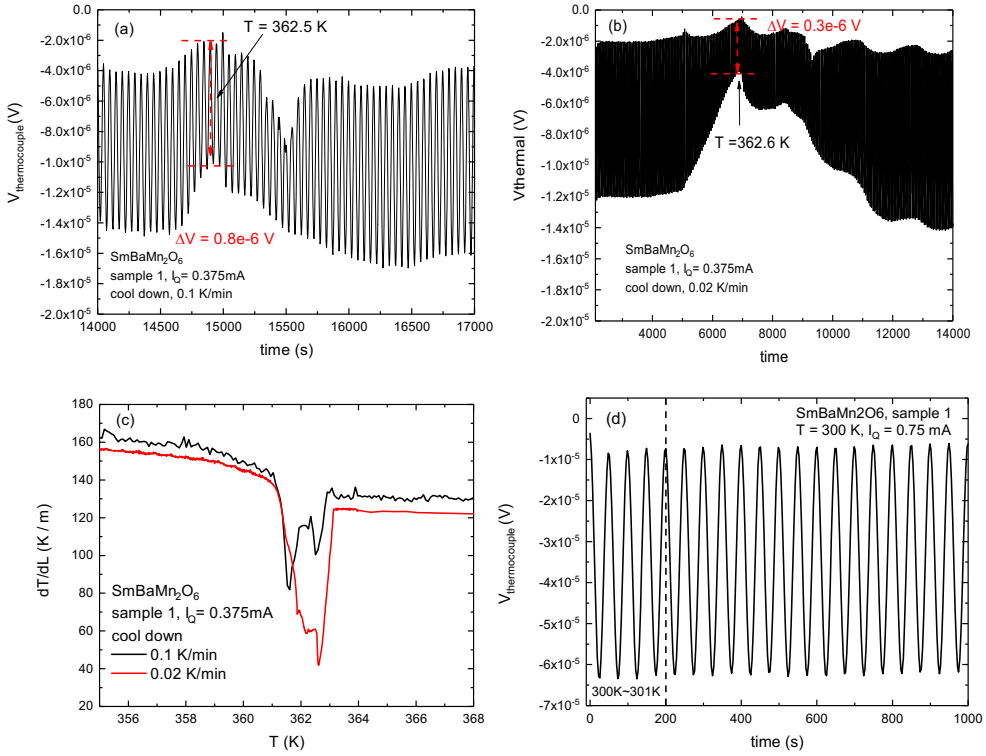

Figure 3.8: The raw data of the thermocouple voltage when a sinusoidal heating current is applied to the sample heater and the overall temperature is swept up at (a) 0.1 K/min and (b) 0.02 K/min. (c) The temperature gradient resulted from the steps described in Panel (a) and (b). (d) Detailed thermocouple voltage at 300 K used in our pulsed power method. The voltage change between "on" and "off" is the same as that measured in the same power of Figure 2.21.

the latent heat releasing power. As a result, we believe that the effect of the latent heat is negligible and the latent heat does not cause our observation of the thermal conductivity enhancement.

We would also like to point out here that the pulsed power technique produces similar results as the steady-state method. As we emphasize in the manuscript, a continuous temperature sweep is necessary to catch the observed narrow transition. However, to make sure that our pulsed power technique, we did the heating power tests with steady-state DC currents before the measurement to make sure the thermocouple reading from the pulsed power technique is the same as the steady-state measurement. Figure 2.21 (a) shows the thermocouple reading at 300 K when running different DC currents through the heater. The thermocouple voltage is proportional to the square of the heater current, which means the thermal gradient is linear with the heater power. With a heater current I_Q = 1 mA, the thermocouple reading difference between heater on and off is 6×10^{-5} V. Figure 2.21 (b)

shows the thermocouple reading vs. the heater power, which corresponds to the heater current in Figure 2.21 (a). It shows the thermocouple reading is linear with the heater power, which means the temperature gradient on the sample responds linearly to the heater power. Figure 3.8 (d) shows the comparison of the thermocouple reading with pulsed power technique when the temperature is slowly increasing from 300 K. I_Q is the RMS value of heater current, which means the peak current is also 1 mA. Since we are using the peak of the sine wave as heater "on" status and valley as heater "off" status, the difference between heater on and off at 300 K is about 5.8×10^{-5} V, which is within 5% error of the DC-current result. So we conclude that the pulsed power technique would bring comparable results for thermal conductivity as the pulsed power technique.

Now what is the origin of the thermal conductivity peak at T_{co1}? We note that the thermal conductivity peak at the MIT in VO_2 single crystal can likely be explained by a soft optical phonon mode which has been observed by neutron scattering [200]. VO_2 undergoes a first order MIT at around 340 K from the insulating monoclinic phase to the metallic rutile phase as temperature increases. Generally, at the structural transition, acoustic phonon modes soften because of the instability of the lattice structure. The decreasing of the phonon energy is overcompensated by a large increase of phonon population and its group velocity, which strongly enhances the thermal conductivity at the structural transition. In $SmBaMn_2O_6$, the thermal conductivity peak at T_{co1} can likely be explained with the same scenario.

The absence of such enhancement around T_{co2} may come from the adjacency between the structural transition at $T_{co2} \sim 190$ K and the AFM ordering at $T_N \sim 175$ K. First-principles calculation suggests strong spin-phonon coupling in perovskite-type manganites like $SrMnO_3$ and $Sr_{1-x}Ba_xMnO_3$ [232, 233, 234]. As the Ba concentration increases, one optical phonon mode rapidly softens at room temperature while other phonon modes remain unchanged. The infrared optical and inelastic x-ray scattering spectra confirm that only the soft phonon modes show remarkable variation with AFM transition for all doping level while other phonon modes are almost temperature independent. As temperature decreases, the continuous softening of this optical phonon is suppressed by the onset of the AFM phase. The soft phonon mode first hardens below T_N and then resoftens at a much lower temperature. Furthermore, the soft-phonon-mode frequency is even modified above T_N because of the strong AFM fluctuation near T_N, which also results in the disappearance of the thermal conductivity peak at T_{co2} [233]. This nonmonotonic temperature dependence of soft-phonon-mode frequency can be explained by considering the spin-phonon coupling:

$$\omega_{TO1}^2 = \omega_0^2 + \lambda \langle \mathbf{S}_i \cdot \mathbf{S}_j \rangle, \tag{3.2}$$

where ω_0 is a phonon frequency without magnetism, λ is a coupling constant, $\langle \mathbf{S}_i \cdot \mathbf{S}_j \rangle$ is the nearest-neighbor spin correlation function [235, 236]. By fitting the theoretical model with the infrared spectra data, the spin-phonon coupling constant in $Sr_{1-x}Ba_xMnO_3$ ($x = 0.3$) is 500 times stronger than that in $EuTiO_3$. We also observe that the total thermal conductivity of $SmBaMn_2O_6$ shows a dip at $T_s = 175K$ (200 K) during cooling down (warming up) and starts to increase as the temperature becomes lower. This is similar to the observations in other magnetic materials or CMR manganites, where $d\kappa/dT$ changes sign upon entering an FM or AFM transition [237, 238, 239, 240, 241]. These features can also be attributed to the strong spin-phonon coupling in these systems, where the critical scattering of thermal phonons on spin fluctuations leads to a dip on κ [242, 243, 244, 245]. In order to fully understand the thermal conductivity behavior in $SmBaMn_2O_6$, other measurement methods, as well as first -principles calculation are needed to illustrate the phonon spectra.

$SmBaMn_2O_6$ single crystals have MIT above room temperature at $T_{co1} \sim 362$ K. Such a high T_{co1} is very attracting from the aspect of device application [231]. The huge thermal conductivity peak provides a path to efficiently conduct the heat out of the device, which suggests a possible way to achieve thermal management in such kind of materials. The soft-phonon modes in this material suggest a potential application in temperature-tunable thermal switches [221].

3.2.5 Conclusion

In summary, we conduct electrical transport, magnetic susceptibility and thermal transport measurement in $SmBaMn_2O_6$ single crystals. Both electrical resistance and magnetic susceptibility show abrupt change accompanied by a narrow hysteresis loop at $T_{co1} \sim 362$ K. Upon further cooling down, another anomaly takes place between 150 K and 210 K (around T_{co2}) which is manifested by a much broader hysteresis loop. The total thermal conductivity is enhanced by 3$\sim$4 times within the MIT at T_{co1}, while no obvious peak is observed around T_{co2}. The enhancement of thermal conductivity within the structural transition at T_{co1} is likely due to the phonon softening. Around T_N, the spin-phonon coupling in this material strongly modifies the phonon spectra and prevent the evolution of soft-phonon modes. The hardening of soft-phonon modes around T_N could cause the absence of thermal conductivity peak around T_{co2}, which lies right above T_N.

CHAPTER 4

Heat Capacity Study in a Trigonal Superconductor Nb-doped Bi_2Se_3

In this chapter, we present the heat capacity study in a topological superconductor candidate, the Nb-doped Bi_2Se_3. The temperature dependence of the electronic heat capacity at the low-temperature end is helpful to reveal the superconducting gap structure. The related publication can be found in Ref. [93].

4.1 Nb-doped Bi_2Se_3: An Odd-parity Topological Superconductor With Nematic Order

Topological superconductors have fully gapped bulk band and gapless surface states. As an unconventional superconductor, topological superconductors with time-reversal-invariance (TRI) have attracted numerous attention due to its potential of holding itinerant Majorana fermions [246, 247, 248, 249, 250, 251]. Theoretical studies point out TRI topological superconductors can be achieved in materials with odd-parity pairing symmetry [85, 84]. Not many unconventional superconductors with odd-parities have been reported except for UPt_3 and Sr_2RuO_4. But none of them are qualified as a TRI topological superconductor.

Recently, a newly discovered superconductor $Cu_xBi_2Se_3$ [252] has been proposed as a candidate for topological superconductors with odd-parity [85]. Theoretical evidence shows that a spin-triplet pairing with odd parity is favored after including strong spin-orbit coupling in $Cu_xBi_2Se_3$ [85]. The high pressure study indeed shows that the absence of Pauli limiting in the upper critical field points to spin-triplet superconductivity [253]. The superconducting gap function also relates closely to parity. Previous theories show that for the gap function, an even parity has line-node states while odd parity has point nodes [85, 322, 255]. But some experiments seem to give contradictory results regards to its gap function and pairing symmetry. The temperature dependence of the specific heat suggests

a fully gapped, strong-coupling superconducting state [256]. A point-contact spectroscopy measurement presents a zero-bias conductance peak (ZBCP) which is due to surface states formed by Majorana fermions [322]. But later on, a scanning tunneling microscope (STM) measurement shows that the density of states at the Fermi level is fully gapped without any in-gap states [257]. Most recently, an unusual anisotropy in the Knight shift has been observed in the $Cu_xBi_2Se_3$ by nuclear magnetic resonance (NMR) measurements which indicates a spontaneous crystal symmetry breaking [88]. These contradictory results are explained by a later theory. Odd parity can also have a point-node state or even fully gapped state after considering the crystalline symmetry [87], which is consistent with a full superconducting gap found in the specific heat measurement [256] and the anisotropy in the Knight shift of NMR measurements [88].

Since then other doped Bi_2Se_3 system such as the Nb-doped Bi_2Se_3 has also been intensively studied. Recently, our group discovered that the magnetic response in the superconducting states strongly couples to the underlying trigonal crystal symmetry in Nb-doped Bi_2Se_3. This effect is manifested by the vanishing of the in-plane torque signal every 60° [93]. More importantly, the amplitude of the superconducting hysteresis loop is enhanced along one direction, which indicates the spontaneous breaking of the rotational symmetry. According to Fu's theory [87], the nematic order could happen in an odd parity topological superconductor. We are curious whether the superconducting gap is nodal or nodeless in this material. Following the pioneering work by Kriener $et.\ al.$ [256], we conduct the specific heat measurement in Nb-doped Bi_2Se_3. The specific heat at a temperature well below T_c could illustrate the structure of the superconducting gap. For fully gapped superconductor, the BCS theory predicts that the electronic specific heat well below T_c is dominated by an exponential dependence [258, 259, 260]:

$$C_{el} \approx \gamma_n T_c a e^{-bT_c/T} \tag{4.1}$$

where the normal-state electronic specific heat is $C_{en} = \gamma_n T$, and a and b are numerical constants. Such an exponential dependence with $b \sim 1.5$ implies a minimum excitation energy per particle of $\sim 1.5 k_B T_c$, where k_B is the Boltzmann constant [260]. But for a nodal structure, the electronic specific heat well below T_c has power-law dependence with T. For example, line nodes have $C_{es} \sim T^2$ while point nodes have $C_{es} \sim T^3$ [261].

4.2 Results: Heat Capacity Study in Nb-doped Bi_2Se_3

4.2.1 Heat Capacity Measurement in Nb-doped Bi_2Se_3

We measured the specific heat of two Nb-doped Bi_2Se_3 single crystal samples with the He-3 heat capacity option in the PPMS DynaCool system from Quantum Design. Sample 1 has a mass of 3 mg while Sample 2 is 12 mg. The specific heat is measured from 25 K down to 0.38 K. Figure 4.1 (a) shows the picture of sample 1 taken under the microscope. Sample 1 is mounted on top of the He-3 heat capacity puck with Apiezon N grease. Figure 4.1 (b) shows the total heat capacity taken in the superconducting state at H = 0 T and H = 0.75 T, which is right above the closing of the hysteresis loop at base T. Since the upper critical field H_{c2} of Sample 1 at T = 0.3 K is about 0.6 T, above 0.6 T the sample has totally entered the normal state. We can use the H = 0.75 T data as the normal-state heat capacity data. From Figure 4.1 (b) we can see that the heat capacity at H = 0 T and H = 0.75 T is the same above 4 K, which means the H = 0.75 T curve can be used as the normal state heat capacity C_n. The normal state heat capacity can be written as

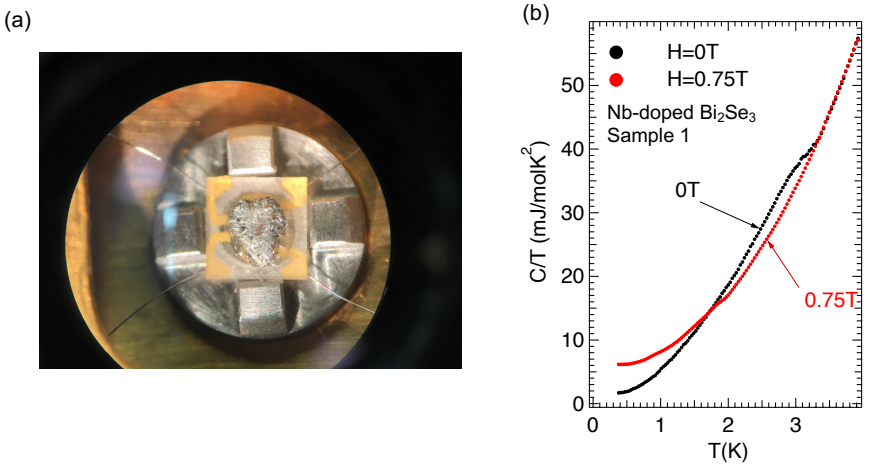

Figure 4.1: (a) Nb-doped Bi_2Se_3 Sample 1 mounted on the heat capacity measurement puck. (b) Measured total heat capacity over temperature $\frac{C}{T}$ vs. T in Sample 1 at H = 0 T and H = 0.75 T. The 0.75 T curve provides us a method to define the phonon contribution C_{ph}.

$$C_n = C_{en} + C_{ph} = \gamma_n T + aT^3 + bT^5 \tag{4.2}$$

where $C_{en} = \gamma_n T$ is the normal-state heat capacity, $C_{ph} = aT^3 + bT^5$ is the phonon heat capacity. The phonon heat capacity can be fitted by plotting $\frac{C_n}{T}$ vs. T^2 and fit with a

polynomial function. The linear term would be a in equation (4.2) and the second order term would be b. For the H = 0 T curve, after subtracting the phonon term C_{ph}, we can get the superconducting state electronic heat capacity C_{el}, which is plotted in Figure 4.2. A λ shaped kink indicates the superconducting transition. As T approaches 0, the heat capacity approaches a finite value. The 0 T heat capacity shows an exponential decay as T approaches 0 K, which is fitted by the dashed magenta curve in Figure 4.2. This exponential decay is expected for a fully gapped superconducting state from equation (4.1).

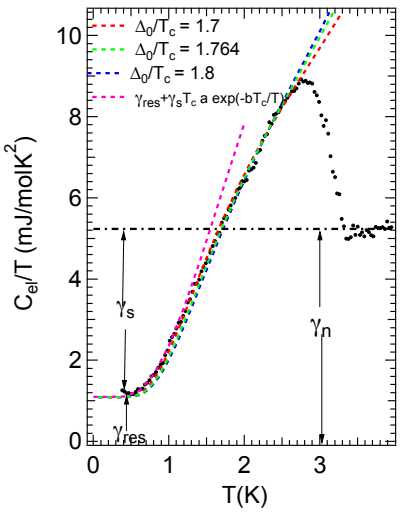

Figure 4.2: The superconducting-state electronic heat capacity of Nb-doped Bi_2Se_3 Sample 1 is shown as $\frac{C_{el}}{T}$ vs. T. A λ shaped kink indicates the superconducting transition. As T approaches 0, the heat capacity approaches a finite value, which gives a measure of the non-superconducting volume fraction of 20%. The 0 T heat capacity shows an exponential decay as T approaches 0 K (fitted by a dashed magenta curve), which is expected from a fully gapped state. The red, green and blue dashed lines are fittings with different parameters by the α model which is developed under the strong-coupling BCS theory. $\alpha = \Delta_0/T_c$, where Δ_0 is the superconducting gap size at 0 K.

4.2.2 Theoretical Fitting with "α Model"

To further prove that the superconducting state is consistent with the picture predicted by the BCS theory, we fit the superconducting-state heat capacity to the Bardeen–Cooper–Schrieffer (BCS)-type temperature dependence. We use the modified BCS model applicable to strong-coupling superconductors as proposed by Ref. [262] and [263], where it is called "α model" with $\alpha = \Delta_0/T_c$ and Δ_0 is the superconducting gap size at 0 K. The single-band-α-model of superconductivity is adapted from the BCS theory mainly to allow fits to electronic heat

capacity versus temperature data that deviates from the BCS prediction. In the BCS theory, $\alpha \approx 1.764$ is a fixed number. α is treated as an adjustable parameter in the α model when it is used to calculate the electronic free energy, entropy, heat capacity and thermodynamic critical field versus T. The BCS equations and limiting behaviors for the superconducting state thermodynamic properties can all be explicitly written in terms of α. For example, the normalized electronic heat capacity $\frac{C_{el}(T)}{\gamma_n T_c}$ versus temperature T in the superconducting state can be expressed as

$$\frac{C_{el}(T)}{\gamma_n T_c} = \frac{6\alpha^3}{\pi^2 t}\int_0^\infty f(1-f)(\frac{\tilde{E}^2}{t} - \frac{1}{2}\frac{d\tilde{\Delta}^2}{dt})d\tilde{\epsilon} \tag{4.3}$$

where the Fermi-Dirac distribution function is (with $E_F = 0$)

$$f = f(\alpha, \tilde{E}, t) = \frac{1}{e^{\alpha\tilde{E}/t}+1} \tag{4.4}$$

with

$$\frac{E}{k_B T} = \frac{\alpha\tilde{E}}{t} \tag{4.5}$$

$\tilde{\Delta}$, $\tilde{\epsilon}$ and t are dimensionless reduced variables

$$\tilde{\Delta} = \frac{\Delta}{\Delta(0)}, \quad \tilde{\epsilon} = \frac{\epsilon}{\epsilon(0)}, \quad t = \frac{T}{T_c} \tag{4.6}$$

From the BCS equation which describes the energy of an electron excited above the superconducting gap

$$E = \sqrt{\epsilon^2 + \Delta^2} \tag{4.7}$$

We can write down the reduced energy as

$$\tilde{E} = \frac{E}{\Delta(0)} = \sqrt{\tilde{\epsilon}^2 + \tilde{\Delta}^2} \tag{4.8}$$

In order to obtain C_{el} at a particular t, we have to first determine $\tilde{\Delta}$ at t using the following gap equation

$$\int_0^{\frac{k_B\Theta_D}{\Delta(0)}} \frac{d\tilde{\epsilon}}{\tilde{E}}\, tanh(\frac{\alpha\tilde{E}}{2t}) = ln[\frac{2k_B\Theta_D}{\Delta(0)}] \tag{4.9}$$

We can numerically solving equations (4.8) and (4.9) for $\tilde{\Delta}$ at fixed values of t.

We tried to reproduce the data with $C_{el}(T)/T = \gamma_{res} + C_{el}(T)//T$ using the theoretical curve C_{el} calculated by the α model (equation (4.3)). The red, green and blue dashed lines in Figure 4.2 show the theoretical fittings with different parameters by the α model.

Overall, $\alpha = 1.764$ gives the best fit of the heat capacity trace below T_c. In a sample with part of it non-superconducting, $\gamma_n = \gamma_s + \gamma_{res}$, in which γ_s comes from the superconducting part and γ_{res} from a residual non-superconducting part. From the calculation, we get $\gamma_n = 5.24$ mJ/molK^2, $\gamma_s = 4.15$ mJ/molK^2 and $\gamma_{res} = 1.09$ mJ/molK^2. So the superconducting volume fraction is $\frac{\gamma_s}{\gamma_n} = 79.2\%$, which is consistent with the results of magnetic susceptibility measurements [93].

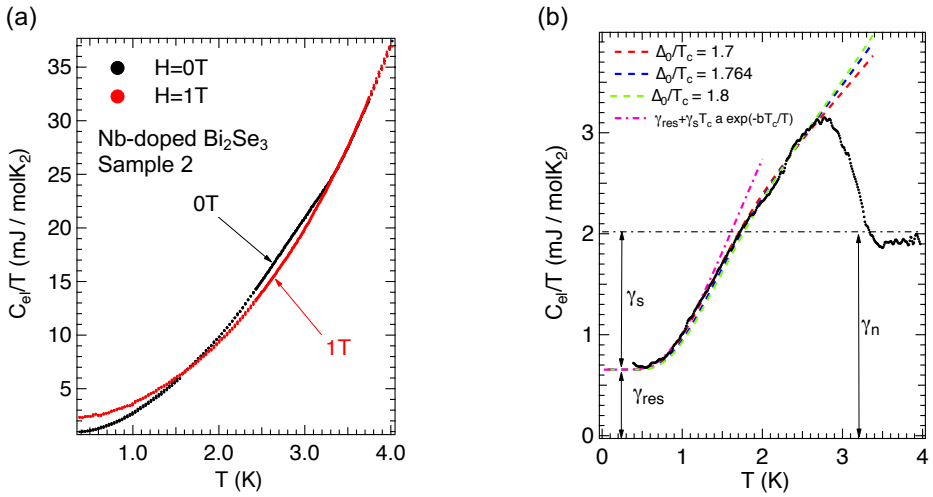

Figure 4.3: (a) Measured total heat capacity over temperature $\frac{C}{T}$ vs. T in Nb-doped Bi_2Se_3 Sample 2 at H = 0 T and H = 1 T. The 1 T curve provides us a method to define the phonon contribution C_{ph}. (b) The superconducting-state electronic heat capacity of Nb-doped Bi_2Se_3 Sample 2 is shown as $\frac{C_{el}}{T}$ vs. T. A λ shaped kink indicates the superconducting transition. As T approaches 0, the heat capacity approaches a finite value, which gives a measure of the non-superconducting volume fraction of 33%. The 0 T heat capacity shows an exponential decay as T approaches 0 K (fitted by a dashed magenta curve), which is expected from a fully gapped state. The red, green and blue dashed lines are fittings with different parameters by the α model which is developed under the strong-coupling BCS theory. $\alpha = \Delta_0/T_c$, where Δ_0 is the superconducting gap size at 0 K.

Similar measurement is also conducted in Nb-doped Bi_2Se_3 Sample 2. Figure 4.3 (a) shows the measured total heat capacity over temperature $\frac{C}{T}$ vs. T in Sample 2 at H = 0 T and H = 1 T. The upper critical field H_{c2} of Sample 2 at T = 0.3 K is higher than H_{c2} in Sample 1. Above 1 T, Sample 2 has totally entered the normal state. We can use the H = 1 T data as the normal-state heat capacity data.The phonon contribution can be fitted from the 1 T curve. After subtracting the phonon heat capacity C_{ph}, the superconducting-state electronic heat capacity is plotted in Figure 4.3 (b). The 0 T heat capacity shows an exponential decay as T approaches to 0 K, which is consistent with the result in Sample

1. After fitting with the α model, we get $\gamma_n = 2.02$ mJ/molK^2, $\gamma_s = 1.36$ mJ/molK^2 and $\gamma_{res} = 0.65$ mJ/molK^2. So the superconducting volume fraction is $\frac{\gamma_s}{\gamma_n} = 67\%$.

4.3 Conclusion

We performed heat capacity measurements from 0.38K to 25K at 0, 0.75 and 1T field in two Nb-doped Bi_2Se_3 samples. For both samples, the heat capacity show exponential decay when T approaches zero. This exponential decay indicates a nodeless superconducting gap structure. Both the nematic order observed in the torque magnetometry measurement and the nodeless gap structure obtained by the heat capacity measurement indicate an odd parity topological superconductor. Other experiments, such as the penetration depth measurements, would give clear answers on whether the superconducting gap has a node.

CHAPTER 5

Spontaneous Nernst Effect in an Iron-based Superconductor $Fe_{1+y}Te_{1-x}Se_x$

In this chapter, we present a study of the Nernst effect in an iron-based superconductor with a non-trivial band topology $Fe_{1+y}Te_{1-x}Se_x$. A non-zero Nernst signal is observed in a narrow temperature region around the superconducting transition temperature T_c at a zero field. This anomalous Nernst signal shows symmetric dependence on the external magnetic field and indicates an unconventional vortex contribution in an s-wave superconductor with a strong spin-orbit coupling, which is originated from the local magnetic moments of the interstitial Fe atoms. Our experiments also provide the first evidence of a locally broken time-reversal symmetry in bulk $Fe_{1+y}Te_{1-x}Se_x$ single crystals.

5.1 Introduction on $Fe_{1+y}Te_{1-x}Se_x$: a Topological Superconductor with Majorana Zero Modes

Topological superconductors have attracted tremendous attention due to its potential of hosting Majorana zero modes (MZM) and further application in topological quantum computation [264, 265]. The theory has predicted that the iron-based superconductor $Fe_{1+y}Te_{1-x}Se_x$ could host a topological superconducting state on its surface [131, 132, 133], which was demonstrated in photoemission [134] and scanning tunneling spectroscopy measurements [135]. Apart from the Dirac dispersion in the surface state, a zero-energy bound states (ZBS) has also been observed at magnetic-field-induced vortices in $Fe_{1+y}Te_{1-x}Se_x$ [135, 136, 137], which indicates a Majorana bound states. Even more surprisingly, the robust ZBS was also found at each interstitial iron impurity by scanning tunneling microscopy in the absence of an external magnetic field [138]. Recently, Jiang $et.\ al.$ propose a theoretical explanation that magnetic impurity ions can generate topological vortices without external magnetic fields in s-wave superconductors with strong spin-orbit coupling. These quantum

anomalous vortices can even support robust Majorana zero-modes when the topological surface states are superconducting [139]. We are curious about how the topological vortices could affect the vortex flow in the vortex liquid state of a type-II superconductor. The best way is to conduct the Nernst effect measurement.

In this chapter, we report on a study of Nernst effect in an iron-based superconductor $Fe_{1+y}Te_{1-x}Se_x$. We observe a zero-field Nernst effect that appears around the superconducting transition temperature T_c. This spontaneous Nernst signal does not follow the temperature and field dependence of the thermal power, and occur only in the T range near T_c where the superconducting fluctuation is strong and vortex liquid is robust. This intrinsic spontaneous Nernst signal indicates the violation of local time reversal symmetry (TRS) in the superconducting state. The TRS in $Fe_{1+y}Te_{1-x}Se_x$ may be broken by pinning flux introduced by the interstitial iron impurity. To further understand the role of excess Fe atoms, we study a series of $Fe_{1+y}Te_{1-x}Se_x$ single crystals that have different T_c and different levels of excess Fe concentrations and demonstrate how they affect the spontaneous Nernst effect signal.

5.2 Sample Preparation and Experiments

The single crystals of the $Fe_{1+y}Te_{1-x}Se_x$ were grown by using a unidirectional solidification method [266]. There are different superconductivity for different sectional crystals in the grown ingot which the actual composition and extra iron in the crystals are variable. The as-grown $Fe_{1+y}Te_{1-x}Se_x$ single crystals were sealed in a vacuum quartz tube and annealed at $400°C \sim 450°C$ for 6 days to 50 days to make the Se/Te distribution more homogeneous. Sample 1 and sample 2 are annealed at 400°C for 50 days. Sample 3 is annealed at 450°C for 6 days, Sample 4 is annealed at 400°C for 7 days. Three sets of crystals are studied. The first set (sample 1) generally has the highest T_c and lowest bulk resistivity. The second set (Sample 2, 3, 4 and 5) have lower T_c and larger bulk resistivity. Sample 5 is the as-grown sample and has the lowest superconductivity temperature. The third kind are superconducting without annealing. Named as Sample 6, they are usually without shinning surfaces and are argued to be crystals without excess Fe [135]. (We note, however, transport measurements and energy-dispersive X-ray spectroscopy (EDX) measurements cannot exclude the existence of a small level of excess Fe in these nominally Fe-impurity-free samples). The dimensions for all 6 samples are listed in Table 5.1.

Resistivity and magnetization were measured in a Physical Properties Measurement System (PPMS) DynaCool from Quantum Design and shown in Figure 5.1. $Fe_{1+y}Te_{1-x}Se_x$ Sample 1 has the highest T_c and second lowest resistivity while Sample 5 has the lowest

T_c and highest resistivity. Sample 6 has the lowest resistivity. The zero-field-cool (ZFC) magnetization was measured with the magnetic field applied inside the ab plane of the crystal. The superconducting transition temperature T_c was defined as the temperature where resistivity drops to one half. The superconductivity fractional volume (SFV) was calculated from the ZFC data. Please refer to Table 5.1 for more details.

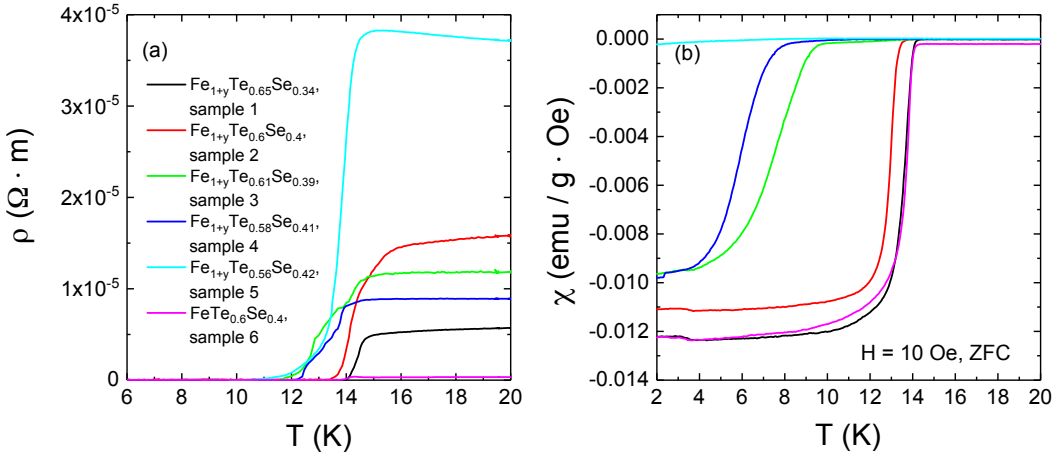

Figure 5.1: (a) Resistivity and (b) Zero-filed-cooled (ZFC) magnetic susceptibility in $Fe_{1+y}Te_{1-x}Se_x$ Sample 1 to Sample 6.

Table 5.1: Properties of $Fe_{1+y}Te_{1-x}Se_x$ Sample 1 to Sample 6

Sample	Formula	T_c	SFV	sample dimension (L× W × t)
1	$Fe_{1+y}Te_{0.65}Se_{0.34}$	14.39 K	88.8%	$4.4 \times 1 \times 0.15\ mm^3$
2	$Fe_{1+y}Te_{0.6}Se_{0.4}$	14.24 K	82.5%	$3.5 \times 1.2 \times 0.075\ mm^3$
3	$Fe_{1+y}Te_{0.61}Se_{0.39}$	13.15 K	73.2%	$3 \times 1.2 \times 0.125 mm^3$
4	$Fe_{1+y}Te_{0.58}Se_{0.41}$	13.39 K	74%	$3.5 \times 2 \times 0.0875\ mm^3$
5	$Fe_{1+y}Te_{0.56}Se_{0.42}$	13.75 K	1.7%	$5 \times 1.5 \times 0.1 mm^3$
6	$FeTe_{0.6}Se_{0.4}$	14.02 K	92.6%	$3 \times 1.5 \times 0.4 mm^3$

The Nernst and Seebeck effects were measured using the pulsed-power technique [189, 190] in a Physical Properties Measurement System (PPMS) DynaCool from Quantum Design and the Oxford Triton200-10 Cryofree Dilution Refrigerator. The signals are checked with static state method, in which the heating current is varied and the thermoelectric voltage signals are proportional to the heating power. In our geometry, the temperature gradient $-\nabla T$ is applied in the ab plane of the crystal ($-\nabla T \parallel \hat{\mathbf{x}}$). With a magnetic field along the crystal c axis ($H \parallel \hat{\mathbf{z}}$), the voltage measured along $\hat{\mathbf{y}}$ gives the raw Nernst signal

e_N [182, 267, 268, 269, 186], $e_N = \frac{V_y(B,T)}{|-\nabla T|d}$, in which d is the distance between the two voltage leads. Since there is always inevitable pickup of Seebeck signals in the Nernst Effect measurement due to the misalignment of contact leads, we have to subtract the Seebeck signal from the raw Nernst signal to reveal the intrinsic Nernst signal.

5.3 Results: Spontaneous Nernst Effect in $Fe_{1+y}Te_{1-x}Se_x$

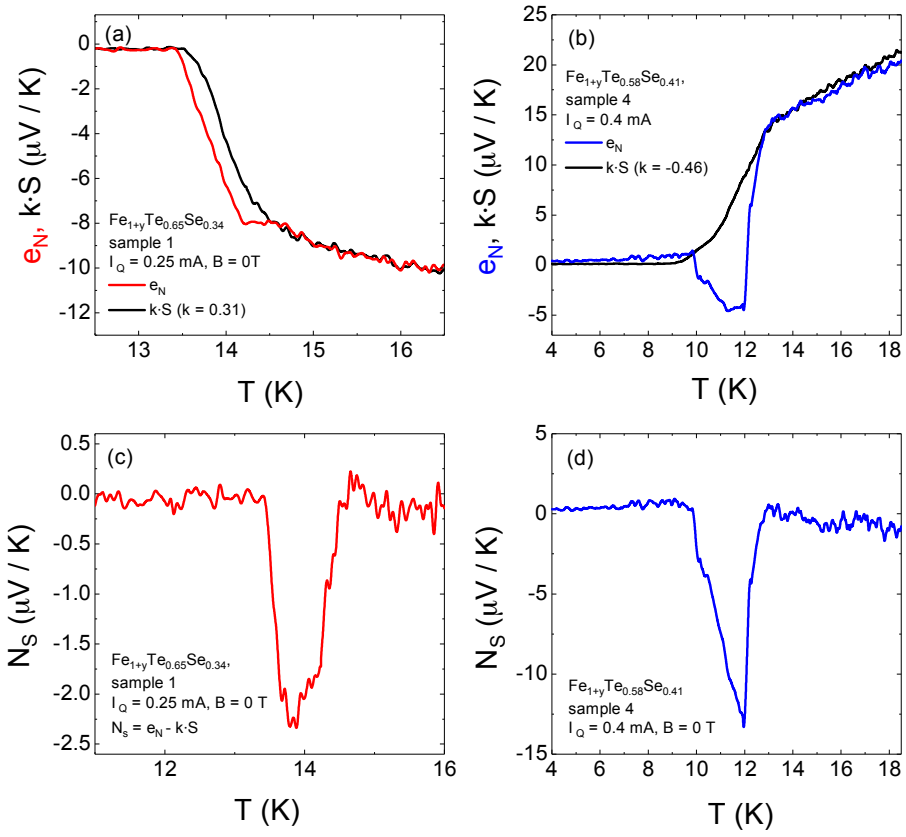

Figure 5.2: The zero-field thermoelectric responses of topological superconductor $Fe_{1+y}Te_{1-x}Se_x$. (a). Temperature T dependence of the thermopower kS (Seebeck signal) and the observed Nernst signal e_N in Sample 1. The thermopower signal S was scaled by a factor $k = 0.31$ to match the T-dependence of S and e_N. (b) The same T dependence of S and e_N for Sample 4, which is in different batch and with different T_c. Similar to Sample 1, Sample 4 also shows that the observed Nernst signal e_N matches the thermopower signal S very well at $T > T_c$. However, a sharp peak appears around T_c. For both samples, the intrinsic spontaneous Nernst signal is extracted by subtracting the scaled thermopower signal $N_S(T) = e_N(T) - k \cdot S(T)$. The heater resistance is 1kΩ for both sample.

Following the pioneering work [270], we determine the geometric pickup factor by scaling the $S - T$ curves to match the $e_N - T$ curves in the normal state (as shown in

Figure 5.2 (a)). This step assumes that there is no intrinsic zero-field Nernst effect signal in the normal metallic state, and the resulting scaling factor k reflects simply the (small) geometric factor due to the transverse contracts misalignment. The intrinsic Nernst signal N_S is given by subtracting the thermopower signal, viz.

$$N_S(B,T) = e_N(B,T) - k \cdot S(B,T) \tag{5.1}$$

in which k is a geometrical scaling factor. The geometrical scaling factor should be the same when the temperature is above or below the superconducting transition temperature since phonon dominates the heat transfer at such a temperature range. After subtracting the Seebeck signal, the intrinsic Nernst signal shows a prominent peak between 13.5 K and 14.5 K (Figure 5.2 (c)). This zero-field Nernst signal can be repeated in other $Fe_{1+y}Te_{1-x}Se_x$ samples with different Fe concentration. For example, N_S in Sample 4 is larger than the signal in Sample 1, as shown in Figure 5.2 (d). The spontaneous Nernst signal also shows some fluctuation even within the same sample. The sign and magnitude of the spontaneous Nernst signal vary at different channels in the same sample (as shown in Figure 5.3). Figure 5.3 plot the zero-field Seebeck signal S and Nernst signal e_N measured in all $Fe_{1+y}Te_{1-x}Se_x$ samples. For Sample 1,2 and 4, two Nernst channels are measured. For Sample 3, 5 and 6, three Nernst channels are measured. Take Sample 3 as an example (as shown in Figure 5.3 (c)), the magnitude and sign of the spontaneous Nernst signal across T_c ($\sim$ 14 K) are different among three Nernst channels. The spontaneous Nernst signal on channel e_{N1} and e_{N2} are negative while e_{N3} is positive.

We also did a power dependent measurement in another sample which come from the same batch of $Fe_{1+y}Te_{1-x}Se_x$ Sample 1 (we still call it Sample 1 in Figure 5.4) to see how the heater power affect the spontaneous Nernst signal. The data is plotted in Figure 5.4, there is a spontaneous Nernst signal shows across the superconducting transition. We can see that with higher heating power, T_c moves towards lower temperature, which is due to the heating up of the whole sample. The zero-field spontaneous Nernst signal also becomes a little bit smaller when apply larger heating power.

To study the field dependence of the Nernst effect, we measured the Seebeck and Nernst signal simultaneously in a magnetic field up to 14 T. Figure 5.5 (a) shows the raw Nernst signal e_N vs. B in Sample 1 at several selected temperatures across the superconducting transition. e_N shows an antisymmetric behavior with respect to B. The ordinary Nernst signal is obtained by the field-antisymmetrization to the Nernst curves in Figure 5.5 (a), i.e., $N_{AS} = \frac{1}{2}[e_N(B,T) - e_N(-B,T)]$ (shown in Figure 5.5 (c)). Above T_c, the ordinary Nernst signal becomes larger with decreasing T. At $T < T_c$, the ordinary Nernst signal starts at zero at low fields. Once B increases beyond the characteristic field B_m,

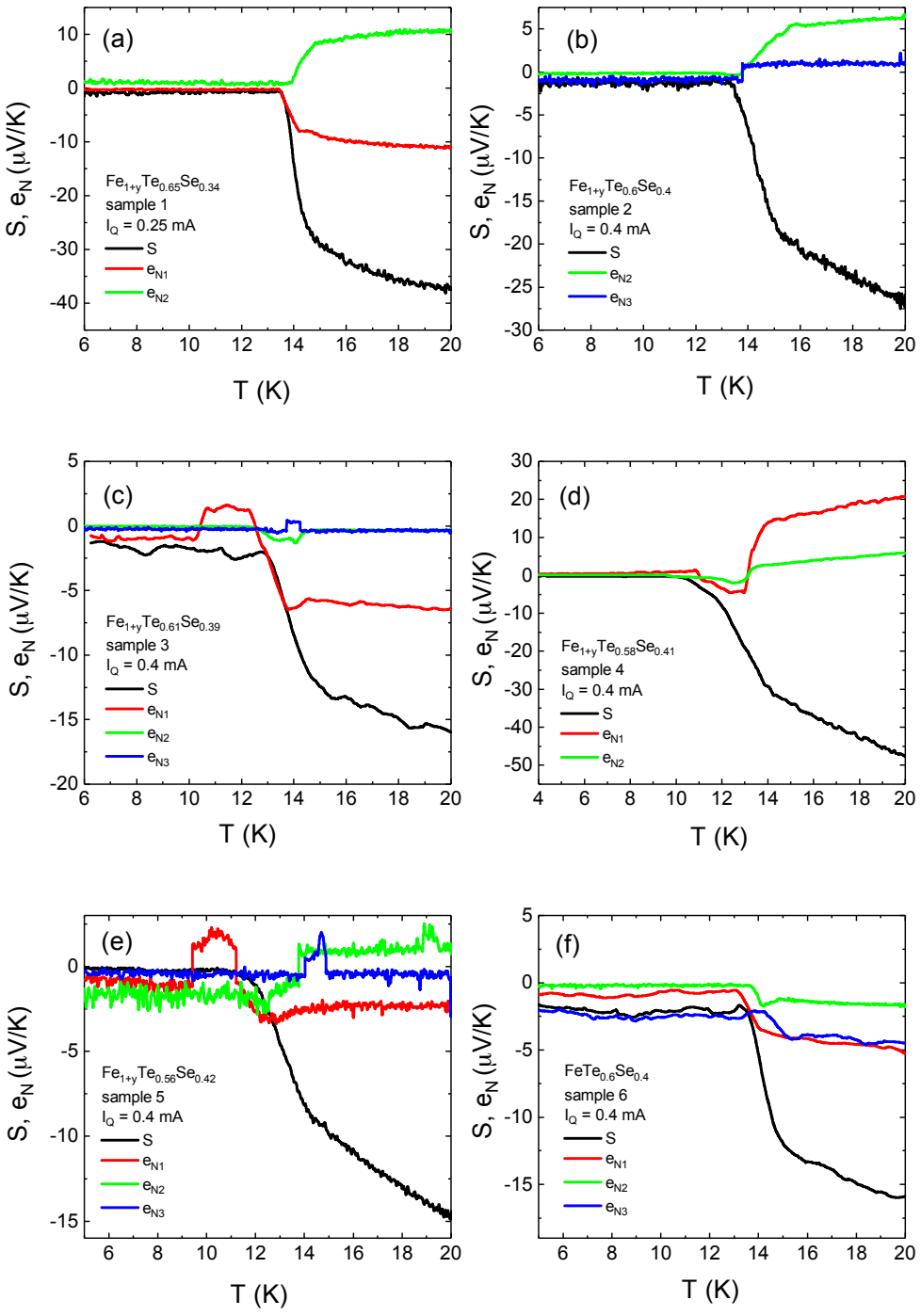

Figure 5.3: The zero-field Seebeck signal S and Nernst signal e_N measured in $Fe_{1+y}Te_{1-x}Se_x$ Sample 1 to Sample 6. For Sample 1,2 and 4, two Nernst channels are measured. For Sample 3, 5 and 6, three Nernst channels are measured. The heater resistance are 1 kΩ for all the samples.

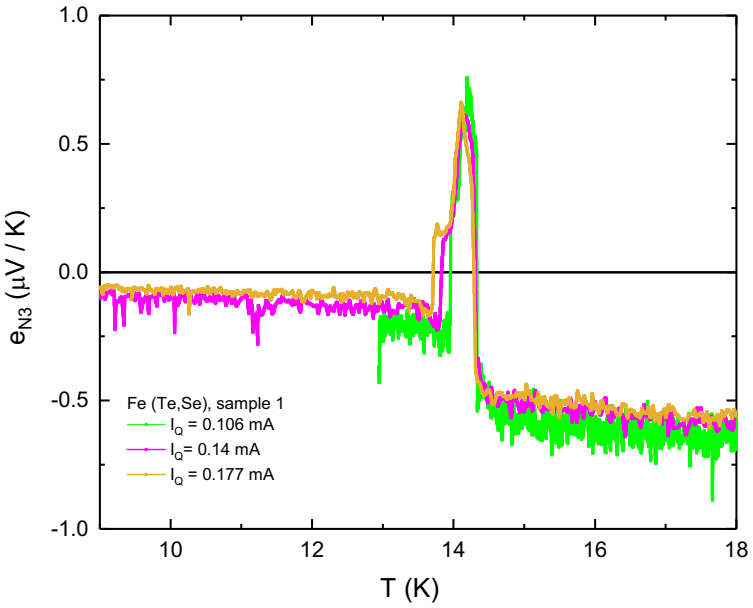

Figure 5.4: Measured Nernst signal e_N vs. T at zero field with different heater current for $Fe_{1+y}Te_{1-x}Se_x$ Sample 1. The heater resistance is 1 kΩ.

the ordinary Nernst signal increases to finite, reflecting the magnetic field driven transition from the vortex solid state at the low fields to the vortex liquid state in the high fields. The sign of the high field ordinary Nernst effect signal is consistent with that of the moving vortices [182, 268]. Finally, we plot the T dependence of ordinary Nernst coefficient N_{AS}/B at selected fields in Figure 5.5 (d), the results are consistent with the previous study [271]. The ordinary Nernst coefficient is strongly enhanced inside the vortex liquid state and vanishes gradually once it entering the vortex solid state. Its peak shifts to lower temperature at a higher field, which is similar to the behavior of thermally-driven vortices in cuprate [272, 273, 269], organic [274], and conventional superconductors [187].

Besides the ordinary Nernst signal, Figure 5.5 (a) also contains information about the field dependence of the anomalous Nernst signal shown in Figure 5.2 (c). By subtracting the Seebeck pickup $k \cdot S$ and ordinary Nernst signal N_{AS} from the observed Nernst data e_N, we obtain the anomalous Nernst signal N_{sym}, viz.

$$N_{sym}(B,T) = e_N(B,T) - k \cdot S(B,T) - N_{AS}(B,T) \tag{5.2}$$

This process is equivalent to subtract the Seebeck pickup from the raw Nernst signal and then do a field symmetrization. The anomalous Nernst signal N_{sym} is plotted in Figure 5.6, which shows a symmetric pattern with respect to B. N_{sym} is non-zero as $B \to 0$, which decreases as T increasing from 11 K to 14 K. This trend of N_{sym} at zero-field is consistent

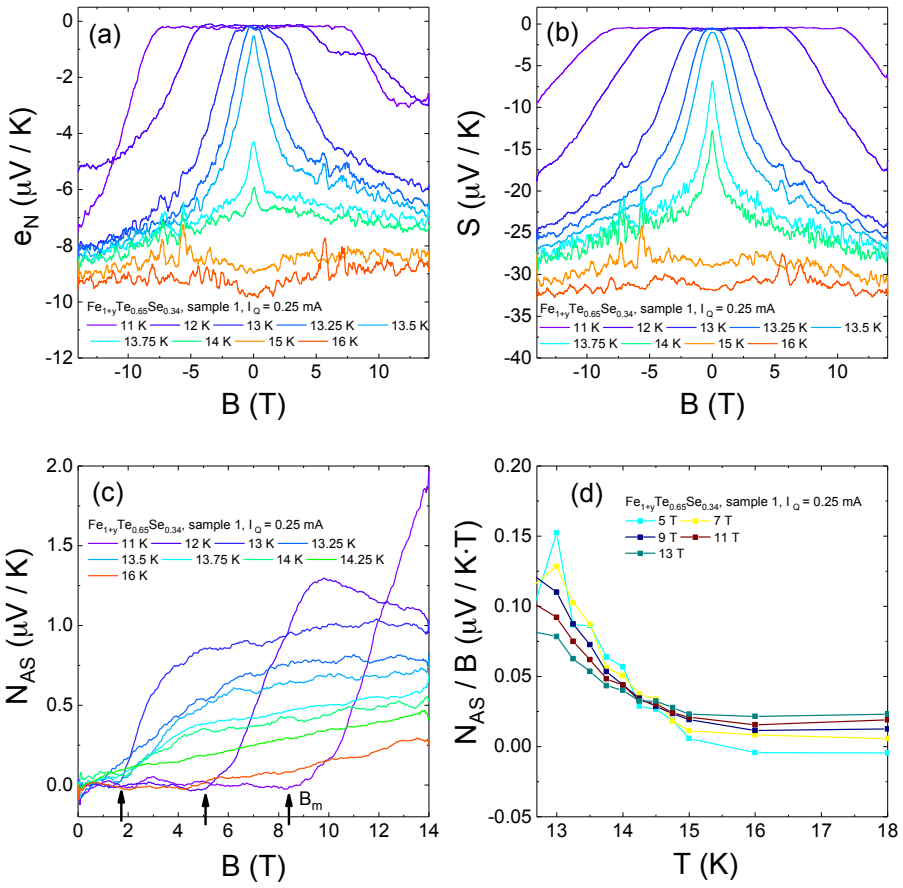

Figure 5.5: Observed (a) Nernst signal e_N and (b) Seebeck signal vs. magnetic field B at selected T from 11 K to 16 K in Sample 1. (c) Ordinary Nernst signal N_{AS} of Sample 1 following the standard B-antisymmetrization to curves in Panel (a). Arrows indicate the melting field B_m of the vortex solid state. (d) Temperature dependence of the ordinary Nernst coefficient $\frac{N_{AS}}{B}$ at selected B up to 13 T. The heater resistance is 1 kΩ.

with the T dependence of the spontaneous Nernst signal plotted in Figure 5.2 (c). Another important feature about the anomalous Nernst signal N_{sym} is a deep trench centered at $B = 0$ T. The trench becomes narrower as T increases from 11 K. This field-symmetric Nernst signal also shows broad dips that shifts to lower field as T increases. We indicate the location of theses broad dips by B_S and plot the temperature dependence of B_S in the inset of Figure 5.6. B_S gradually converges to zero field as T increases. This trend is similar to the T dependence of the melting field B_m, suggesting the vortex nature of the anomalous Nernst signal.

Theoretically speaking, such a zero-field Nernst signal is forbidden in a material that holds the TRS. A broken time-reversal symmetry (TRS) has been theoretically predicted in many high-T_c superconductors, such as cuprates [275, 276] and iron-base superconductors [277, 278, 279, 280]. In cuprates, the broke TRS is observed by angle-resolved

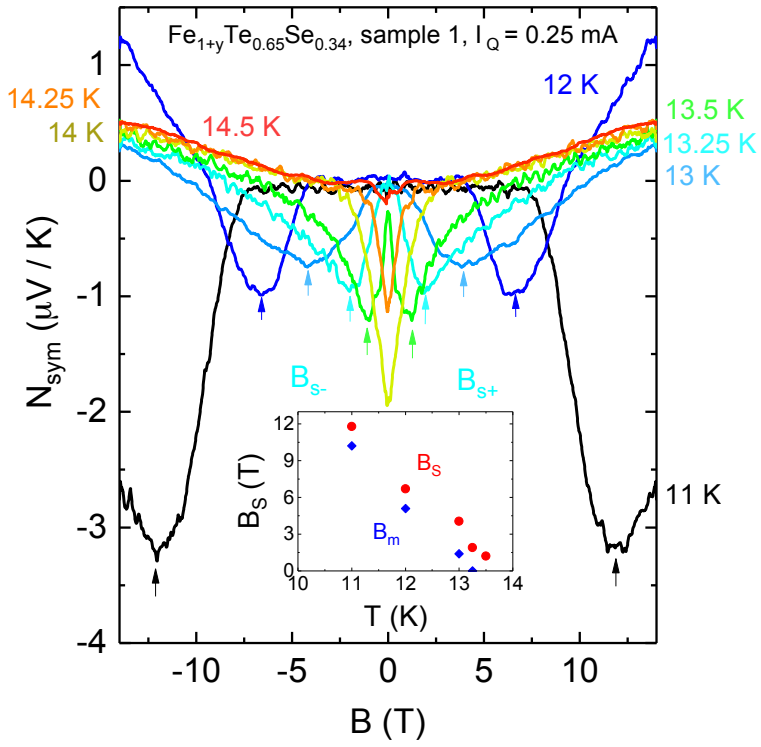

Figure 5.6: Magnetic field dependence of the intrinsic field-symmetrized Nernst signal. The Seebeck pickup has been subtracted, (see Eq (1)). Arrows indicate the location of the shoulder trend B_S. Inset shows the temperature dependence of B_S, compared with the melting fields B_m. As expected for the characteristic field scales in superconductors, both fields converge to zero as the T increases towards T_c. The heater resistance is 1 kΩ.

photoelectron spectroscopy (ARPES) [281], polarized neutron scattering [282, 283, 284], Nernst measurements [270, 285], and magneto-optical measurements [286, 287, 288]. As for the iron-based superconductors, there is less evidence about the spontaneous breaking of TRS. Grinenko *et. al.* reported the observation of an enhanced zero-field muon spin-relaxation rate below the superconducting transition temperature in the ion-irradiated $Ba_{0.27}K_{0.73}Fe_2As_2$ single crystals [289]. There is no experimental evidence of TRS breaking in the bulk of intrinsic Fe-base superconductors. In $Fe_{1+y}Te_{1-x}Se_x$, the excess Fe randomly occupies the Fe(2) site between the square planar sheets of Fe [290, 291]. The interstitial iron impurity could locally break the TRS by introducing a local magnetic moment [292]. Although the Nernst effect is generally taken as a bulk transport measurement probe, it often reflects the fluctuations in the local scale (A good example is the superconducting fluctuation in the cuprates [185, 182, 293, 294, 295]). The Nernst signal only measures the local thermoelectric properties across each channel, which is consistent with the fluctuation of the spontaneous Nernst signal observed among different Nernst channels in the same $Fe_{1+y}Te_{1-x}Se_x$ sample (as shown in Figure 5.3). We believe the difference

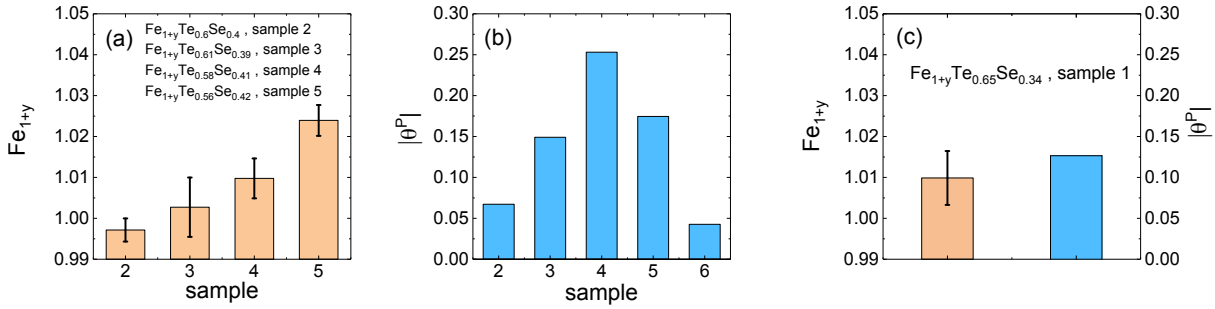

Figure 5.7: (a) Fe concentration in $Fe_{1+y}Te_{1-x}Se_x$ Sample 2, 3, 4, and 5. Error bars plot the standard deviation of Fe concentration on different sample spots. (b) The averaged peak values of the zero-field spontaneous Peltier Hall signal $|\theta^P|$, defined as the ratio of $|\alpha_{xy}|$ and α_{xx}, in Sample 6, 2, 3, 4, and 5, in the order that the nominal Fe concentration increases. As a comparison, Iron concentration and $|\theta^P|$ in Sample 1 are also plotted in (c). Sample 2, 3, 4, and 5 has a lower Te concentration compared to Sample 1.

in different Nernst channels is exactly caused by the uneven distribution of iron impurities across the sample. The iron impurity is not evenly distributed across the whole sample, which is observed in our EDX measurement. The most reasonable interpretation of why we see almost absent spontaneous Nernst signals on some channels in part of our $Fe_{1+y}Te_{1-x}Se_x$ samples is that the spin-up and spin-down moments on excess iron sites are almost compensated locally at the positions of these channels.

To understand how the amount of excess Fe could affect the zero-field Nernst signal, we measured the Nernst effect in a series of $Fe_{1+y}Te_{1-x}Se_x$ samples with different Fe concentration. In these $Fe_{1+y}Te_{1-x}Se_x$ single crystals, the atomic concentration is determined by the EDX measurement with a Cameca SX100 Electron Probe Micro Analyzer. For each sample, we select 15 spots on the sample to do EDX measurement and get the averaged element concentration. The averaged Fe concentrations in four different samples (Sample 2, 3, 4, and 5) are plotted in Figure 5.7 (a). Figure 5.8 to 5.12 plot the field-dependent thermoelectric data for $Fe_{1+y}Te_{1-x}Se_x$ Sample 2 to Sample 6.

We also measured the Hall signal in $Fe_{1+y}Te_{0.65}Se_{0.34}$ Sample 1 up to 14 T at the temperature where the spontaneous Nernst signal is the largest. Figure 5.13 shows the Hall resistivity ρ_{xy} measured during field sweep up and sweep down. The inset of Figure 5.13 shows the magnetoresistivity ρ_{xx} measured at the same temperature. At 14 T, $\frac{\rho_{xy}}{\rho_{xx}} < 0.01$, which means the Hall angle $\theta < 0.57°$. The Hall signal is very small compared to the resistivity within the temperature range where shows spontaneous Nernst signal. So the Hall angle θ can be neglected when calculate the Peltier Hall angle θ^P. With the Nernst

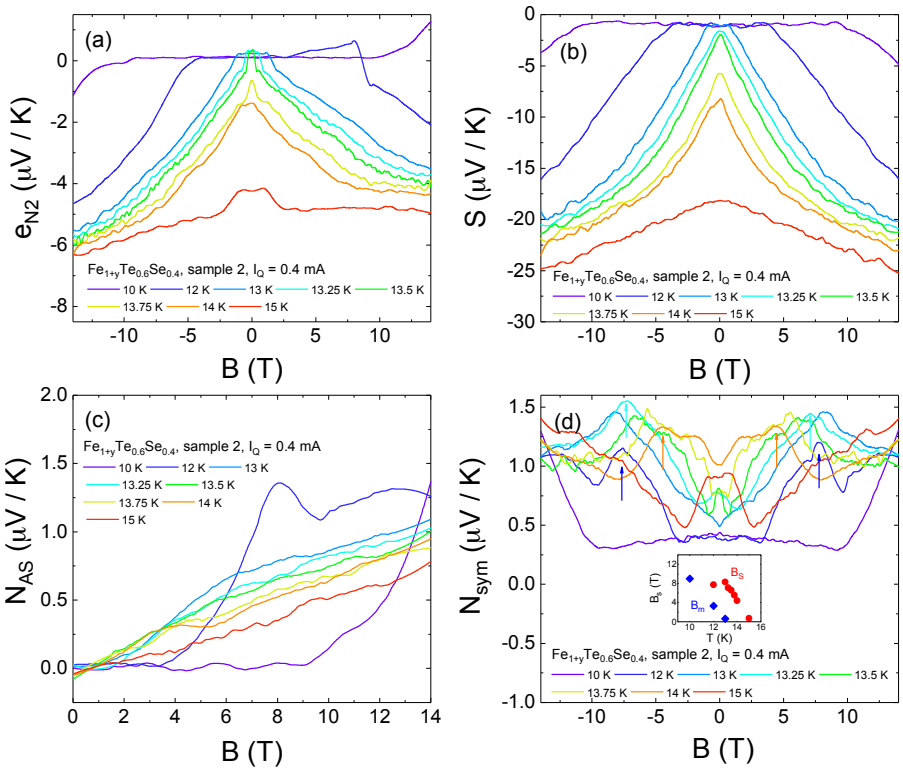

Figure 5.8: Observed (a) Nernst signal e_{N2} and (b) Seebeck signal vs. magnetic field B at selected T from 10 K to 15 K in Sample 2. (c) Ordinary Nernst signal N_{AS} of Sample 2 following the standard B-antisymmetrization to curves in Panel (a). (d) Magnetic field dependence of the intrinsic field-symmetrized Nernst signal. Arrows indicate the location of the shoulder trend B_S. The Seebeck pickup has been subtracted. Inset shows the temperature dependence of B_S, compared with the melting fields B_m. As expected for the characteristic field scales in superconductors, both fields converge to zero as the T increases towards T_c. The heater resistance is 1 kΩ.

signal e_y and Seebeck coefficient, we can get

$$e_N = S(\alpha_{xy}/\alpha - \sigma_{xy}/\sigma) = S(\tan\theta^P - \tan\theta) \approx S\tan\theta^P \tag{5.3}$$

$$\tan\theta^P = \alpha_{xy}/\alpha \approx e_y/S \tag{5.4}$$

in which σ_{xy} is the Hall conductivity, e_N is the Nernst signal, and α is the 2D Peltier conductivity tensor. . The averaged peak values of the zero-field spontaneous Peltier Hall signal $|\theta^P|$ is defined as the ratio of $|\alpha_{xy}|$ and α_{xx} [188], in which α is the two dimensional Peltier conductivity tensor. The Peltier Hall signal $|\theta^P|$ in Sample 2 to Sample 6 is plotted in Figure 5.7 (b), which shows a non-monotonic dependence on the Fe concentration. Sample 6 has nominally no excess Fe and the smallest $|\theta^P|$. As the Fe concentration increases, $|\theta^P|$ is first enhanced and then suppressed. The Fe concentration and $|\theta^P|$ measured in Sample

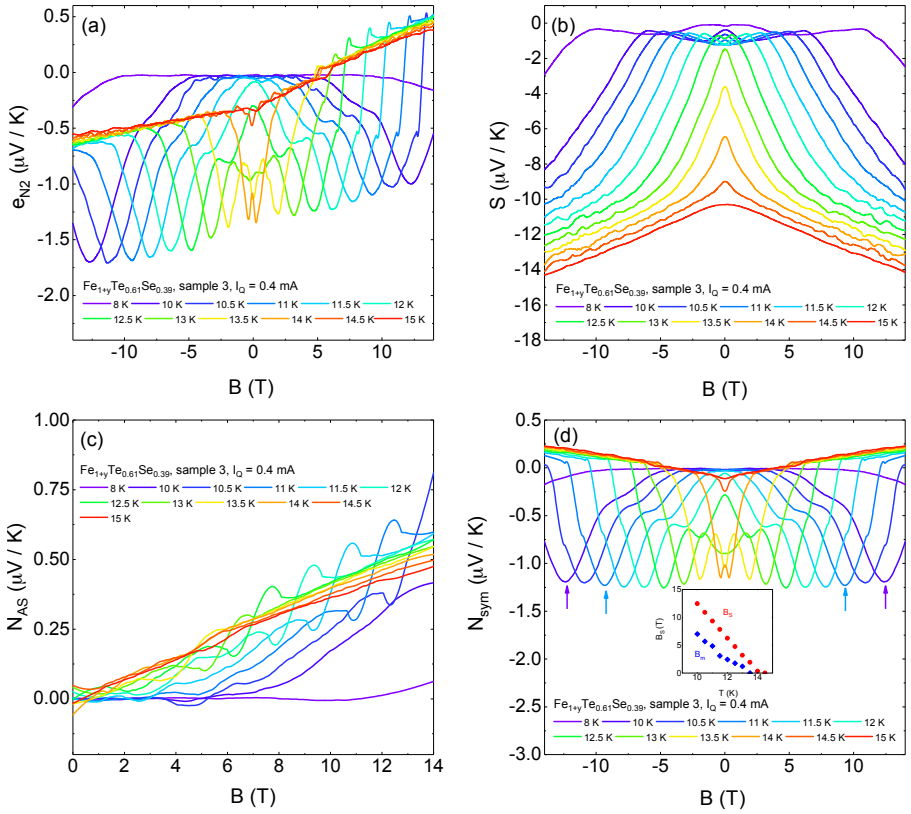

Figure 5.9: Observed (a) Nernst signal e_{N2} and (b) Seebeck signal vs. magnetic field B at selected T from 8 K to 15 K in Sample 3. (c) Ordinary Nernst signal N_{AS} of Sample 3 following the standard B-antisymmetrization to curves in Panel (a). (d) Magnetic field dependence of the intrinsic field-symmetrized Nernst signal. Arrows indicate the location of the shoulder trend B_S. The Seebeck pickup has been subtracted. Inset shows the temperature dependence of B_S, compared with the melting fields B_m. As expected for the characteristic field scales in superconductors, both fields converge to zero as the T increases towards T_c. The heater resistance is 1 kΩ.

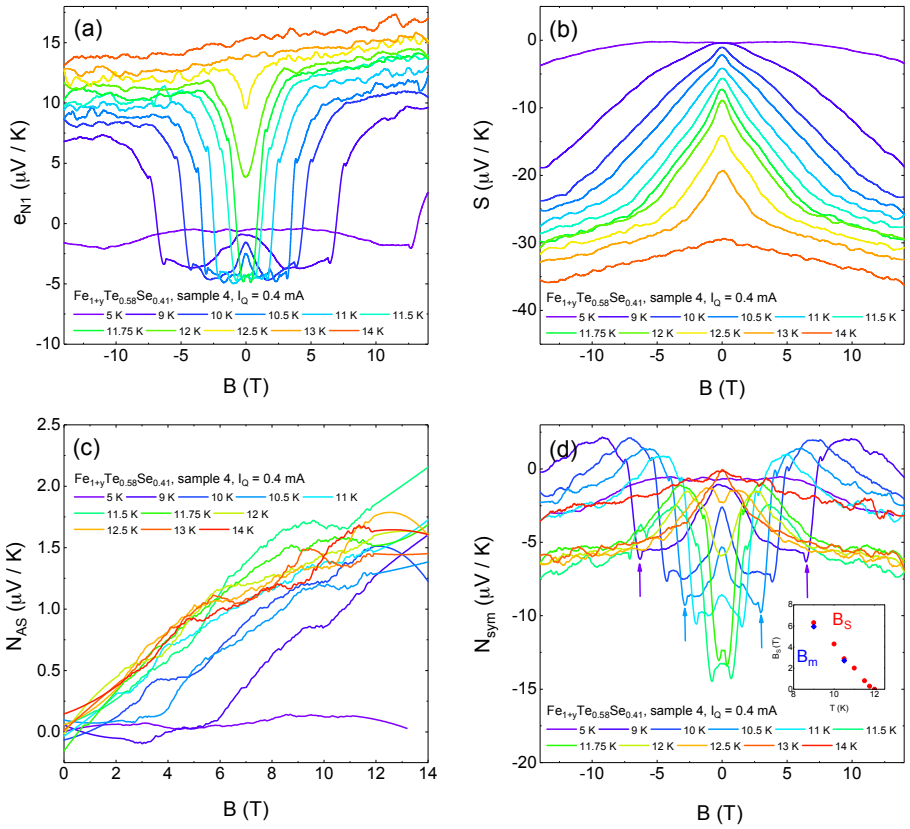

Figure 5.10: Observed (a) Nernst signal e_{N1} and (b) Seebeck signal vs. magnetic field B at selected T from 5 K to 14 K in Sample 4. (c) Ordinary Nernst signal N_{AS} of Sample 4 following the standard B-antisymmetrization to curves in Panel (a). (d) Magnetic field dependence of the intrinsic field-symmetrized Nernst signal. Arrows indicate the location of the shoulder trend B_S. The Seebeck pickup has been subtracted. Inset shows the temperature dependence of B_S, compared with the melting fields B_m. As expected for the characteristic field scales in superconductors, both fields converge to zero as the T increases towards T_c. The heater resistance is 1 kΩ.

1 are plotted in Figure 5.7 (c) as a comparison.

5.4 Discussion

This spontaneous Nernst signal is only non-zero inside the vortex liquid regime. A similar anomalous Nernst effect has been reported in the striped cuprate superconductor $La_{2-x}Ba_xCuO_4$ by Li *et. al.* [270]. In these quasi-2D superconductors, thermally driven vortices are generated in equilibrium at $B = 0$ above the Berenzinski-Kosterlitz-Thouless (BKT) transition. Instead of having the same number of vortices and anti-vortices, a predominant sign of vortex is energetically favorable due to the relieve of interlayer phase frustration [296]. In

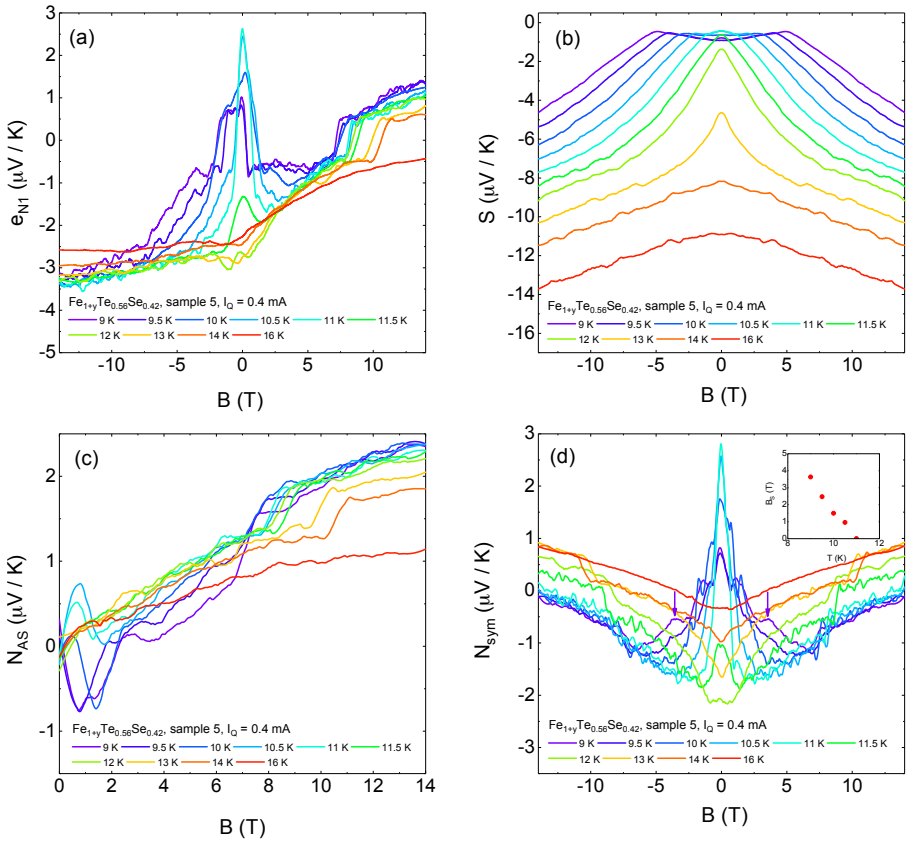

Figure 5.11: Observed (a) Nernst signal e_{N1} and (b) Seebeck signal vs. magnetic field B at selected T from 9 K to 16 K in Sample 5. (c) Ordinary Nernst signal N_{AS} of Sample 5 following the standard B-antisymmetrization to curves in Panel (a). (d) Magnetic field dependence of the intrinsic field-symmetrized Nernst signal. Arrows indicate the location of the shoulder trend B_S. The Seebeck pickup has been subtracted. Inset shows the temperature dependence of B_S, compared with the melting fields B_m. As expected for the characteristic field scales in superconductors, both fields converge to zero as the T increases towards T_c. The heater resistance is 1 kΩ.

$La_{2-x}Ba_xCuO_4$, the strong superconducting fluctuation extends from the charge-ordering temperature down to 5 K enables the vortices (with the predominant sign) to move freely in a temperature gradient and generate the spontaneous Nernst signal [297, 298]. The existence of the thermal-driven vortices have also been generally reported in Fe-based superconductors [299, 271, 183]. We note that $Fe_{1+y}Te_{1-x}Se_x$ is more towards a 3D superconductor due to a weaker anisotropy [300]. Nonetheless, a theoretical study points out the existence of vortex liquid state in a three-dimensional type-II superconductor with strong thermal fluctuations [301]. As a result, for 3D anisotropic superconductors, such as $Fe_{1+y}Te_{1-x}Se_x$, there is still a narrow region between the superconducting critical temperature and the mean-field transition temperature where spontaneously created vortex lines

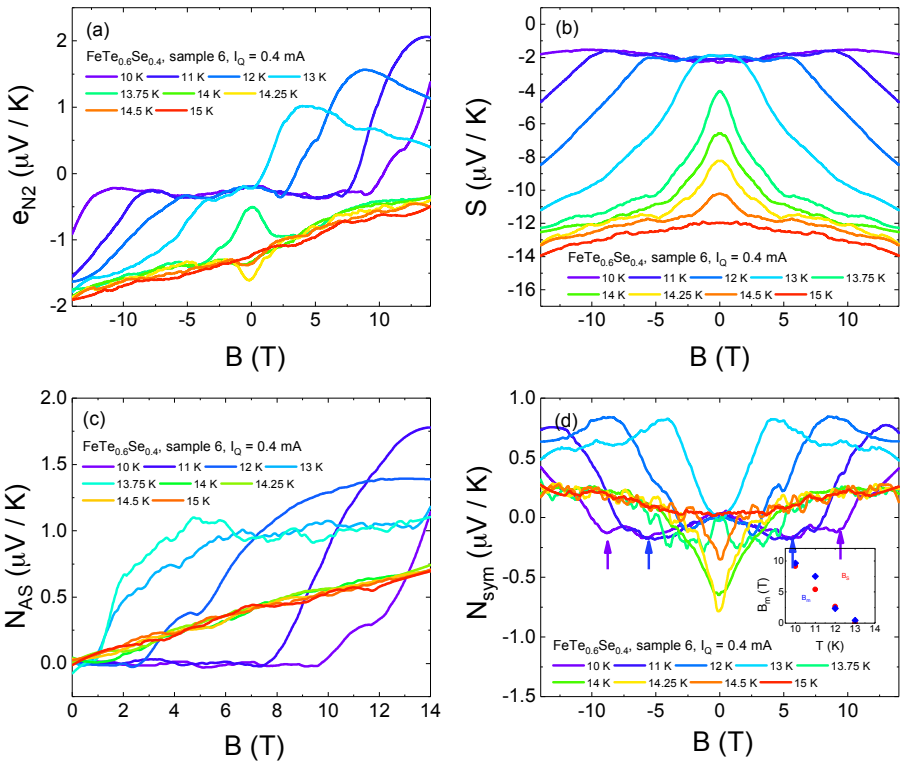

Figure 5.12: Observed (a) Nernst signal e_{N2} and (b) Seebeck signal vs. magnetic field B at selected T from 10 K to 15 K in Sample 6. (c) Ordinary Nernst signal N_{AS} of Sample 6 following the standard B-antisymmetrization to curves in Panel (a). (d) Magnetic field dependence of the intrinsic field-symmetrized Nernst signal. Arrows indicate the location of the shoulder trend B_S. The Seebeck pickup has been subtracted. Inset shows the temperature dependence of B_S, compared with the melting fields B_m. As expected for the characteristic field scales in superconductors, both fields converge to zero as the T increases towards T_c. The heater resistance is 1 kΩ.

exist [302]. This is consistent with the temperature span of a few Kelvin of the spontaneous Nernst signal observed in Figure 5.2 (c) and (d).

After having spontaneously generated vortex-antivortex pairs, the next question is what provides the non-zero net vortex in the vortex liquid state of $Fe_{1+y}Te_{1-x}Se_x$? Recently, Jiang $et.\ al.$ points out that in an s-wave superconductor with strong spin-orbit coupling, the magnetic impurity ions can generate topological vortices without applying a magnetic field [139]. The quantum anomalous vortices produced by the interstitial magnetic Fe are pinned at the magnetic ion, which means they can not move freely or provide the non-zero Nernst signal at zero-field directly. The pinned quantum anomalous vortices could possibly break the balance between thermally-created vortices and anti-vortices. Although we need further theoretical evidence to support this assumption, experimentally we find the spontaneous Nernst effect signals need both bulk superconductivity and excess Fe.

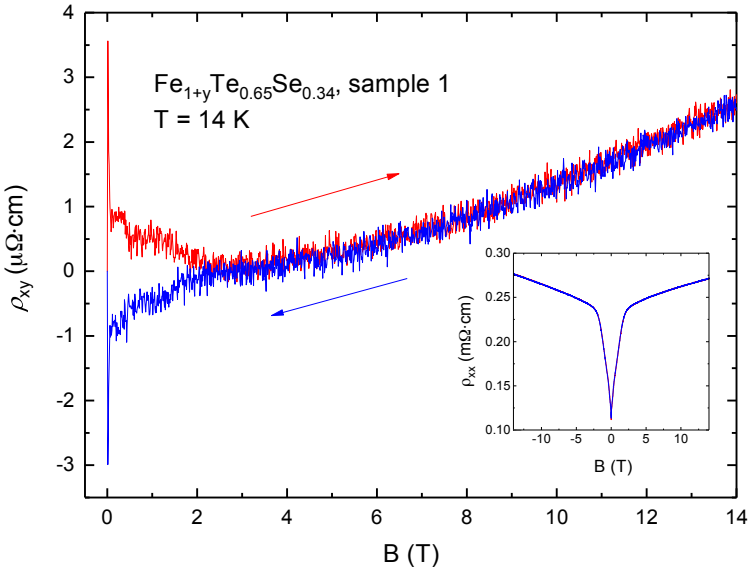

Figure 5.13: The Hall resistivity ρ_{xy} measured at 14 K in $Fe_{1+y}Te_{0.65}Se_{0.34}$ Sample 1. The inset shows the magnetoresistivity ρ_{xx} measured at the same temperature. Red curve represents the field sweep up while blue curve represents the sweep down.

This point is supported by the smallest signal amplitude of Sample 6, the sample with the lowest excess Fe level (Figure 5.7 (b)). This point is further supported by the observation that the spontaneous Nernst signal is strongly suppressed in Sample 5 (as shown in Figure 5.7 (b)), which has a less than 2% superconducting volume (as seen in Table 5.1). This could be evidence that bulk superconductivity is indispensable in producing the spontaneous Nernst signal. As shown by a previous study, the as-grown $Fe_{1+y}Te_{1-x}Se_x$ single crystals hold filamentary superconductivity due to the extra Fe, most of the bulk nature of the superconductivity can only be achieved by oxygen annealing [303].

We also measured the Nernst signal with different cooling process in $Fe_{1+y}Te_{1-x}Se_x$ Sample 4. The local magnetic moments introduced by impurity ions are pinned randomly in the sample, which means the Ising-like magnetic moment could either point up or down in the zero-field-cooling process. We tried to change the magnetic moment direction of interstitial Fe by warming up the sample to 350 K and do a field-cooling in both B = 14 T and -14 T, then swept the field between 14 T and -14 T at several temperatures where the unusual Nernst signal is most prominent (as shown in Figure 5.14 (d)). We also did a T sweep below 20 K to check the zero-field Nernst signal (as shown in Figure 5.14 (b) and (c)). The results show that the field-cooling process can't alter the sign or the magnitude of the spontaneous Nernst signal. One possibility is 350 K is not high enough to overcome the large out-of-plane magnetic anisotropy energy or alter the magnetic moment direction.

To further study whether this spontaneous Nernst signal could only happen in mate-

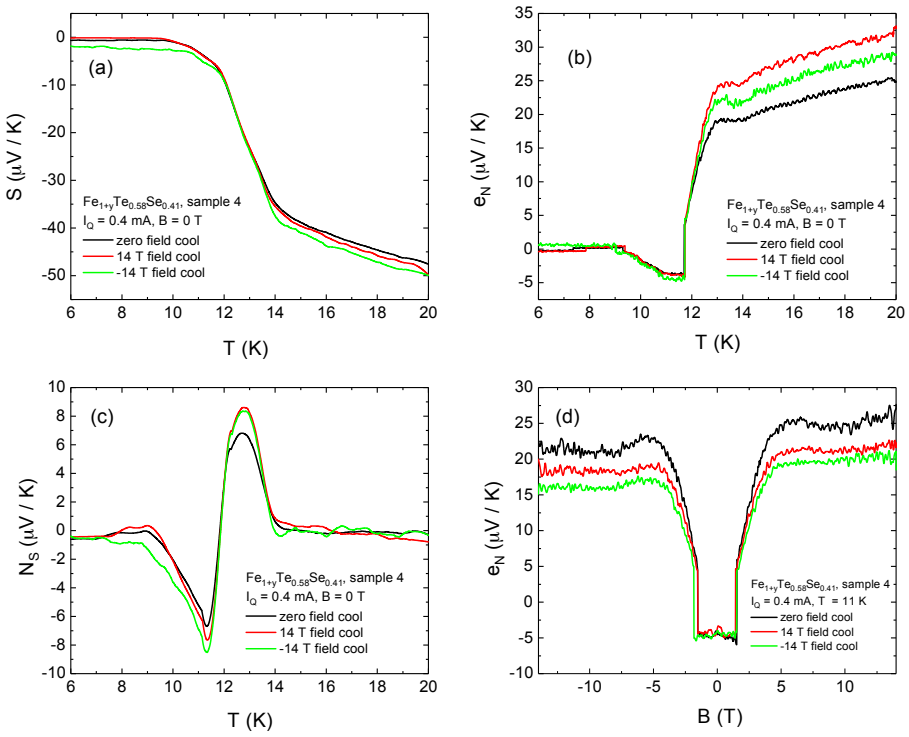

Figure 5.14: The Seebeck and Nernst signal measured with different cooling process in $Fe_{1+y}Te_{1-x}Se_x$ Sample 4. Temperature T dependence of the (a) thermopower S (Seebeck signal) and (b) the observed Nernst signal e_N in Sample 4. (c) The intrinsic spontaneous Nernst signal is extracted by subtracting the scaled thermopower signal $N_S(T) = e_N(T) - k \cdot S(T)$. (d) Observed Nernst signal e_N vs. magnetic field B at 11 K in Sample 4. Black curves are taken with zero-field-cool process. Red curves are taken with a 14T-field-cool process. Green curves are taken with a -14 T-field-cool process. The field was applied at 350 K.

rials that hold non-trivial topological band structure, we conduct the same thermoelectric measurements in FeSe single crystals which have similar properties as $Fe_{1+y}Te_{1-x}Se_x$ but a topologically trivial band structure [304]. Figure 5.15 plot the complete data set for FeSe Sample 1. The FeSe single crystal being measured here has a dimension of $2.5 \times 1 \times 0.175$ mm^3 and a superconducting transition temperature of $T_c \sim 8.3$ K. Figure 5.15 (a) shows two Nernst channels only have pickup from the Seebeck signal. There is no obvious zero-field Nernst signal across the superconducting transition. Figure 5.15 (b) plots the field dependent Nernst signal e_{N3}, which is dominated by the antisymmetric ordinary Nernst signal. The ordinary Nernst signal N_{AS} of FeSe Sample 1 following the standard B-antisymmetrization to curves in panel (b) is shown in Figure 5.15 (d), which is about 2 times the value obtained in reference [305]. The field-dependent Nernst signal shows a monotonic dependence on the magnetic field, which contradicts to what has been observed in the $Fe_{1+y}Te_{1-x}Se_x$ samples. There is experimental evidence that shows the interstitial

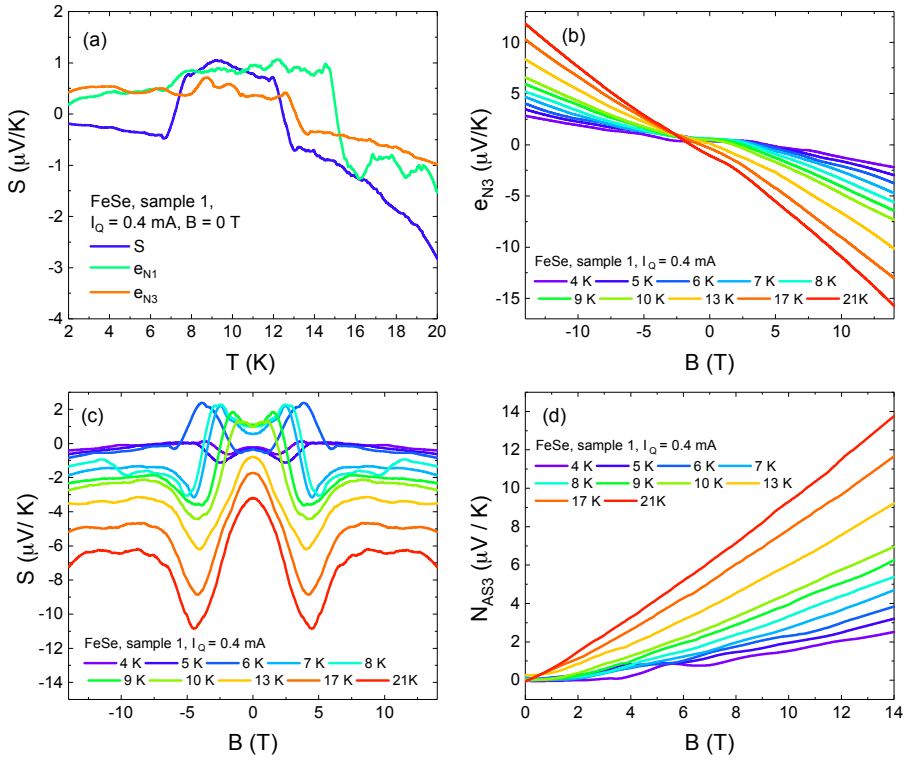

Figure 5.15: (a) Observed Nernst signal e_{N1}, e_{N3} and Seebeck signal S vs. T at $B = 0$ T for FeSe Sample 1. Observed (b) Nernst signal e_{N3} and (c) Seebeck signal S vs. magnetic field B at selected T from 4 K to 21 K in FeSe Sample 1. (d) Ordinary Nernst signal N_{AS} of FeSe Sample 1 following the standard B-antisymmetrization to curves in Panel (b). The heater resistance is 1 kΩ.

Fe(2) site is unoccupied in clean FeSe single crystals [306]. The absence of the spontaneous Nernst effect in FeSe is most likely due to the unoccupation of the interstitial Fe(2) site in FeSe single crystals. But we could not rule out the possibility that a topologically non-trivial band structure also plays a role in inducing a spontaneous Nernst effect in $Fe_{1+y}Te_{1-x}Se_x$.

At this point, it's necessary to clarify that the zero-field spontaneous Nernst signal doesn't come from the disorder or inhomogeneity of the sample. Our $Fe_{1+y}Te_{1-x}Se_x$ and FeSe sample have similar superconducting transition width, which means they have similar disorder levels. But FeSe sample doesn't show the zero-field spontaneous Nernst signal, which indicates this signal doesn't simply come from the disorder or inhomogeneity of the sample. Further more, the inhomogeneity and nanoscale electronic disorder in the high-T_c superconductors has been observed in many cuprates [307, 308, 309]. This electronic inhomogeneity is commonly attributed to a disorder introduced by the poorly screened electrostatic potential of the out-of-plane oxygen dopant atoms [310, 311], although the

electronic inhomogeneity is also argued to be intrinsic to the competing orders. But this electronic inhomogeneity does not generally induce a spontaneous Nernst signal in the vortex liquid states of these cuprates, with the only exception of the 1/8-doped striped-phased LBCO [270]. Obviously, the spontaneous Nernst signal does not result simply from the inhomogeneity in a vortex liquid. It must be related to some intrinsic properties of the material $Fe_{1+y}Te_{1-x}Se_x$. The spontaneous Nernst signal doesn't come from the misalignment of the Nernst channel contacts either since our $Fe_{1+y}Te_{1-x}Se_x$ and FeSe samples have similar contact misalignment conditions and FeSe sample doesn't show the spontaneous Nernst signal.

The zero-field spontaneous Nernst signal doesn't come from the pickup of an anisotropic Seebeck signal, either. Indeed, whether the thermopower is isotropic or not could be decided by heat current direction. With a well defined sample geometry, the heat should transfer uniformly inside the sample. At such a low temperature range ($T < 20$ K), the heat transport is mainly conducted by phonons, which means crystal structure decides the heat flow anisotropy in the sample. The crystal structure doesn't change when the sample crosses the superconducting transition. Further more, Fe(Te,Se) has a tetragonal structure while FeSe has an orthogonal structure at this temperature range. When we apply the heat current in-plane in the FeSe sample, it could have a more anisotropic thermopower signal. But we couldn't observe the zero-field Nernst signal in FeSe even with the same data analysis method, which indicates this zero-field Nernst signal may not purely come from the pickup of an anisotropic Seebeck signal.

The homogeneity of the temperature gradient in our sample is also checkup with the thermal Hall measurements. The experimental setup is shown in Figure 5.16. Our analysis assumes that the temperature gradient in our sample is homogenous. A horizontal thermal gradient component may induce a horizontal voltage that looks as if a Nernst effect signal. To check if this horizontal thermal gradient exists, we carried out the thermal Hall measurement in $Fe_{1+y}Te_{1-x}Se_x$ sample 1 at $B = 1$ T and $B = 4$ T. The data is shown in Figure 5.17. At both 1 T and 4 T, the thermal Hall signal is around zero with a finite noise level. Our experiment shows that no thermal Hall signal has been observed at either zero field or finite field. So we believe there is no large transverse thermal gradient component built up in the samples at zero magnetic field, which indicates a homogenous thermal gradient across the sample. We note that a spontaneous thermal Hall effect is highly unusual and has only been reported in very few materials, such as the chiral antiferromagnet Mn_3Sn [312].

In order to further verify that the spontaneous Nernst signal is not simply coming from the pickup of inhomogeneous Seebeck signals, we measure three pairs of Seebeck channels in $Fe_{1+y}Te_{1-x}Se_x$ Sample 1. The experimental configuration is shown in Figure 5.18 (a).

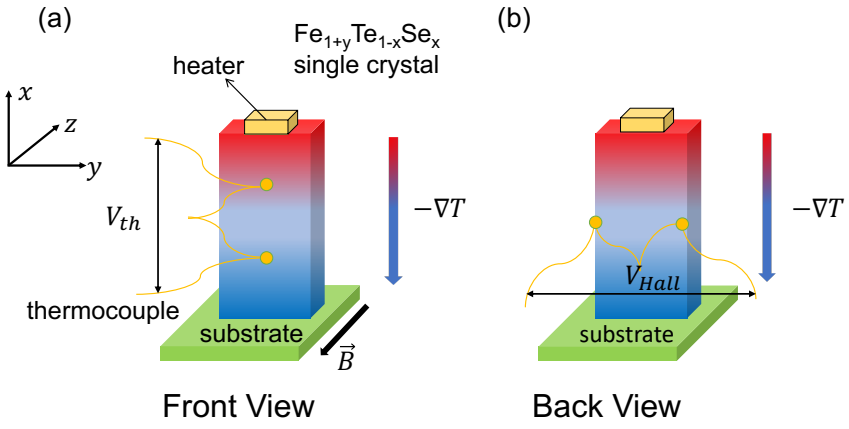

Figure 5.16: (a) Front view and (b) back view of the thermal Hall measurement setup. A heat current Q is sent in the ab plane of the $Fe_{1+y}Te_{1-x}Se_x$ sample 1 along the x direction. Two type-E thermocouples are mounted vertically on the frontside of the sample to measure the temperature gradient along the x direction. The other two type-E thermocouples are mounted horizontally on the backside of the sample to measure the temperature gradient along the y direction. The magnetic field B is applied along the z direction.

The Seebeck channels measured here are S_1 and S_1', S_2 and S_2', S_3 and S_3'. Each pair of them are measured simultaneously. In order to align the contacts of corresponding Seebeck channels well, the contacts are remade with silver epoxy. The distance between contacts V_{1A} and V_{2A} is 0.9 mm, which is the same as the distance between contacts V_{1A}' and V_{2A}'. The distance between contacts V_{2A} and V_{3A} is 0.875 mm, which is a little bit shorter than the distance between contacts V_{2A}' and V_{3A}' (0.9 mm).

Figure 5.18 (b), (c) and (d) show the experimental results. Panel (b) is the measured Seebeck coefficients S vs T of channel S_1 and S_1'. S_1' vs. T overlaps with S_1 vs. T after multiplying by a factor of 0.94. The scaling factor between Seebeck channels S_2 and S_2', S_3 and S_3' are 0.84 and 0.87. The difference between S_x and S_x' is within the error bar brought by the size of the electrical contacts and the slight misalignment of the contacts. Take S_1 and S_1' as an example, the electrical contacts are made by silver epoxy and has a diameter of 0.1 mm. Compared to the distance between the two contacts, which is 0.9 mm, it can bring an error of -10% to +12.5% to the Seebeck coefficient.

If we define T_c to be the temperature where the Seebeck signal changes from nearly zero to a finite value, we can see that Seebeck channels S_x and S_x' resolve exactly the same T_c. Therefore, two edges of our sample don't have large inhomogeneity, which can bring different T_c for Seebeck channels S_x and S_x''. But the T_c for S_1, S_2 and S_3 are 13.9 K, 13.4 K and 13.5 K, which are different. This is due to the temperature gradient that built up

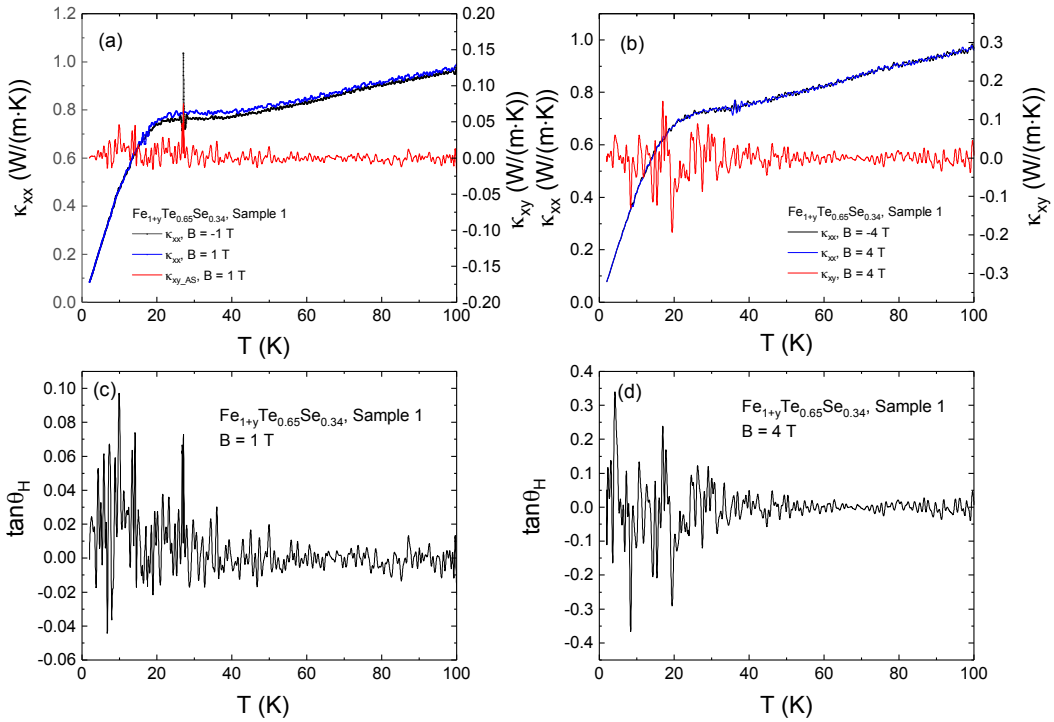

Figure 5.17: Thermal conductivity κ_{xx} and thermal Hall conductivity κ_{xy} measured in $Fe_{1+y}Te_{0.65}Se_{0.34}$ Sample 1 at (a) B = 1 T and (b) B = 4 T. The thermal Hall angle θ_H is extracted from the ratio of the thermal Hall conductivity and thermal conductivity with $\tan\theta_H = \frac{\kappa_{xy}}{\kappa_{xx}}$.

along the sample. The actual temperature differs for about 0.5 K between the hot and cold end of the sample.

Furthermore, the difference between Seebeck channels S_x and S_x' has a monotonic dependence with temperature which increases from a near-zero value to a finite value when enters the normal state. In contrast, the zero-field Nernst signal shows a non-monotonic dependence with temperature (such as Panel (c) of Figure 5.2), which can not come from the contribution of a monotonic Seebeck pickup.

Besides, we also measured the Nernst signal in $Fe_{1+y}Te_{1-x}Se_x$ Sample 1 after remaking the contacts. Sample 1 still shows a spontaneous Nernst signal at $B = 0$ T (as shown in Figure 5.18 (e) and (f)). The magnitude of the spontaneous Nernst signal e_N is comparable to the result in Panel (c) of Figure 5.2, which is taken before remaking the contacts. We note that the temperature dependence of the e_N is different from what is measured with the original contacts. We suspect that is due to the inhomogeneity of the Fe impurities in the sample. Similar patterns are observed in other samples, like those in Figure 5.14 (c).

In conclusion, the measured Seebeck coefficients verify the homogeneity of our sample. As a result, the zero-field Nernst signal is not simply due to the pickup of inhomoge-

neous Seebeck signal and is intrinsic to the $Fe_{1+y}Te_{1-x}Se_x$ samples.

5.5 Conclusion

To conclude, we study the Nernst effect in Fe-based superconductor $Fe_{1+y}Te_{1-x}Se_x$ and find a filed-symmetric Nernst signal which is non-zero as $B \to 0$ and only appears in the superconducting state. Our experiment provides the first evidence of a locally broken TRS in the bulk of a topologically non-trivial superconductor. The spontaneous Nernst signal varies in different Nernst channels and the overall strength is sensitive to the concentration of excess Fe, suggesting its relevance to the TRS-breaking local moments on these interstitial Fe sites. Our results also indicate an unconventional vortex contribution and provide indirect evidence of the existence of QAVs, although more theoretical explanation is needed to illustrate the underlying mechanism.

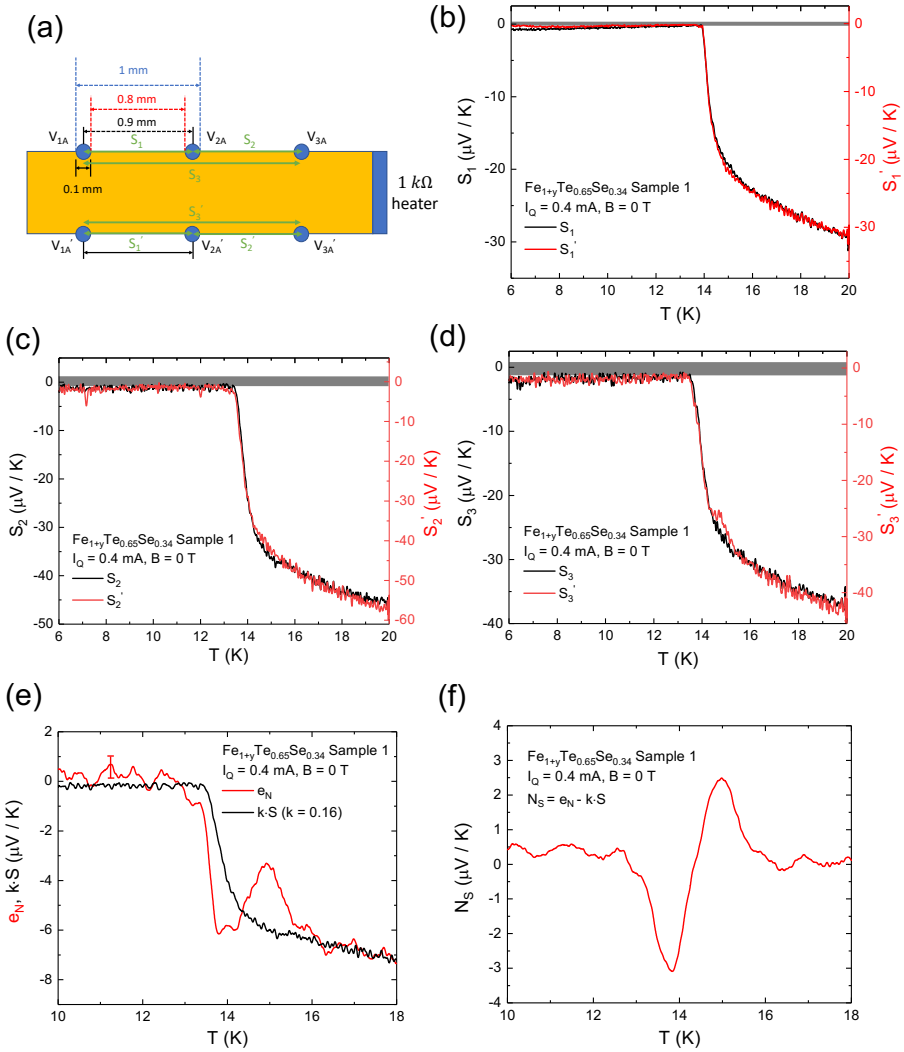

Figure 5.18: (a) Experimental configuration of $Fe_{1+y}Te_{1-x}Se_x$ Sample 1, which is the same as the $Fe_{1+y}Te_{1-x}Se_x$ Sample 1 configuration in the main text. Six contacts were remade to make sure they are well aligned. S_x and $S_{x'}$ are two Seebeck channels being measured simultaneously. Blue solid circles are electrical contacts. Dashed lines and arrows label the distance between the contacts. (b), (c) and (d) are measured Seebeck coefficients for three pairs of Seebeck channels. The Seebeck coefficients of channel $S_1^{'}$ overlaps with channel S_1 after multiplying by a factor of 0.94. The scaling factor between Seebeck channels S_2 and $S_2^{'}$, S_3 and $S_3^{'}$ are 0.84 and 0.87. Gray solid lines mark $S = 0$ with their widths indicate the error bar of the Seebeck coefficient. The heater resistance is 1 kΩ. The heater current is 0.4 mA. (e) Temperature dependence of the thermopower $k \cdot S$ (Seebeck signal) and the observed Nernst signal e_N in Sample 1. The thermopower signal S was scaled by a factor $k = 0.16$ to match the T-dependence of S and e_N. (f) The intrinsic spontaneous Nernst signals N_S vs. T in Sample 1, which is extracted by subtracting the scaled thermopower signal $N_S(T) = e_N(T) - k \cdot S(T)$.

CHAPTER 6

Conclusions and Outlook

6.1 Summary

Motivated by the interesting phenomena that have been discovered in quantum materials, we developed a new experimental technique to measure the electronic and magnetic properties of different types of materials. Multiple thermal transport, thermoelectric and thermodynamic studies are conducted in transition metal oxides and topological superconductors to reveal their novel properties across different types of phase transitions, such as the metal-insulator transition, magnetic phase transition and superconducting transition.

We developed a highly sensitive torque differential magnetometry using the qPlus mode of a quartz tuning fork. We observe a sharp resonance of the quartz tuning fork with a Q factor of 10^4 at low temperatures down to 20 mK. Two different circuits for low and high field measurements maintain high sensitivity in both conditions. We calibrate our torque differential magnetometry by measuring the angular dependence of the hysteresis loop in ferromagnetic single-crystal $Fe_{0.25}TaS_2$. The hysteresis loop measurement in the ferromagnetic $Fe_{0.25}TaS_2$ single crystal proves that QTF can achieve a sensitivity of magnetic moment measurement at around 10^{-7} emu, which is comparable to other state-of-the-art magnetometers. Furthermore, we demonstrate the high sensitivity of the torque differential magnetometry by measuring the quantum oscillations of a bismuth single crystal. To use the tuning fork magnetometry in a wet cryogenic system, we also make vacuum cells for the tuning forks which could hold a high vacuum at liquid Helium temperature. We also demonstrate the application of tuning fork magnetometry in a pulsed magnetic field up to 65 T by measuring the hysteresis loop and melting field of underdoped high-temperature superconductors $YBa_2Cu_3O_y$. All of these measurements demonstrate that our qPlus QTF magnetometry is a reliable method for conducting torque differential magnetometry measurements, especially at cryogenic temperatures and intense magnetic fields.

We conduct thermal transport study in two strongly correlated materials, vanadium

dioxides (VO_2) and $SmBaMn_2O_6$. We investigate the thermal conductivity across the phases transitions in VO_2 and $SmBaMn_2O_6$ single crystals by performing the thermal transport measurement with an extremely slow sweeping speed of temperature. A narrow thermal conductivity peak is revealed within the first-order metal-insulator transition in VO_2 single crystals. The thermal conductivity peak doesn't show obvious dependence on the magnetic field, which indicates that the strong enhancement of the thermal conductivity could possibly due to the softening of certain phonon modes at the phase transition. In $SmBaMn_2O_6$ single crystals, both electrical resistance and magnetic susceptibility show abrupt change accompanied by a narrow hysteresis loop at $T_{co1} \sim 362$ K. Upon further cooling down, another anomaly takes place between 150 K and 210 K (around T_{co2}) which is manifested by a much broader hysteresis loop. The total thermal conductivity is enhanced by 3$\sim$4 times within the MIT at T_{co1}, while no obvious peak is observed around T_{co2}. The enhancement of thermal conductivity within the structural transition at T_{co1} is likely due to the phonon softening. Around T_N, the spin-phonon coupling in this material strongly modifies the phonon spectra and prevent the evolution of soft-phonon modes. The hardening of soft-phonon modes around T_N may explain the absence of thermal conductivity peak around T_{co2}, which lies right above T_N. The results in $SmBaMn_2O_6$ single crystals further prove that the thermal conductivity peak across a structural phase transition could possibly come from the soft-phonon contributions. These experiments provide a new idea to solve the thermal management issues in solid-state materials and could also bring potential applications in electronic devices.

To reveal the superconducting gap structure of a topological superconductor candidate, we conduct the heat capacity measurement in the Nb-doped Bi_2Se_3 single crystals. For all samples, the heat capacity shows an exponential decay when T approaches zero, which indicates a nodeless superconducting gap structure. Both the nematic order observed in the torque magnetometry measurement and the nodeless gap structure obtained by the heat capacity measurement indicate an odd parity topological superconductor.

We also present a study of the Nernst effect in an iron-based superconductor with a non-trivial band topology $Fe_{1+y}Te_{1-x}Se_x$. We find a filed-symmetric Nernst signal which is non-zero as $B \rightarrow 0$ and only appears in the superconducting state. Our experiment provides the first evidence of a locally broken TRS in the bulk of a topologically non-trivial superconductor. The spontaneous Nernst signal varies in different Nernst channels and the overall strength is sensitive to the concentration of excess Fe, suggesting its relevance to the TRS-breaking local moments on these interstitial Fe sites. Our results also indicate an unconventional vortex contribution and provide indirect evidence of the existence of QAVs, although more theoretical explanation is needed to illustrate the underlying mechanism.

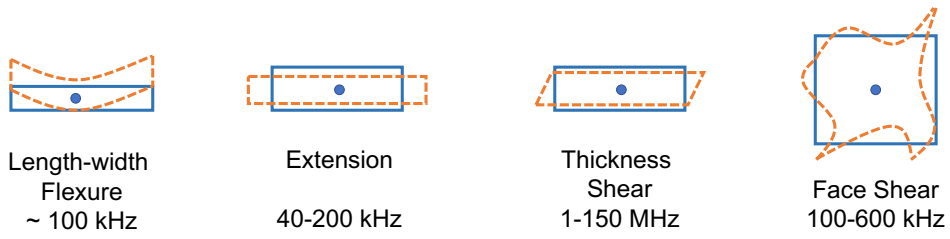

Figure 6.1: Basic modes of vibration and their typical resonance frequencies of quartz crystals.

6.2 Future Work

6.2.1 Magnetometer with Quartz Crystals Working at Megahertz (MHz) Range

Our experiments in the DC magnetic field have proved that the qPlus QTF magnetometry is a reliable method for conducting torque differential magnetometry measurements in many different types of materials. But we failed to reveal the quantum oscillation signals in bismuth single crystals in a pulsed magnetic field. One possible reason is the responding speed of the QTF is not enough to reveal a fast oscillating signal. For a short magnetic pulse up to 10 T, the total rising-up time is 8 ms. There are roughly 7 to 8 periods of quantum oscillation signals within this period of time, which means each period only has a time span of around 1 ms. Qualitatively speaking, the responding time t of a QTF is proportionally related to its quality factor Q but inversely proportional to its resonance frequency ω_0, which can be expressed as the following simple form.

$$t \sim \frac{Q}{\omega_0} \tag{6.1}$$

A larger Q factor indicates the QTF needs a longer time to be damped. A lower resonance frequency means it needs longer time to finish one oscillation period, which also indicates a longer time to reflect the change it has detected. In order to have a fast enough responding speed, the responding time needs to be shortened. Therefore, we need a QTF with a higher resonance frequency. As has been introduced in Chapter 2.1.3, we use QTFs with a resonance frequency of 192 kHz in the pulsed field. In order to increase the responding speed by an order of magnitude, we have to turn to the quartz oscillators with a resonance frequency of MHz range.

The bad news is the highest frequency of a commercially available QTF is lower than 500 kHz. The reason is a QTF works at the flexure mode (bending or bowing) of a quartz

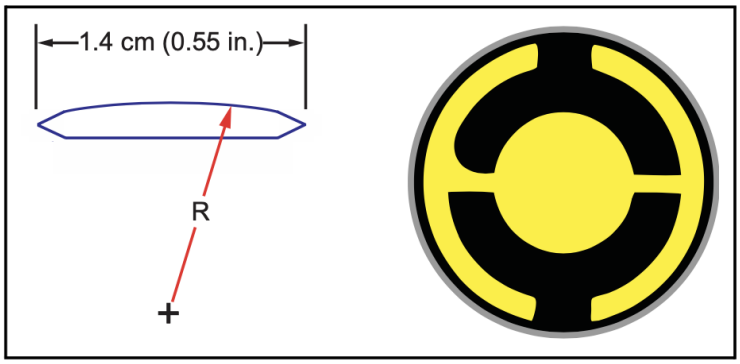

Figure 6.2: The design of the quartz crystal in a deposition monitor [313].

crystal, which has a frequency range of $\sim$ 100 kHz and much lower compared to the thickness shear mode of the quartz crystals ($\sim$ 1 to 150 MHz), as shown in Figure 6.1. To achieve a resonance frequency of about MHz range, we need to use the shear mode of the quartz crystals. The resonant frequency of a mechanical oscillator depends on its size, shape, elasticity, and the speed of sound in the material. Depending on the shape and orientation of the crystal blank, many different modes of vibration can be used and it is possible to control the frequency-temperature characteristics of the quartz resonator to within close limits by an appropriate choice. The most commonly used type of resonator is the AT-cut, where the quartz blank is in the form of a thin plate cut as an angle of about 35°15' to the optic axis of the crystal. The AT-cut quartz crystal works on the thickness shear mode on resonance. For industrial applications, high-frequency quartz crystals are typically cut in the shape of a simple rectangle or circular disk while low-frequency crystals, such as those used in digital watches, are typically cut in the shape of a tuning fork.

We are working on the quartz plates with a resonance frequency of several MHz. One big challenge is to figure out the mounting place of the sample on the quartz plate. The commercially available quartz plates at several MHz range are either rectangular shape or round shape (as shown in Figure 6.3). For the rectangular shaped quartz plate, we have a hard time figuring out where to mount the sample without damping the resonance too much. The round shape quartz might bring more hope since it has been widely used as the essential device for the deposition monitor, which measures the rate and thickness in a thin film deposition process. Figure 6.2 depicts the design of the quartz crystal in a deposition monitor. A circular-shaped crystal increases the symmetry and reduces the number of allowed vibrational modes. With a special design of the deposited electrodes, it can better trap the acoustic energy and limits the excitation to the central area. Energy is not reflected back to the center when it reaches the edge, which decreases the interference with newly launched waves. With the crystal vibration restricted to the plate center, the plate can be

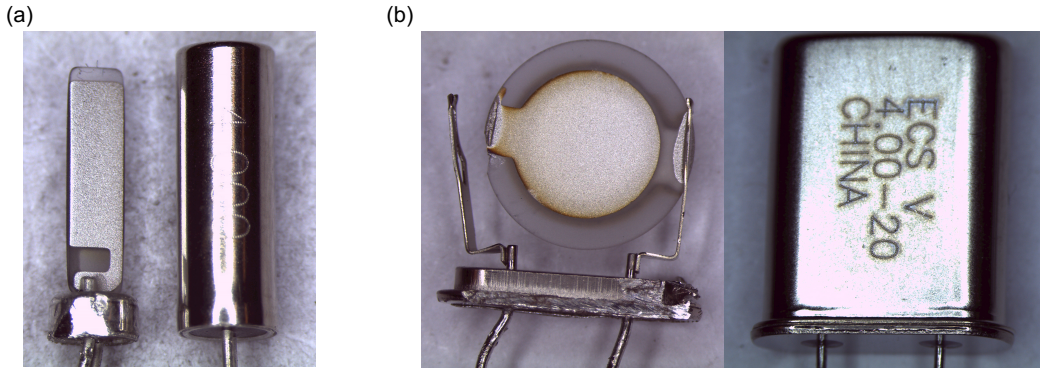

Figure 6.3: 4 MHz (a) rectangular-shaped and (b) round-shaped quartz oscillators.

clamped at the outer edge without introducing any undesirable effects. The mechanism of the crystal used for monitoring the deposition thickness is quite simple. For a bare quartz plate, it has a resonance period of T_q and a mass of M_q. After a small mass M_f is deposited on the center of the quartz plate, the resonance period changes to T_c. It was recognized by Behrndt [314] in 1971 that

$$\frac{M_f}{M_q} = \frac{(T_c - T_q)}{T_q} = \frac{\Delta F}{F_c}, \tag{6.2}$$

where $F_c = \frac{1}{T_c}$, $F_q = \frac{1}{T_q}$, and $\Delta F = F_q - F_c$ is the change in resonance frequency. So we can tell the newly deposited mass by measuring the change of the resonance frequency.

With all the advantages of the round shape quartz plate, it's hopeful that we can adopt this device and further modify it for our torque magnetometry setup. Although there are still several questions to answer. What could be a reasonable sample mass or sample volume? It could greatly damp the vibration if a huge sample is attached to the center of the quartz plate. How should the resonance frequency change correspond to the magnetization signal coming from the sample? Since the mechanical model of a quartz plate working with the shear mode totally differs from that of a QTF, it is necessary to derive a new mechanical model that links the measurement variable to the physical quantity of the sample.

The other direction of shorting the responding time is decreasing the quality factor of the quartz crystal. The intrinsic Q of a quartz crystal is about 10^7 at 1 MHz, which is even higher than the Q of a QTF. One way to bring down the Q is to increase the sample mass. The other way is to add exchange gas inside the probe or merge the quartz crystal into the liquid to decrease the Q. Our data in Figure 2.9 and Figure 2.10 show that both the exchange gas and the liquid could help to damp the vibration of the QTF.

6.2.2 Thermal Hall Measurement in $Fe_{1+y}Te_{1-x}Se_x$ Single Crystals

The pseudogap phase in high T_c superconductors has been extensively studied since its discovery. Whether the pseudogap phase is a precursor of the superconducting state [315, 316, 317] or they are independent/competitive phases [276, 318, 319, 320] are still controversial. It has been suggested that the pseudogap phase may be a common feature in many unconventional superconductors, such as heavy fermions [321] and topological superconductors [322]. In recent years, there has been a lot of debate about the existence of pseudogap states in the iron-based superconductors. Experimental evidence shows that the pseudogap is present in the iron chalcogenide FeSe [323] and $Fe_{1+y}Te_{1-x}Se_x$ [324, 325], iron pnictides $LaFeAs(O_{1-x}F_x)$ [326, 327] and $SmFeAs(O_{1-x}F_x)$ [328, 329], as well as hole-doped $Ba_{1-x}K_xFe_2As_2$ [330, 331] and electron-doped $Ba(Fe_{1-x}Co_x)_2As_2$ [332, 333, 334]. Although counter-evidence has also been provided by scanning tunneling spectroscopy measurements performed on $Ba(Fe_{1-x}Co_x)_2As_2$ [335] and FeSe[336]. In the family of iron-based superconductors, $Fe_{1+y}Te_{1-x}Se_x$ has attracted more and more attention nowadays due to the fact that it holds a superconducting Dirac surface state and Majorana bound states (MBS) at the vortex cores [134, 135, 136]. Apart from magnetotransport and thermopower measurements [324, 325], it's necessary to look for other experimental evidence to verify the existence of pseudogap phases in $Fe_{1+y}Te_{1-x}Se_x$.

Recently, a giant negative thermal Hall conductivity has been discovered in the pseudogap phase of four different cuprate superconductors [337]. It suggests that the thermal Hall effect measurements could also provide evidence for the formation of the pseudogap phase in iron-based superconductors [334]. We propose to conduct thermal Hall measurements in $Fe_{1+y}Te_{1-x}Se_x$ single crystals with different excess Fe levels. It has been reported that the excess Fe content in $Fe_{1+y}Te_{1-x}Se_x$ samples affects the pseudogap temperature much more strongly than the superconducting transition temperature T_c [324]. So it's highly possible that we would see some correlation between the thermal Hall conductivity and the excess Fe content in $Fe_{1+y}Te_{1-x}Se_x$ single crystals. Although we have performed a quick test on the thermal Hall signal in $Fe_{1+y}Te_{1-x}Se_x$ single crystals, the type-E thermocouples generate quite large noise during the temperature or field sweep which could smear out the very small thermal Hall signal. So in the future experiment, we propose to conduct the thermal Hall measurement with a steady-state method, which means we are going to take data at a fixed temperature and magnetic field. Hopefully, the steady-state method could eliminate the electromotive force generated within the thermocouple loops during a field sweep.

The short-term goal of this research is to search for indications of the pseudogap phase in the iron-based superconductors. The origin of the pseudogap is crucial in understand-

ing the pairing mechanism of the unconventional superconductors, especially the high T_c superconductors.

My Ph.D. thesis focuses on the development of new measurement technologies such as the torque differential magnetometry and the thermal measurement setup compatible with PPMS. The QTF-based magnetometry is a reliable method for conducting torque differential magnetometry measurements at cryogenic temperatures and intense magnetic fields. It also solves multiple problems that have been faced by the traditional cantilever-based magnetometry when being used in a pulsed magnetic field. Due to its high sensitivity, the QTF-based magnetometry becomes a powerful probe to resolve the electronic and magnetic anisotropy of novel solid-state materials and can be used in many different research fields in condensed matter physics. The home-designed TTO puck that's compatible with PPMS makes a great compensation for performing thermal measurements on small samples in PPMS. This setup can potentially be used for conducting thermal measurements for all types of materials.

BIBLIOGRAPHY

[1] Emilia Morosan, Douglas Natelson, Andriy H. Nevidomskyy, Qimiao Si, Adv. Mater. **24**, 4896 (2012).

[2] Elbio Dagotto, Science **309**, 257 (2005).

[3] E. Dagotto and Y. Tokura, MRS Bulletin **33**, 1037 (2008).

[4] Patrick A. Lee, Naoto Nagaosa, and Xiao-Gang Wen, Rev. Mod. Phys. **78**, 17 (2006).

[5] Elbio Dagottoa, Takashi Hottab, Adriana Moreo, Phys. Rep. **344**, 1 (2001).

[6] Y. Tokura, Rep. Prog. Phys. **69** 797 (2006).

[7] J.F. Mitchell, D.N. Argyriou, A. Berger, K.E. Gray, R. Osborn, U. Welp, J. Phys. Chem. B **105**, 10731 (2001).

[8] S. Nakatsuji, Y. Maeno, Phys. Rev. Lett. **84**, 2666 (2000).

[9] S. Nakatsuji, V. Dobrosavljević, D. Tanasković, M. Minakata, H. Fukazawa, and Y. Maeno Phys. Rev. Lett. **93**, 146401 (2004).

[10] Maw Lin Foo, Yayu Wang, Satoshi Watauchi, H. W. Zandbergen, Tao He, R. J. Cava, and N. P. Ong, Phys. Rev. Lett. **92**, 247001 (2004).

[11] P. Limelette, P. Wzietek, S. Florens, A. Georges, T. A. Costi, C. Pasquier, D. Jérome, C. Mézière, and P. Batail Phys. Rev. Lett. **91**, 016401 (2003).

[12] V. Sidorov, M. Nicklas, P. G. Pagliuso, J. L. Sarrao, Y. Bang, A. V. Balatsky, and J. D. Thompson, Phys. Rev. Lett. **89**, 157004 (2002).

[13] E. Engel, R. M. Dreizler, Density functional theory: an advanced course. Springer 2011.

[14] Vladimir I. Anisimov, Jan Zaanen, and Ole K. Andersen, Phys. Rev. B 44, 943 (1991).

[15] Walter Metzner and Dieter Vollhardt, Phys. Rev. Lett. **62**, 324 (1989).

[16] Antoine Georges, Gabriel Kotliar, Werner Krauth, and Marcelo J. Rozenberg, **??**Rev. Mod. Phys. **68**, 13 (1996).

[17] D. Vollhardt, K. Held, G. Keller, R. Bulla, T. Pruschke, I. Nekrasov, V. Anisimov, J. Phys. Soc. Jpn. **74**, 136 (2005).

[18] G.Kotliar, S. Savrasov, K. Haule, V. S. Oudovenko, O. Parcollet, C. A. Marianetti, Rev. Mod. Phys. **78**, 865 (2006).

[19] J.B. Torrance, P. Lacorre, A.I. Nazzal, E.J. Ansaldo, Ch. Niedermayer, Phys. Rev. B **45**, 8209 (1992).

[20] Y. Tokura, H. Takagi and S. Uchida, Nature **337**, 345 (1989).

[21] Andrea Damascelli, Zahid Hussain, and Zhi-Xun Shen, Rev. Mod. Phys. **75**, 473 (2003).

[22] J. Kanamori, J. Phys. Chem. Solids **10**, 87 (1959).

[23] A. Moreira dos Santos, A.K. Cheetham, T. Atou, Y. Shono, Y. Yamaguchi, K. Ohyama, H. Chiba, C.N.R. Rao, Phys. Rev. B **66**, 064425 (2002).

[24] F, Millange, V. Caignaert, B. Domengès and B. Raveau and E. Suard, Chem. Mater. **10**, 1974 (1998).

[25] T. Nakajima, H. Kageyama and Y. Ueda, J. Phys. Chem. **63**, 913 (2002).

[26] D. Akahoshi, M. Uchida, Y. Tomioka, T. Arima, Y. Matsui, and Y. Tokura, Phys. Rev. Lett. **90**, 177203 (2003).

[27] E. Dagotto, T. Hotta, A. Moreo, Phys. Rep. **344**, 1 (2001).

[28] J. Burgy, M. Mayr, V. Martin-Mayor, A. Moreo, and E. Dagotto, Phys. Rev. Lett. **87**, 277202 (2001).

[29] J. Burgy, A. Moreo, E. Dagotto, Phys. Rev. Lett. **92**, 097202 (2004).

[30] S. Yunoki, J. Hu, A. L. Malvezzi, A. Moreo, N. Furukawa, and E. Dagotto, Phys. Rev. Lett. **80**, 845 (1998).

[31] A. Moreo, S. Yunoki, E. Dagotto, Science **283**, 2034 (1999).

[32] M. Uehara, S. Mori, C. H. Chen and S.-W. Cheong, Nature **399**, 560(1999).

[33] Despina Louca, T. Egami, E. L. Brosha, H. Röder, and A. R. Bishop, Phys. Rev. B **56**, R8475(R) (1997).

[34] C. N. Berglund and H. J. Guggenheim, Phys. Rev. **185**, 1022 (1969).

[35] John B. Goodenough, J. Solid State Chem. **3**, 490 (1971).

[36] A. Zylbersztejn and N. F. Mott, Phys. Rev. B **11**, 4383 (1975).

[37] A. S. Belozerov, M. A. Korotin, V. I. Anisimov, and A. I. Poteryaev, Phys. Rev. B **85**, 045109 (2012).

[38] V. Eyert, Ann. Phys. (Berlin) **11**, 650 (2002).

[39] V. Eyert, Phys. Rev. Lett. **107**, 016401 (2011).

[40] M. E. Williams, W. H. Butler, C. K. Mewes, H. Sims, M. Chshiev, and S.K. Sarker, J. Appl. Phys. **105**, 07E510 (2009).

[41] R. Grau-Crespo, H. Wang, and U. Schwingenschlogl, Phys. Rev. B **86**, 081101 (2012).

[42] Huihuo Zheng and Lucas K. Wagner, Phys. Rev. Lett. **114**, 176401 (2015).

[43] M. M. Qazilbash, K. S. Burch, D. Whisler, D. Shrekenhamer, B. G. Chae, H. T. Kim, and D. N. Basov, Phys. Rev. B **74**, 205118 (2006).

[44] M. M. Qazilbash, A. A. Schafgans, K. S. Burch, S. J. Yun, B. G. Chae, B. J. Kim, H. T. Kim, and D. N. Basov, Phys. Rev. B **77**, 115121 (2008).

[45] M. M. Qazilbash, M. Brehm, Byung-Gyu Chae, P.-C. Ho, G. O. Andreev, Bong-Jun Kim, Sun Jin Yun, A. V. Balatsky, M. B. Maple, F. Keilmann, Hyun-Tak Kim, and D. N. Basov, Science **318**, 1750 (2007).

[46] M. Z. Hasan and C. L. Kane, Rev. Mod. Phys. **82**, 3045 (2010).

[47] Yoichi Ando, J. Phys. Soc. Jpn. **82**, 102001 (2013).

[48] J. E. Moore, Nature **464**, 194 (2010).

[49] A. Schynder, S. Ryu, A. Furusaki, and A. Ludwig, Phys. Rev. B **78**, 195125 (2008).

[50] X. L. Qi, T. Hughes, S. Raghu, and S. C. Zhang, Phys. Rev. Lett. **102**, 187001 (2009).

[51] Alexei Kitaev, AIP Conf. Proc. **1134**, 22 (2009).

[52] N. Read and Dmitry Green, Phys. Rev. B **61**, 10267(2000).

[53] A .Y. Kitaev, Phys.—Usp. **44**, 131 (2001).

[54] M. Sato, Phys. Lett. B **575**, 126 (2003).

[55] D. J. Thouless, M. Kohmoto, M. P. Nightingale, and M. den Nijs, Phys. Rev. Lett. **49**, 405 (1982).

[56] Mahito Kohmoto, Ann. Phys. **160**, 343 (1985).

[57] C. L. Kane and E. J. Mele, Phys. Rev. Lett. **95**, 226801 (2005).

[58] C. L. Kane and E. J. Mele, Phys. Rev. Lett. **95**, 146802 (2005).

[59] B. A. Bernevig, T. L. Hughes, and S.-C. Zhang, Science, **314**, 1757 (2006).

[60] M. König, S. Wiedmann, C. Brüne, A. Roth, H. Buhmann, L. W. Molenkamp, X.-L. Qi, and S.-C. Zhang, Science, 318, 766 (2007).

[61] J. E. Moore and L. Balents, Phys. Rev. B, **75**, 121306 (2007).

[62] Liang Fu and C. L. Kane, Phys. Rev. B **76**, 045302 (2007).

[63] D. Hsieh, D. Qian, L. Wray, Y. Xia, Y. S. Hor, R. J. Cava, and M. Z. Hasan, Nature **452**, 970 (2008).

[64] A. A. Taskin and Y. Ando, Phys. Rev. B **80**, 085303 (2009).

[65] Pedram Roushan, Jungpil Seo, Colin V. Parker, Y. S. Hor, D. Hsieh, Dong Qian, Anthony Richardella, M. Z. Hasan, R. J. Cava and Ali Yazdani, Nature **460**, 1106 (2009).

[66] A. Nishide, A. A. Taskin, Y. Takeichi, T. Okuda, A. Kakizaki, T. Hirahara, K. Nakatsuji, F. Komori, Y. Ando, and I. Matsuda, Phys. Rev. B **81**, 041309(R) (2010).

[67] D Hsieh, L Wray, D Qian, Y Xia, J H Dil, F Meier, L Patthey, J Osterwalder, G Bihlmayer, Y S Hor, R J Cava and M Z Hasan, New J. Phys. **12**, 125001 (2010).

[68] Y. Xia, D. Qian, D. Hsieh, L. Wray, A. Pal, H. Lin, A. Bansil, D. Grauer, Y. S. Hor, R. J. Cava and M. Z. Hasan, Nat. Phys. **5**, 398 (2009).

[69] D. Hsieh, Y. Xia, D. Qian, L. Wray, J. H. Dil, F. Meier, J. Osterwalder, L. Patthey, J. G. Checkelsky, N. P. Ong, A. V. Fedorov, H. Lin, A. Bansil, D. Grauer, Y. S. Hor, R. J. Cava and M. Z. Hasan, Nature **460**, 1101–1105 (2009).

[70] Yoichi Ando, J. Phys. Soc. Jpn. **82**, 102001 (2013).

[71] Masatoshi Sato and Yoichi Ando, Rep. Prog. Phys. **80**, 076501 (2017).

[72] Xiao-Liang Qi, Taylor L. Hughes, and Shou-Cheng Zhang, Phys. Rev. B **78**, 195424 (2008).

[73] Andreas P. Schnyder, Shinsei Ryu, Akira Furusaki, and Andreas W. W. Ludwig, Phys. Rev. B **78**, 195125 (2008).

[74] Yukio Tanaka, Masatoshi Sato, and Naoto Nagaosa, J. Phys. Soc. Jpn. **81**, 011013 (2012).

[75] Jeffrey C. Y. Teo and C. L. Kane, Phys. Rev. B **82**, 115120 (2010).

[76] Yasumasa Tsutsumi, Masaki Ishikawa, Takuto Kawakami, Takeshi Mizushima, Masatoshi Sato, Masanori Ichioka, and Kazushige Machida, J. Phys. Soc. Jpn. **82**, 113707 (2013).

[77] Po-Yao Chang, Shunji Matsuura, Andreas P. Schnyder, and Shinsei Ryu, Phys. Rev. B **90**, 174504 (2014).

[78] Yasumasa Tsutsumi, Takuto Kawakami, Ken Shiozaki, Masatoshi Sato, and Kazushige Machida, Phys. Rev. B **91**, 144504 (2015).

[79] Darrick Lee and Andreas P. Schnyder, **??**Phys. Rev. B **93**, 064522 (2016).

[80] A. Y. Kitaev, Phys.—Usp. **44**, 131 (2001).

[81] G. E. Volovik, The Universe in a Helium Droplet (Oxford: Oxford University Press), 2003.

[82] Takeshi Mizushima, Yasumasa Tsutsumi, Masatoshi Sato and Kazushige Machida, J. Phys.: Condens. Matter. **27**, 113203 (2015).

[83] Masatoshi Sato, Phys. Rev. B **79**, 214526 (2009).

[84] M. Sato, Phys. Rev. B **81**, 220504(R) (2010).

[85] L. Fu and E. Berg, Phys. Rev. Lett. **105**, 097001 (2010).

[86] P. M. R. Brydon, S. Das Sarma, Hoi-Yin Hui, and Jay D. Sau, Phys. Rev. B **90**, 184512 (2014).

[87] Liang Fu, Phys. Rev. B **90**, 100509(R) (2014).

[88] K. Matano, M. Kriener, K. Segawa, Y. Ando and Guo-qing Zheng, Nature Physics **12**, 852 (2016).

[89] Shingo Yonezawa, Kengo Tajiri, Suguru Nakata, Yuki Nagai, Zhiwei Wang, Kouji Segawa, Yoichi Ando and Yoshiteru Maeno, Nat. Phys. **13**, 123 (2017).

[90] Y. Pan, A. M. Nikitin, G. K. Araizi, Y. K. Huang, Y. Matsushita, T. Naka and A. de Visser, Sci. Rep. **6**, 28632 (2016).

[91] A. M. Nikitin, Y. Pan, Y. K. Huang, T. Naka, and A. de Visser, 94, 144516 (2016).

[92] Guan Du, YuFeng Li, J. Schneeloch, R. D. Zhong, GenDa Gu, Huan Yang, Hai Lin and Hai-Hu Wen, Sci. China—Phys. Mech. Astron. **60**, 037411 (2017).

[93] Tomoya Asaba, B. J. Lawson, Colin Tinsman, Lu Chen, Paul Corbae, Gang Li, Y. Qiu, Y. S. Hor, Liang Fu and Lu Li, Phys. Rev. X **7**, 011009 (2017).

[94] Gil Young Cho, Jens H. Bardarson, Yuan-Ming Lu, and Joel E. Moore, Phys. Rev. B **86**, 214514 (2012).

[95] G. Bednik, A. A. Zyuzin, and A. A. Burkov, Phys. Rev. B **92**, 035153 (2015).

[96] Tao Zhou, Yi Gao, and Z. D. Wang, Phys. Rev. B **93**, 094517 (2016).

[97] Shingo Kobayashi and Masatoshi Sato, Phys. Rev. Lett. **115**, 187001 (2015).

[98] Tatsuki Hashimoto, Shingo Kobayashi, Yukio Tanaka, and Masatoshi Sato, Phys. Rev. B **94**, 014510 (2016).

[99] Lanpo He, Yating Jia, Sijia Zhang, Xiaochen Hong, Changqing Jin and Shiyan Li, NPJ Quantum Mater. **1**, 16014 (2016).

[100] Leena Aggarwal, Abhishek Gaurav, Gohil S. Thakur, Zeba Haque, Ashok K. Ganguli and Goutam Sheet, Nat. Mater. **15**, 32 (2016).

[101] He Wang, Huichao Wang, Haiwen Liu, Hong Lu, Wuhao Yang, Shuang Jia, Xiong-Jun Liu, X. C. Xie, Jian Wei and Jian Wang, Nat. Mater. **15**, 38 (2016).

[102] Liang Fu and C. L. Kane, Phys. Rev. Lett. **100**, 096407 (2008).

[103] Masatoshi Sato, Yoshiro Takahashi, and Satoshi Fujimoto, Phys. Rev. Lett. **103**, 020401 (2009).

[104] Jacob Linder, Yukio Tanaka, Takehito Yokoyama, Asle Sudbø, and Naoto Nagaosa, Phys. Rev. Lett. **104**, 067001 (2010).

[105] Masatoshi Sato and Satoshi Fujimoto, Phys. Rev. Lett. **105**, 217001 (2010).

[106] Akito Daido and Youichi Yanase, Phys. Rev. B **94**, 054519 (2016).

[107] Y. Maeno, H. Hashimoto, K. Yoshida, S. Nishizaki, T. Fujita, J. G. Bednorz and F. Lichtenberg, Nature **372**, 532 (1994).

[108] T. M. Rice and M. Sigrist, J. Phys.: Condens. Matter. **7**, L643 (1995).

[109] Catherine Kallin and John Berlinsky, Rep. Prog. Phys. **79**, 054502 (2016).

[110] K. Ishida, H. Mukuda, Y. Kitaoka, K. Asayama, Z. Q. Mao, Y. Mori and Y. Maeno, Nature **396**, 658 (1998).

[111] G. M. Luke, Y. Fudamoto, K. M. Kojima, M. I. Larkin, J. Merrin, B. Nachumi, Y. J. Uemura, Y. Maeno, Z. Q. Mao, Y. Mori, H. Nakamura and M. Sigrist, Nature **394**, 558 (1998).

[112] Masashi Yamashiro, Yukio Tanaka, and Satoshi Kashiwaya, Phys. Rev. B **56**, 7847 (1997).

[113] Akira Furusaki, Masashige Matsumoto, and Manfred Sigrist, Phys. Rev. B **64**, 054514 (2001).

[114] Michael Stone and Rahul Roy, Phys. Rev. B **69**, 184511 (2004).

[115] Satoshi Kashiwaya, Hiromi Kashiwaya, Hiroshi Kambara, Tsuyoshi Furuta, Hiroshi Yaguchi, Yukio Tanaka, and Yoshiteru Maeno, Phys. Rev. Lett. **107**, 077003 (2011).

[116] Yuji Ueno, Ai Yamakage, Yukio Tanaka, and Masatoshi Sato, Phys. Rev. Lett. **111**, 087002 (2013).

[117] J. Jang, D. G. Ferguson, V. Vakaryuk, R. Budakian, S. B. Chung, P. M. Goldbart, Y. Maeno, Science **331**, 186 (2011).

[118] A. Pustogow, Yongkang Luo, A. Chronister, Y.-S. Su, D. Sokolov, F. Jerzembeck, A. P. Mackenzie, C. W. Hicks, N. Kikugawa, S. Raghu, E. D. Bauer and S. E. Brown, Nature **574**, 72 (2019).

[119] Shunichiro Kittaka, Shota Nakamura, Toshiro Sakakibara, Naoki Kikugawa, Taichi Terashima, Shinya Uji, Dmitry A. Sokolov, Andrew P. Mackenzie, Koki Irie, Yasumasa Tsutsumi, Katsuhiro Suzuki, and Kazushige Machida, J. Phys. Soc. Jpn. **87**, 093703 (2018).

[120] E. Hassinger, P. Bourgeois-Hope, H. Taniguchi, S. René de Cotret, G. Grissonnanche, M. S. Anwar, Y. Maeno, N. Doiron-Leyraud, and Louis Taillefer, Phys. Rev. X **7**, 011032 (2017)

[121] Per G. Björnsson, Yoshiteru Maeno, Martin E. Huber, and Kathryn A. Moler, Phys. Rev. B **72**, 012504 (2005).

[122] Clifford W. Hicks, John R. Kirtley, Thomas M. Lippman, Nicholas C. Koshnick, Martin E. Huber, Yoshiteru Maeno, William M. Yuhasz, M. Brian Maple, and Kathryn A. Moler, Phys. Rev. B **81**, 214501 (2010).

[123] Christopher A. Watson, Alexandra S. Gibbs, Andrew P. Mackenzie, Clifford W. Hicks, and Kathryn A. Moler, Phys. Rev. B **98**, 094521 (2018).

[124] Masatoshi Sato and Satoshi Fujimoto, Phys. Rev. B **79**, 094504 (2009).

[125] Yukio Tanaka, Takehito Yokoyama, Alexander V. Balatsky, and Naoto Nagaosa, Phys. Rev. B **79**, 060505(R) (2009).

[126] E. Bauer, G. Hilscher, H. Michor, Ch. Paul, E. W. Scheidt, A. Gribanov, Yu. Seropegin, H. Noël, M. Sigrist, and P. Rogl, Phys. Rev. Lett. **92**, 027003 (2004).

[127] Tatsuki Hashimoto, Keiji Yada, Ai Yamakage, Masatoshi Sato and Yukio Tanaka, Supercond. Sci. Technol. **27**, 104002 (2014).

[128] Yasuyuki Nakajima, Rongwei Hu, Kevin Kirshenbaum, Alex Hughes, Paul Syers, Xiangfeng Wang, Kefeng Wang, Renxiong Wang, Shanta R. Saha, Daniel Pratt, Jeffrey W. Lynn and Johnpierre Paglione, Science Advances **1**, e1500242 (2015).

[129] Markus Meinert, Phys. Rev. Lett. **116**, 137001 (2016).

[130] Sheng Ran, Chris Eckberg, Qing-Ping Ding, Yuji Furukawa, Tristin Metz, Shanta R. Saha, I-Lin Liu, Mark Zic, Hyunsoo Kim, Johnpierre Paglione, Nicholas P. Butch, Science **365**, 684 (2019).

[131] Z. Wang, P. Zhang, G. Xu, L. K. Zeng, H. Miao, X. Xu, T. Qian, H. Weng, P. Richard, A. V. Fedorov, H. Ding, X. Dai, Z. Fang, Phys. Rev. B **92**, 115119 (2015).

[132] X. Wu, S. Qin, Y. Liang, H. Fan, J. Hu, Phys. Rev. B **93**, 115129 (2016).

[133] G. Xu, B. Lian, P. Tang, X.-L. Qi, S.-C. Zhang, Phys. Rev. Lett. **117**, 047001 (2016).

[134] Peng Zhang, Koichiro Yaji, Takahiro Hashimoto, Yuichi Ota, Takeshi Kondo, Kozo Okazaki, Zhijun Wang, Jinsheng Wen, G. D. Gu, Hong Ding, Shik Shin, Science **360**, 182–186 (2018).

[135] Dongfei Wang, Lingyuan Kong, Peng Fan, Hui Chen, Shiyu Zhu, Wenyao Liu, Lu Cao, Yujie Sun, Shixuan Du, John Schneeloch, Ruidan Zhong, Genda Gu, Liang Fu, Hong Ding, Hong-Jun Gao, Science **362**, 333 (2018).

[136] Lingyuan Kong, Shiyu Zhu, Michał Papaj, Hui Chen, Lu Cao, Hiroki Isobe, Yuqing Xing, Wenyao Liu, Dongfei Wang, Peng Fan, Yujie Sun, Shixuan Du, John Schneeloch, Ruidan Zhong, Genda Gu, Liang Fu, Hong-Jun Gao and Hong Ding, Nat. Phys., DOI: 10.1038/s41567-019-0630-5 (2019).

[137] Xiaoyu Chen, Mingyang Chen, Wen Duan, Xiyu Zhu, Huan Yang and Hai-Hu Wen, arXiv: 1909.01686.

[138] J-X. Yin, Zheng Wu, J-H. Wang, Z-Y. Ye, Jing Gong, X-Y. Hou, Lei Shan, Ang Li, X-J. Liang, X-X. Wu, Jian Li, C-S. Ting, Z-Q. Wang, J-P. Hu, P-H. Hor, H. Ding and S. H. Pan, Nat. Phys. **11**, 543 (2015).

[139] Kun Jiang, Xi Dai, and Ziqiang Wang, Phys. Rev. X **9**, 011033 (2019).

[140] Lu Chen, Fan Yu, Ziji Xiang, Tomoya Asaba, Colin Tinsman, Benjamin Lawson, Paul M. Sass, Weida Wu, B. L. Kang, Xianhui Chen, and Lu Li, Phys. Rev. Applied **9**, 024005 (2018).

[141] Piezoelectric Quartz Tuning Forks for Scanning Probe Microscopy, 2005, Nanonis GmbH, Switzerland.

[142] F.J. Giessibl, S. Hembacher, M. Herz, C. Schiller, J. Mannhart, Stability considerations and implementation of cantilevers allowing dynamic force microscopy with optimal resolution: the qPlus sensor, Nanotechnology **15**, S79 (2004).

[143] A. Kamra, M. Schreier, H. Huebl, and S. T. B. Goennenwein, Theoretical model for torque differential magnetometry of single-domain magnets, Phys. Rev. B **89**, 184406 (2014).

[144] P. Günther, U. Ch. Fischer, and K. Dransfeld, Scanning near-field acoustic microscopy, Appl. Phys. B **48**, 89 (1989).

[145] K. Karrai and Robert Grober, Piezoelectric tip-sample distance control for near field optical microscopes, Appl. Phys. Lett. **66**, 1842 (1995).

[146] K. Karrai and I. Tiemann, Interfacial shear force microscopy, Phys. Rev. B **62**, 13174 (2000).

[147] H. Edwards, L. Taylor, W. Duncan, and A. J. Melmed, Fast, high-resolution atomic force microscopy using a quartz tuning fork as actuator and sensor, J. Appl. Phys. **82**, 980 (1997).

[148] Y. Martin and H.K. Wickramasinghe, Magnetic imaging by force microscopy with 1000 $\mathring{A}$ resolution, Appl. Phys. Lett. **50**, 1455 (1987).

[149] M. R. Koblischka, U. Hartmann, and T. Sulzbach, Resolving magnetic nanostructures in the 10-nm range using MFM at ambient conditions, Mater. Sci. Eng : C **23**, 747 (2003).

[150] F. J. Giessibl, High-speed force sensor for force microscopy and profilometry utilizing a quartz tuning fork, Appl. Phys. Lett. **73**, 3956 (1998).

[151] A. Kamra, S.V. Hoesslin, N. Roschewsky, J. Lotze, M. Schreier, R. Gross, S. T. B. Goennenwein, and H. Huebl, An all-electrical torque differential magnetometer operating under ambient conditions, Eur. Phys. J. B **88**, 224 (2015).

[152] B.C. Stipe, H.J. Mamin, T.D. Stowe, T.W. Kenny, D. Rugar, Magnetic Dissipation and Fluctuations in Individual Nanomagnets Measured by Ultrasensitive Cantilever Magnetometry, Phys. Rev. Lett. **86**, 2874 (2001).

[153] D. P. Weber, D. Rüffer, A. Buchter, F. Xue, E. Russo-Averchi, R. Huber, P. Berberich, J. Arbiol, A. Fontcuberta i Morral, D. Grundler, and M. Poggio, Cantilever Magnetometry of Individual Ni Nanotubes, Nano Lett. **12**, 6139 (2012).

[154] Franz J. Giessibl, Florian Pielmeier, Toyoaki Eguchi, Toshu An, Yukio Hasegawa, Comparison of force sensors for atomic force microscopy based on quartz tuning forks and length-extensional resonators, Phys. Rev. B **84**, 125409 (2011).

[155] Angelo Peronio and Franz J. Giessibl, Attempts to test an alternative electrodynamic theory of superconductors by low-temperature scanning tunneling and atomic force microscopy, Phys. Rev. B **94**, 094503 (2016).

[156] R. N. Bhargava, de Haas-van Alphen and Galvanomagnetic Effect in Bi and Bi-Pb Alloys, Phys. Rev. **156**, 785 (1967).

[157] Boris J. Albers, Marcus Liebmann, Todd C. Schwendemann, Mehmet Z. Baykara, Markus Heyde, Miquel Salmeron, Eric I. Altman, and Udo D. Schwarz, Combined low-temperature scanning tunneling/atomic force microscope for atomic resolution imaging and site-specific force spectroscopy, Rev. Sci. Instr. **79**, 033704 (2008).

[158] Jens Falter, Marvin Stiefermann, Gernot Langewisch, Philipp Schurig, Hendrik Hölscher, Harald Fuchs, and André Schirmeisen, Calibration of quartz tuning fork spring constants for non-contact atomic force microscopy: direct mechanical measurements and simulations, Beilstein J. Nanotechnol. 2014, **5**, 507–516.

[159] Omur E. Dagdeviren and Udo D. Schwarz, Optimizing qPlus sensor assemblies for simultaneous scanning tunneling and noncontact atomic force microscopy operation based on finite element method analysis, Beilstein J. Nanotechnol. 2017, **8**, 657–666.

[160] Franz J. Giessibl, Noncontact Atomic Force Microscopy, (Spinger, 2009, chapter 6).

[161] Joonho Jang, Investigation of half-quantized fluxoid states in Sr_2RuO_4 mesoscopic superconducting rings, University of Illinois at Urbana-Champaign, 2012.

[162] G. Li, Z. Xiang, F. Yu,T. Asaba,B. Lawson, P. Cai, C. Tinsman, A. Berkley, S. Wolgast, Y. S. Eo, Dae-Jeong Kim, C. Kurdak, J. W. Allen, K. Sun, X. H. Chen, Y. Y. Wang, Z. Fisk, Lu Li, Two-dimensional Fermi surfaces in Kondo insulator SmB_6, Science **346**,1208 (2014).

[163] E. Morosan, H. W. Zandbergen, Lu Li, Minhyea Lee, J. G. Checkelsky, M. Heinrich, T. Siegrist, N. P. Ong, and R. J. Cava, Sharp switching of the magnetization in $Fe_{\frac{1}{4}}TaS_2$, Phys. Rev. B **75**, 104401 (2007).

[164] G. Wu, B. L. Kang, Y. L. Li, T. Wu, N. Z. Wang, X. G. Luo, Z. Sun, L. J. Zou, X. H. Chen, Large magnetic anisotropy in FexTaS2 single crystals, arXiv:1705.03139.

[165] J. G. Checkelsky, Minhyea Lee, E. Morosan, R. J. Cava, and N. P. Ong, Anomalous Hall effect and magnetoresistance in the layered ferromagnet $Fe_{\frac{1}{4}}TaS_2$: The inelastic regime, Phys, Rev. B **77**, 014433 (2008).

[166] Lu Li, Torque Magnetometry in Unconventional Superconductors, Princeton University, 2008.

[167] M. Lee, J. Jahng, K. Kim and W. Jhe, Quantitative atomic force measurement with a quartz tuning fork, Appl. Phys. Lett. **91**, 023117 (2007).

[168] Franz J. Giessibl, Atomic resolution on Si(111)-(7×7) by noncontact atomic force microscopy with a force sensor based on a quartz tuning fork, Appl. Phys. Lett. **76**, 1470 (2000).

[169] D. Shoenberg, Magnetic oscillations in metals. (Cambridge University Press, Cambridge, 1984).

[170] Lu Li, J. G. Checkelsky, Y. S. Hor, C. Uher, A. F. Hebard, R. J. Cava, N. P. Ong, Phase Transitions of Dirac Electrons in Bismuth, Science **321**, 547 (2008).

[171] Yi-han Kao, Cyclotron Resonance Studies of the Fermi Surfaces in Bismuth, Phys. Rev. **129**, 1122 (1963).

[172] Kamran Behnia, Luis Balicas, Yakov Kopelevich, Science **317**, 1729 (2007).

[173] Zhu, Z. et al. Emptying Dirac valleys in bismuth using high magnetic fields. Nat. Commun. **8**, 15297 (2017).

[174] Zengwei Zhu, Benoît Fauqué, Yuki Fuseya, and Kamran Behnia, Angle-resolved Landau spectrum of electrons and holes in bismuth, Phys. Rev. **B** 84, 115137 (2011).

[175] F. Y. Yang, Kai Liu, Kimin Hong, D. H. Reich, P. C. Searson, C. L. Chien, Y. Leprince-Wang, Kui Yu-Zhang, and Ke Han, Phys. Rev. B **61**, 6631 (2000).

[176] Zengwei Zhu, Benoît Fauqué, Liam Malone, Arlei Borba Antunes, Yuki Fuseya, and Kamran Behnia, Landau spectrum and twin boundaries of bismuth in the extreme quantum limit, PNAS **109**, 14813-14818 (2012).

[177] K. A. Modic, Ross D. McDonald, J. P. C. Ruff, Maja D. Bachmann, You Lai, Johanna C. Palmstrom, David Graf, Mun Chan, F. F. Balakirev, J. B. Betts, G. S. Boebinger, Marcus Schmidt, D. A. Sokolov, Philip J. W. Moll, B. J. Ramshaw, and Arkady Shekhter, Scale-invariance of a Spin Liquid in High Magnetic Fields, arXiv:1901.09245.

[178] G. Grissonnanche, O. Cyr-Choinière, F. Laliberté, S. Renéde Cotret, A. Juneau-Fecteau, S. Dufour-Beauséjour, M.-È. Delage, D. LeBoeuf, J. Chang, B.J. Ramshaw, D.A. Bonn, W.N. Hardy, R. Liang, S. Adachi, E. Hussey, B. Vignolle, C. Proust, M.

Sutherland, S. Krämer, J.-H. Park, D. Graf, N. Doiron-Leyraud and Louis Taillefer, Direct measurement of the upper critical field in cuprate superconductors, Nat Commun **5**, 3280 (2014).

[179] Physical Property Measurement System Heat Capacity Option User's Manual, Page 1-2, Quantum Design, 25th edition, 2014.

[180] R. Bachmann, F. J. DiSalvo Jr., T. H. Geballe, R. L. Greene, R. E. Howard, C. N. King, H. C. Kirsch, K. N. Lee, R. E. Schwall, H.-U. Thomas, and R. B. Zubeck, Rev. Sci. Instrum. **43**, 205 (1972).

[181] Hai Jun Cho, Gowoon Kim, Takaki Onozato, Hyoungjeen Jeen, Hiromichi Ohta, Int. J. Heat Mass Transf. **137**, 263 (2019).

[182] Yayu Wang, Lu Li, and N. P. Ong, Phys. Rev. B **73**, 024510 (2006).

[183] Kamran Behnia and Hervé Aubin, Rep. Prog. Phys. **69**, 046502 (2016).

[184] E. H. Sondheimer, P. Roy. Soc. Lond A Mat **193**, 484 (1948).

[185] Z. A. Xu, N. P. Ong, Y. Wang, T. Kakeshita and S. Uchida, Nature **406**, 486 (2000).

[186] Kamran Behnia, J. Phys. Condens. Matter **21**, 113101 (2009).

[187] A. Pourret, P. Spathis, H. Aubin and K. Behnia, New J. Phys. **11** 055071 (2009).

[188] Yayu Wang, "Nernst Effect in High Temperature Superconductos", thesis, Princeton University (2004).

[189] Lu Chen, Ziji Xiang, Colin Tinsman, Tomoya Asaba, Qing Huang, Haidong Zhou, and Lu Li, Appl. Phys. Lett. **113**, 061902 (2018).

[190] Lu Chen, Ziji Xiang, Colin Tinsman, Qing Huang, K. G. Reynolds, Haidong Zhou, and Lu Li, Appl. Phys. Lett. **114**, 251904 (2019).

[191] Sangwook Lee, Kedar Hippalgaonkar, Fan Yang, Jiawang Hong, Changhyun Ko, Joonki Suh, Kai Liu, Kevin Wang, Jeffrey J. Urban, Xiang Zhang, Chris Dames, Sean A. Hartnoll, Olivier Delaire, Junqiao Wu, Science **355**, 371–374 (2017).

[192] Keisuke Shibuya, Masashi Kawasaki, and Yoshinori Tokura, Appl. Phys. Lett. **96**, 022102 (2010).

[193] Y. Muraoka and Z. Hiroi, Appl. Phys. Lett. **80**, 583 (2002).

[194] M. Nakano, K. Shibuya, D. Okuyama, T. Hatano, S. Ono, M. Kawasaki, Y. Iwasa and Y. Tokura, Nature **487**, 459–462 (2012).

[195] M. Nakano, K. Shibuya, N. Ogawa, T. Hatano, M. Kawasaki, Y. Iwasa, and Y. Tokura, Appl. Phys. Lett. **103**, 153503 (2013).

[196] Tianxiang Nan, Ming Liu, Wei Ren, Zuo-Guang Ye and Nian X. Sun, Scientific Reports **4**, 5931 (2014).

[197] Kenichi Kawatani, Teruo Kanki, and Hidekazu Tanaka, Phys. Rev. B **90**, 054203 (2014).

[198] Vance R. Morrison, Robert. P. Chatelain, Kunal L. Tiwari, Ali Hendaoui, Andrew Bruhács, Mohamed Chaker, Bradley J. Siwick, Science **346**, 445 (2014).

[199] C. J. Hearn, J. Phys. C: Solid State Phys. **5**, 1317 (1972).

[200] John D. Budai, Jiawang Hong, Michael E. Manley, Eliot D. Specht, Chen W. Li, Jonathan Z. Tischler, Douglas L. Abernathy, Ayman H. Said, Bogdan M. Leu, Lynn A. Boatner, Robert J. McQueeney and Olivier Delaire, Nature **515**, 535 (2014).

[201] Yoshichika Bando, Koichi Nagasawa, Yasutoshi Kato and Toshio Takada, Japan. J. Appl. Phys. **8**, 633 (1969).

[202] Koichi Nagasawa, Mat. Res. Bull. **6**, 853 (1971).

[203] Dongliang Zhao, Xin Qian, Xiaokun Gu, Saad Ayub Jajja and Ronggui Yang, J. Electron. Packag **138(4)**, 040802 (2016).

[204] Y. Muraoka and Z. Hiroi, Appl. Phys. Lett **80**, 583 (2002).

[205] Chongyang Yin, Run Zhang, Guoyu Qian, Qingshan Fu, Canglong Li, Mingchao Wang, Changming Zhu, Liguang Wang, Songliu Yuan, Xiujian Zhao and Haizheng Tao, Appl. Phys. Lett **110**, 172404 (2017).

[206] J. Cao, W. Fan, H. Zheng, and J. Wu, Nano Lett. **9**, 4001 (2009).

[207] Deyi Fu, Kai Liu, Tao Tao, Kelvin Lo, Chun Cheng, Bin Liu, Rong Zhang, Hans A. Bechtel, and Junqiao Wu, J. Appl. Phys. **113**, 043707 (2013).

[208] Takayoshi Katase, Kenji Endo, and Hiromichi Ohta, Phys. Rev. B **92**, 035302 (2015).

[209] V. N. Andreev, A. V. Chudnovskii, A. V. Petrov, E. I. Terukov, Phys. Status Solidi, A Appl. Res. **48**, K153–K156 (1978).

[210] Hyungyu Jin, Oscar D. Restrepo, Nikolas Antolin, Stephen R. Boona, Wolfgang Windl, Roberto C. Myers, and Joseph P. Heremans, Nature Materials **14**, 601–606 (2015).

[211] G. V. Chandrashekhar, H. L. C. Barros, and J. M. Honig, Mat. Res. Bull. **8** 369 (1973).

[212] Sedat Ballikaya, Hang Chi, James R. Salvadorc and Ctirad Uher, J. Mater. Chem. A **1**, 12478(2013).

[213] R. M. Murphy, E. D. Murray, S. Fahy, and I. Savić, Phys. Rev. B **93**, 104304 (2016).

[214] R. M. Murphy, E. D. Murray, S. Fahy, and I. Savić, Phys. Rev. B **95**, 144302 (2017).

[215] Hugo Aramberri, Riccardo Rurali, and Jorge íñiguez, Phys. Rev. B **96**, 195201(2017).

[216] M. A. Carpenter, R. J. Hemley, and H.-k. Mao, J. Geophys. Res.:Solid Earth **105**, 10807 (2000).

[217] D. Andrault, G. Fiquet, F. Guyot, and M. Hanfland, Science **282**, 720 (1998).

[218] A. Togo, F. Oba, and I. Tanaka, Phys. Rev. B **78**, 134106 (2008).

[219] R. S. Kwok and S. E. Brown, Phys. Rev. Lett. **63**, 895 (1989).

[220] Yunus A. Cengel Dr. and Afshin J. Ghajar, Heat and Mass Transfer: Fundamentals and Applications, McGraw-Hill Education, 5th edition, Chapter 15.

[221] G. Venkataraman, Bull. Mater. Sci. **1**, 129 (1979).

[222] Y. Tokura, and N. Nagaosa, Science **288**, 462 (2000).

[223] Yusuke Tokunaga, Thomas Lottermoser, Yunsang Lee, Reiji Kumai, Masaya Uchida, Takahisa Arima and Yoshinori Tokura, Nat. Mater. **5**, 937 (2006).

[224] H. Sagayama, S. Toyoda, K. Sugimoto, Y. Maeda, S. Yamada, and T. Arima, Phys. Rev. B **90**, 241113(R) (2014).

[225] Masaya Uchida, Daisuke Akahoshi, Reiji Kumai, Yasuhide Tomioka, Taka-hisa Arima, Yoshinori Tokura, and Yoshio Matsui, J. Phys. Soc. Jpn. **71**, 2605 (2002).

[226] D. Morikawa, K. Tsuda, Y. Maeda, S. Yamada, and T. Arima, J. Phys. Soc. Jpn. **81** 093602 (2012).

[227] D. Akahoshi, Y. Okimoto, M. Kubota, R. Kumai, T. Arima, Y. Tomioka, and Y. Tokura, Phys. Rev. B **70**, 064418 (2004).

[228] S. Yamada, Y. Maeda, and T.-h. Arima, J. Phys. Soc. Jpn. **81**, 113711 (2012).

[229] W. Schuddinck, G. Van Tendeloo, C. Martin, M. Hervieu, B. Raveau, J. Alloys Compd. **333**, 13 (2002).

[230] Y. G. Zhao, W. Cai, J. Zhao, X. P. Zhang, B. S. Cao, M. H. Zhu, L. W. Zhang, S. B. Ogale, Tom Wu, T. Venkatesan, Li Lu, T. K. Mandal, and J. Gopalakrishnan, Phys. Rev. B **65**, 144406 (2002).

[231] Tomohiko Nakajima, and Yutaka Ueda, J. Appl. Phys. **98**, 046108 (2005).

[232] Gianluca Giovannetti, Sanjeev Kumar, Carmine Ortix, Massimo Capone, and Jeroen van den Brink, Phys. Rev. Lett. **109**, 107601 (2012).

[233] H. Sakai, J. Fujioka, T. Fukuda, M. S. Bahramy, D. Okuyama, R. Arita, T. Arima, A. Q. R. Baron, Y. Taguchi, and Y. Tokura, Phys. Rev. B **86**, 104407 (2012).

[234] S. Kamba, V. Goian, V. Skoromets, J. Hejtmá nek, V. Bovtun, M. Kempa, F. Borodavka, P. Vaněk, A. A. Belik, J. H. Lee, O. Pacherová, and K. M. Rabe, Phys. Rev. B **89**, 064308 (2014).

[235] T. Katsufuji and H. Takagi, Phys. Rev. B **64**, 054415 (2001).

[236] Jiawang Hong, Alessandro Stroppa, Jorge Íñiguez, Silvia Picozzi, and David Vanderbilt, Phys. Rev. B **85**, 054417 (2012).

[237] F. B. Lewis and N. H. Saunders, J. Phys. C **6**, 2525 (1973).

[238] J. L. Cohn, J. J. Neumeier, C. P. Popoviciu, K. J. McClellan, and Th. Leventouri, Phys. Rev. B **56**, R8495(R) (1997).

[239] D. W. Visser, A. P. Ramirez, and M. A. Subramanian, Phys. Rev. Lett. **78**, 3947 (1997).

[240] K. H. Kim, M. Uehara, C. Hess, P. A. Sharma, and S-W. Cheong, Phys. Rev. Lett. **84**, 2961 (2000).

[241] Makoto Tachibana and Eiji Takayama-Muromachi, Appl. Phys. Lett. **92**, 242507 (2008).

[242] K. Kawasaki, Prog. Theor. Phys. **29**, 801 (1963).

[243] H. Stern, J. Phys. Chem. Solids **26**, 153 (1965).

[244] G. S. Dixon and D. Walton, Phys. Rev. **185**, 735 (1969).

[245] P. A. Sharma, J. S. Ahn, N. Hur, S. Park, S. B. Kim, S. Lee, J.-G. Par, S. Guha, and S.-W. Cheong, Phys. Rev. Lett. **93**, 177202 (2004).

[246] X. L. Qi, T. L. Hughes, and S. C. Zhang, Phys. Rev. B **81**, 134508 (2010).

[247] Y.-Y. Xiang, W.-S. Wang, Q.-H. Wang, and D.-H. Lee, Phys. Rev. B **86**, 024523 (2012).

[248] S. Nakosai, Y. Tanaka, and N. Nagaosa, Phys. Rev. Lett. **108**, 147003 (2012).

[249] M. S. Scheurer and J. Schmalian, Nat. Commun. **6**, 6005 (2015).

[250] J. Wang, Y. Xu, and S.-C. Zhang, Phys. Rev. B **90**, 054503 (2014).

[251] P. Hosur, X. Dai, Z. Fang, and X.-L. Qi, Phys. Rev. B **90**, 045130 (2014).

[252] Y. S. Hor, A. J. Williams, J. G. Checkelsky, P. Roushan, J. Seo, Q. Xu, H. W. Zandbergen, A. Yazdani, N. P. Ong, and R. J. Cava, Phys. Rev. Lett. **104**, 057001 (2010).

[253] T. V. Bay, T. Naka, Y. K. Huang, H. Luigjes, M. S. Golden, and A. de Visser, Phys. Rev. Lett. **108**, 057001 (2012).

[254] S. Sasaki, M. Kriener, K. Segawa, K. Yada, Y. Tanaka, M. Sato, and Y. Ando, Phys. Rev. Lett. **107**, 217001 (2011).

[255] S. K. Yip, Phys. Rev. B **87**, 104505 (2013).

[256] M. Kriener, Kouji Segawa, Zhi Ren, Satoshi Sasaki, and Yoichi Ando, Phys. Rev. Lett. **106**, 127004 (2011).

[257] Niv Levy, Tong Zhang, Jeonghoon Ha, Fred Sharifi, A. Alec Talin, Young Kuk, and Joseph A. Stroscio, Phys. Rev. Lett. **110**, 117001 (2013).

[258] Michael Tinkham, Introduction to Superconductivity, 2nd edition, page 8, 2004.

[259] W. S. Corak, B. B. Goodman, C. B. Satterthwaite, and A. Wexler, Phys. Rev. **96**, 1442 (1954).

[260] W. S. Corak, B. B. Goodman, C. B. Satterthwaite, and A. Wexler, Phys. Rev. **102**, 656 (1956).

[261] Manfred Sigrist and Kazuo Ueda, Rev. Mod. Phys. **63**, 239 (1991).

[262] H. Padamsee, J. E. Neighbor, and C. A. Shiffman, J. Low Temp. Phys. **12**, 387 (1973).

[263] David C Johnston, Supercond. Sci. Technol. **26**, 115011 (2013).

[264] Chetan Nayak, Steven H. Simon, Ady Stern, Michael Freedman, and Sankar Das Sarma, Rev. Mod. Phys. **80**, 1083 (2008).

[265] Xiao-Liang Qi and Shou-Cheng Zhang, Rev. Mod. Phys. **83**, 1057 (2011).

[266] Jinsheng Wen, Guangyong Xu, Genda Gu, J M Tranquada and R J Birgeneau, Rep. Prog. Phys. **74**, 124503 (2011).

[267] Lu Li, Yayu Wang, M. J. Naughton, Seiki Komiya, Shimpei Ono, Yoichi Ando, N. P. Ong, J. Magn. Magn. Mater. **310**, 460 (2007).

[268] Y. Onose, Lu Li, C. Petrovic and N. P. Ong, EPL, **79** 17006 (2007).

[269] J. Chang, R. Daou, Cyril Proust, David LeBoeuf, Nicolas Doiron-Leyraud, Francis Laliberté, B. Pingault, B. J. Ramshaw, Ruixing Liang, D. A. Bonn, W. N. Hardy, H. Takagi, A. B. Antunes, I. Sheikin, K. Behnia, and Louis Taillefer, Phys. Rev. Lett. **104**, 057005 (2010).

[270] Lu Li, N. Alidoust, J. M. Tranquada, G. D. Gu, and N. P. Ong, Phys. Rev. Lett. **107**, 277001 (2011).

[271] Alexandre Pourret, Liam Malone, Arlei B. Antunes, C. S. Yadav, P. L. Paulose, Benoît Fauqué, and Kamran Behnia, Phys. Rev. B **83**, 020504(R) (2011).

[272] H.-C. Ri, R. Gross, F. Gollnik, A. Beck, R. P. Huebener, P. Wagner, and H. Adrian, Phys. Rev. B **50**, 3312 (1994).

[273] Yayu Wang, N. P. Ong, Z. A. Xu, T. Kakeshita, S. Uchida, D. A. Bonn, R. Liang, and W. N. Hardy, Phys. Rev. Lett. **88**, 257003 (2002).

[274] M.-S. Nam, A. Ardavan, S. J. Blundell, and J. A. Schlueter, Nature (London) **449**, 584 (2007).

[275] C. M. Varma, Phys. Rev. B **55**, 14554 (1997).

[276] C. M. Varma, Phys. Rev. Lett. **83**, 3538 (1999).

[277] Wei-Cheng Lee, Shou-Cheng Zhang, and Congjun Wu, Phys. Rev. Lett. **102**, 217002 (2009).

[278] Saurabh Maiti and Andrey V. Chubukov, Phys. Rev. B **87**, 144511 (2013).

[279] M. Marciani, L. Fanfarillo, C. Castellani, and L. Benfatto, Phys. Rev. B **88**, 214508 (2013).

[280] Jian Kang, Andrey V. Chubukov, and Rafael M. Fernandes, Phys. Rev. B **98**, 064508 (2018).

[281] A. Kaminski, S. Rosenkranz, H. M. Fretwell, J. C. Campuzano, Z. Li, H. Raffy, W. G. Cullen, H. You, C. G. Olsonk, C. M. Varma and H. Höchst, Nature (London) **416**, 610 (2002).

[282] B. Fauqué, Y. Sidis, V. Hinkov, S. Pailhes, C. T. Lin, X. Chaud, and P. Bourges, Phys. Rev. Lett. **96**, 197001 (2006).

[283] H. A. Mook, Y. Sidis, B. Fauqué, V. Balédent, and P. Bourges, Phys. Rev. B **78**, 020506 (2008).

[284] Y. Li, V. Balédent, N. Barišić, Y. Cho, B. Fauqué, Y. Sidis, G. Yu, X. Zhao, P. Bourges, and M. Greven, Nature (London) **455**, 372 (2008).

[285] Anjan Soumyanarayanan, X. Y. Tee, T. Ito, T. Ushiyama, Y. Tomioka, and C. Panagopoulos, Phys. Rev. B **93**, 054512 (2016).

[286] Jing Xia, Elizabeth Schemm, G. Deutscher, S. A. Kivelson, D. A. Bonn, W. N. Hardy, R. Liang, W. Siemons, G. Koster, M. M. Fejer, and A. Kapitulnik, Phys. Rev. Lett. **100**, 127002 (2008).

[287] Rui-Hua He, M. Hashimoto, H. Karapetyan, J. D. Koralek, J. P. Hinton, J. P. Testaud, V. Nathan, Y. Yoshida, Hong Yao, K. Tanaka, W. Meevasana, R. G. Moore, D. H. Lu, S.-K. Mo, M. Ishikado, H. Eisaki, Z. Hussain, T. P. Devereaux, S. A. Kivelson, J. Orenstein, A. Kapitulnik, Z.-X. Shen, Science **331**, 1579 (2011).

[288] Hovnatan Karapetyan, M. Hücker, G. D. Gu, J. M. Tranquada, M. M. Fejer, Jing Xia, and A. Kapitulnik, Phys. Rev. Lett. **109**, 147001 (2012).

[289] V. Grinenko, P. Materne, R. Sarkar, H. Luetkens, K. Kihou, C. H. Lee, S. Akhmadaliev, D. V. Efremov, S.-L. Drechsler, and H.-H. Klauss, Phys. Rev. B **95**, 214511 (2017).

[290] Shiliang Li, Clarina de la Cruz, Q. Huang, Y. Chen, J. W. Lynn, Jiangping Hu, Yi-Lin Huang, Fong-Chi Hsu, Kuo-Wei Yeh, Maw-Kuen Wu, and Pengcheng Dai, Phys. Rev. B **79**, 054503 (2009).

[291] Wei Bao, Y. Qiu, Q. Huang, M. A. Green, P. Zajdel, M. R. Fitzsimmons, M. Zhernenkov, S. Chang, Minghu Fang, B. Qian, E. K. Vehstedt, Jinhu Yang, H. M. Pham, L. Spinu, and Z. Q. Mao, Phys. Rev. Lett. **102**, 247001 (2009).

[292] J. D. Rameau, N. Zaki, G. D. Gu, and P. D. Johnson, M. Weinert, Phys. Rev. B **99**, 205117 (2019).

[293] Olivier Cyr-Choinière, R. Daou, Francis Laliberté, David LeBoeuf, Nicolas Doiron-Leyraud, J. Chang, J.-Q. Yan, J.-G. Cheng, J.-S. Zhou, J. B. Goodenough, S. Pyon, T. Takayama, H. Takagi, Y. Tanaka and Louis Taillefer, Nature **458**, 743(2009).

[294] F. F. Tafti, F. Laliberté, M. Dion, J. Gaudet, P. Fournier, and Louis Taillefer, Phys. Rev. B **90**, 024519 (2014).

[295] J. Chang, N. Doiron-Leyraud, O. Cyr-Choinière, G. Grissonnanche, F. Laliberté, E. Hassinger, J-Ph. Reid, R. Daou, S. Pyon, T. Takayama, H. Takagi and Louis Taillefer, Nat. Phys. **8**, 751–756 (2012).

[296] Erez Berg, Eduardo Fradkin, Steven A Kivelson and John M Tranquada, New J. Phys. 11, 115004 (2009).

[297] Q. Li, M. Hücker, G. D. Gu, A. M. Tsvelik, and J. M. Tranquada, Phys. Rev. Lett. **99**, 067001 (2007).

[298] J. M. Tranquada, G. D. Gu, M. Hücker, Q. Jie, H.-J. Kang, R. Klingeler, Q. Li, N. Tristan, J. S. Wen, G. Y. Xu, Z. J. Xu, J. Zhou, and M. v. Zimmermann, Phys. Rev. B **78**, 174529 (2008).

[299] Agnieszka Kondrat, Günter Behr, Bernd Büchner, and Christian Hess, Phys. Rev. B **83**, 092507(2011).

[300] A. A. Kalenyuk, A. Pagliero, E. A. Borodianskyi, S. Aswartham, S. Wurmehl, B. Büchner, D. A. Chareev, A. A. Kordyuk, and V. M. Krasnov, Phys. Rev. B **96**, 134512 (2017).

[301] Daniel S. Fisher, Matthew P. A. Fisher, David A. Huse, Phys. Rev. B **43**, 130 (1991).

[302] L. N. Bulaevskii, M. Ledvij, and V. G. Kogan, Phys. Rev. Lett. **68**, 3773 (1992).

[303] Yue Sun, Yuji Tsuchiya, Toshihiro Taen, Tatsuhiro Yamada, Sunseng Pyon, Akira Sugimoto, Toshikazu Ekino, Zhixiang Shi & Tsuyoshi Tamegai, Sci. Rep. **4**, 4585 (2014).

[304] K. Nakayama, Y. Miyata, G. N. Phan, T. Sato, Y. Tanabe, T. Urata, K. Tanigaki, and T. Takahashi, Phys. Rev. Lett. **113**, 237001 (2014).

[305] Huan Yang, Guanyu Chen, Xiyu Zhu, Jie Xing, and Hai-Hu Wen, Phys. Rev. B **96**, 064501 (2017).

[306] Rongwei Hu, Hechang Lei, Milinda Abeykoon, Emil S. Bozin, Simon J. L. Billinge, J. B. Warren, Theo Siegrist, and C. Petrovic, Phys. Rev. B **83**, 224502 (2011)

[307] K. McElroy, Jinho Lee, J. A. Slezak, D.-H. Lee, H. Eisaki, S. Uchida, J. C. Davis, Science **309**, 1048 (2005)

[308] H. Mashima, N. Fukuo, Y. Matsumoto, G. Kinoda, T. Kondo, H. Ikuta, T. Hitosugi, and T. Hasegawa, Phys. Rev. B **73**, 060502(R) (2006)

[309] Damjan Pelc, Marija Vužković, Mihael S. Grbić, Miroslav Požek, Guichuan Yu, Takao Sasagawa, Martin Greven and Neven Barišić, Nat. Commun. **9**, 4327 (2018)

[310] Ziqiang Wang, Jan R. Engelbrecht, Shancai Wang, Hong Ding, and Shuheng H. Pan, Phys. Rev. B **65**, 064509 (2002)

[311] A. V. Balatsky, I. Vekhter, and Jian-Xin Zhu, Rev. Mod. Phys. **78**, 373 (2006)

[312] Xiaokang Li, Liangcai Xu, Linchao Ding, Jinhua Wang, Mingsong Shen, Xiufang Lu, Zengwei Zhu, and Kamran Behnia, Phys. Rev. Lett. **119**, 056601 (2017)

[313] SQM-160 Multi-Film Rate/Thickness Monitor Operation Manual, INFICON Instruments for Intelligent Control, 2015.

[314] K. H. Behrndt, J. Vac. Sci. Technol. **8**, 622 (1971).

[315] Ch. Renner, B. Revaz, J.-Y. Genoud, K. Kadowaki, and Ø. Fischer, Phys. Rev. Lett. **80**, 149 (1998).

[316] O. Tjernberg, H. Nylén, G. Chiaia, S. Söderholm, U. O. Karlsson, M. Qvarford, I. Lindau, C. Puglia, N. Mårtensson, and L. Leonyuk, Phys. Rev. Lett. **79**, 499 (1997).

[317] H. Ding, T. Yokoya, J. C. Campuzano, T. Takahashi, M. Randeria, M. R. Norman, T. Mochiku, K. Kadowaki and J. Giapintzakis, Nature (London) **382**, 51 (1996).

[318] J. L. Tallon J. W. Loram G. V. M. Williams J. R. Cooper I. R. Fisher J. D. Johnson M. P. Staines C. Bernhard, Phys. Status Solidi B **215**, 531 (1999).

[319] J. L. Tallon and J. W. Loram, Physica C **349**, 53 (2001).

[320] David Sénéchal and A.-M. S. Tremblay, Phys. Rev. Lett. **92**, 126401 (2004).

[321] S. Kawasaki, T. Mito, G.-q. Zheng, C. Thessieu, Y. Kawasaki, K. Ishida, Y. Kitaoka, T. Muramatsu, T. C. Kobayashi, D. Aoki, S. Araki, Y. Haga, R. Settai, and Y. Ōnuki, Phys. Rev. B **65**, 020504(R) (2001).

[322] Satoshi Sasaki, M. Kriener, Kouji Segawa, Keiji Yada, Yukio Tanaka, Masatoshi Sato, and Yoichi Ando, Phys. Rev. Lett. **107**, 217001 (2011).

[323] S. Kasahara, T. Yamashita, A. Shi, R. Kobayashi, Y. Shimoyama, T. Watashige, K. Ishida, T. Terashima, T. Wolf, F. Hardy, C. Meingast, H. v. Löhneysen, A. Levchenko, T. Shibauchi and Y. Matsuda, Nat. Commun. **7**, 12843 (2016).

[324] I. Pallecchi, M. Tropeano, C. Ferdeghini, G. Lamura, A. Martinelli, A. Palenzona and M. Putti, J. Supercond. Nov. Magn. **24**, 1751 (2011).

[325] Takumi Otsuka, Shotaro Hagisawa, Yuta Koshika, Shintaro Adachi, Tomohiro Usui, Nae Sasaki, Seya Sasaki, Shunpei Yamaguchi, Yoshiki Nakanishi, Masahito Yoshizawa, Shojiro Kimura, and Takao Watanabe, Phys. Rev. B **99**, 184505 (2019).

[326] Takafumi Sato, Seigo Souma, Kosuke Nakayama, Kensei Terashima, Katsuaki Sugawara, Takashi Takahashi, Yoichi Kamihara, Masahiro Hirano, and Hideo Hosono, J. Phys. Soc. Jpn. **77**, 063708 (2008).

[327] C. Hess, A. Kondrat, A. Narduzzo, J. E. Hamann-Borrero, R. Klingeler, J. Werner, G. Behr and B. Büchner, Europhys. Lett. **87**, 17005 (2009).

[328] Liu Hai-Yun, Jia Xiao-Wen, Zhang Wen-Tao, Zhao Lin, Meng Jian-Qiao, Liu Guo-Dong, Dong Xiao-Li, Wu Gang, Liu Rong-Hua, Chen Xian-Hui, Ren Zhi-An, Yi Wei, Che Guang-Can, Chen Gen-Fu, Wang Nan-Lin, Wang Gui-Ling, Zhou Yong, Zhu Yong, Wang Xiao-Yang, Zhao Zhong-Xian, Xu Zu-Yan, Chen Chuang-Tian and Zhou Xing-Jiang, Chinese Phys. Lett. **25**, 3761 (2008).

[329] T. Mertelj, V. V. Kabanov, C. Gadermaier, N. D. Zhigadlo, S. Katrych, J. Karpinski, and D. Mihailovic, Phys. Rev. Lett. **102**, 117002 (2009).

[330] Y.-M. Xu, P. Richard, K. Nakayama, T. Kawahara, Y. Sekiba, T. Qian, M. Neupane, S. Souma, T. Sato, T. Takahashi, H.-Q. Luo, H.-H. Wen, G.-F. Chen, N.-L. Wang, Z. Wang, Z. Fang, X. Dai and H. Ding, Nat. Commun. **2**, 392 (2011).

[331] Yong Seung Kwon, Jong Beom Hong, Yu Ran Jang, Hyun Jin Oh, Yun Young Song, Byeong Hun Min, Takeuya Iizuka, Shin-ichi Kimura, A V Balatsky and Yunkyu Bang, New J. Phys. **14**, 063009 (2012).

[332] M. A. Tanatar, N. Ni, A. Thaler, S. L. Bud'ko, P. C. Canfield, and R. Prozorov, Phys. Rev. B **82**, 134528 (2010).

[333] S. J. Moon, A. A. Schafgans, S. Kasahara, T. Shibauchi, T. Terashima, Y. Matsuda, M. A. Tanatar, R. Prozorov, A. Thaler, P. C. Canfield, A. S. Sefat, D. Mandrus, and D. N. Basov, Phys. Rev. Lett. **109**, 027006 (2012).

[334] Marcin Matusiak and Thomas Wolf, Phys. Rev B **92**, 020507(R) (2015).

[335] F. Massee, Y. K. Huang, J. Kaas, E. van Heumen, S. de Jong, R. Huisman, H. Luigjes, J. B. Goedkoop and M. S. Golden, Europhys. Lett. **92**, 57012 (2010).

[336] T. Hanaguri, S. Kasahara, J. Böker, I. Eremin, T. Shibauchi, and Y. Matsuda, Phys. Rev. Lett. **122**, 077001 (2019).

[337] G. Grissonnanche, A. Legros, S. Badoux, E. Lefrançois, V. Zatko, M. Lizaire, F. Laliberté, A. Gourgout, J.-S. Zhou, S. Pyon, T. Takayama, H. Takagi, S. Ono, N. Doiron-Leyraud and L. Taillefer, Nature **571**, 376(2019).